The detection and quantification of wave slamming from full-scale measurements on a polar vessel

by
Jesslyn Cassandra Bossau

Thesis presented in partial fulfilment of the requirements for the degree of Master of Engineering (Mechatronic) in the Faculty of Engineering at Stellenbosch University

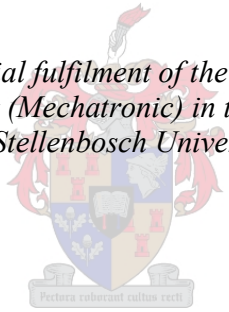

Supervisor: Prof. Anriëtte Bekker

December 2020

Declaration

By submitting this thesis electronically, I declare that the entirety of the work contained therein is my own, original work, that I am the sole author thereof (save to the extent explicitly otherwise stated), that reproduction and publication thereof by Stellenbosch University will not infringe any third party rights and that I have not previously in its entirety or in part submitted it for obtaining any qualification.

Date: December 2020

Abstract

The SA Agulhas II is a polar supply and research vessel. Her extended transom design predisposes her to stern slamming, which may lead to significant high transient whipping responses. Slamming is a concern for the fatigue life of the vessel and may lead to local damage. Slamming and whipping are investigated through full-scale measurements of ship responses, recorded concurrently with the associated vessel operational parameters and environmental conditions encountered during purposely executed open water manoeuvres. A systematic operational study was conducted accordingly, whereby the relative heading and vessel speed were regulated in consistent wave states. Firstly, slamming events need to be accurately detected from signals measured with an accelerometer array in the vessel hull. The MATLAB `findpeaks` function, the continuous Morlet wavelet transform and a spectrogram method were implemented. The continuous Morlet wavelet transform and `findpeaks` method showed the most promising slamming detection capabilities. It was determined that the proposed slamming detection methods require a threshold to identify structurally significant slams and reject slams of smaller magnitude. The peak acceleration amplitude at the time of impact is extracted and the impact site is determined. Typically, more slams are detected at the stern and the peak magnitude of the acceleration measurements is also greatest at the stern. A structural vibration analysis reveals that high velocity levels are potentially a concern for fatigue and may lead to structural damage. Operational modal analysis techniques determined the hull flexure vertical bending response magnitude resulting from wave-induced vibration. The frequency of stern slams is shown to be highest when the vessel is held on station in following and stern-quartering seas and the corresponding acceleration magnitude is largest at the stern under these conditions. It is shown that stern slamming gives rise to higher vibration velocity levels, which indicate that damage is probable for conditions associated with prevalent stern slams of larger magnitude. The frequency and magnitude of slamming incidence detected at the stern can similarly be shown to concur with the associated flexural response, as the first bending mode dominates the response when the ship encounters following and stern-quartering waves during stationary or low-speed operations. The slamming and associated vertical bending mode whipping response is reduced under these conditions as the wave encounter frequency is decreased with increasing vessel speed. Conversely, as the speed increases, more slamming and a greater bending response is observed for head and bow-quartering seas. Consequently, results indicate potential structural damage attributed to stern slamming and whipping, which is exacerbated in following seas when the vessel is stationary. The quantification of wave slamming presented in this thesis therefore warrants a further investigation into the contribution of whipping to fatigue damage in conjunction with a conventional fatigue analysis.

Uittreksel

Die SA Agulhas II is ‘n polêre navorsings- en voorsieningskip. Weens haar verlengede agterdekontwerp is sy geneig tot branderimpakte teen haar agterboeg wat tot beduidende verbygaande transiënte vibrasie lei. Branderimpakte kan lokale skade van die romp veroorsaak, terwyl die daaropvolgende vibrasie gekoppel is aan versnelde vermoeidheid van die struktuur. Branderimpak en die daaropvolgende vibrasie word deur omvattende meting van die dinamiese skeepsrespons ondersoek, saam met die gepaardgaande parameters van *omgewingstoestande* gedurende doelgerigte oop water maneuvers. ‘n Sistematiese bedryfsstudie is gevolglik uitgevoer waarby die relatiewe gang en skip spoed gereguleer is in gereëlde golf toestande. Eerstens, moet branderimpakte akkuraat uit vessnellingseine vasgestel word wat vir die doel in die skip se romp aangebring is. Die MATLAB `findpeaks` funksie, die kontinue Morlet golftransformasie en ‘n spektrogram metode is ondersoek om branderimpakte in lang tydseine te identifiseer. Die kontinue Morlet golftransformasie- en `findpeaks` metodes het die mees belowende identifikasie van branderimpak gelewer waarneming vermoë gewys. Dit is bewerkstellig dat die voorgestelde metode vir die identifikasie van branderimpakte ‘n drumpel benodig om struktureel betekenisvolle branderimpakte te identifiseer en die minder beduidende impakte te ignoreer. Die piek versnellingsamplitude ten tye van die impak is onttrek en die oreenstemende tyd van impak is bepaal. Die tydstip is gebruik om die posisie van die impak op die skeepsromp vas te stel. Tipies word meer branderimpakte teen die agterboeg ondervind en die piekwaarde van versnellingsmetings is ook die grootste by die agterboeg. ‘n Strukturele vibrasieanalise onthul dat hoë vlakke van snelheid potensiëel gekorreleer is met oortollige vermoedheid van die skip en moontlik tot strukturele skade kan lei. Operasionele modale analise is gebruik om die omvang van die romp se buigingsreaksie te bepaal, wat deur golf-geïnduseerde vibrasie veroorsaak is. Die gereëldheid van impakte teen die agterboeg is die hoogste wanneer die skip stasionêr in navolgende brandertoestande bedryf word. Die korresponderende versnellingsomvang is die grootste by die agterboeg onder hierdie toestande. Dit is bewys dat impakte teen die agterboeg meer beduidende vibrasie snelheid veroorsaak, wat aandui dat skade meer waarskynlik is in toestande met oorwegende branderimpakte teen die agterboeg. Die gereëldheid en omvang van branderimpakte teen die agterboeg val saam met die geassosiëerde buigingsreaksie, omdat die eerste buigmode die skiprespons domineer wanneer volgende golwe gedurende stasionêre of lae spoed operasies die boeg impakteer. Die buigingseffekte neem af in grootte en gereëldheid wanneer die relatiewe spoed tussen die romp en golfblootselling afneem. Gevolglik dui die studie op moontlike strukturele skade toegeskryf aan oortollige vibrasie weens branderimpakte op die agterboeg, veral in navolgende golftoestande wanneer die skip nie beweeg nie. Die kwantifisering van golfimpakte aangebied in hierdie verhandeling regverdig dus verdere ondersoek na die bydrae van impakte tot verswakkende skade in samewerking met ‘n gebruiklike vermoeidheidsanalise.

Acknowledgements

Firstly, to my supervisor, Professor Annie Bekker, thank you for your guidance and support over the past three years, which has sometimes extended outside the sphere of academics. I would like to express my sincere gratitude for your encouragement, enthusiasm and for being an exceptional role model. The opportunities which have accompanied this project have surpassed my expectations. I would like to thank the Sound and Vibration Research Group for making the past two years especially enjoyable. Thank you to Nicole Taylor, Armand van Zuydam and Martinique Engelbrecht for your friendship and making the time at sea truly memorable. Thank you to Christof van Zijl for his valuable guidance. Thank you also to our collaborators Tor Aarskog and Andrei Sandru from the Norwegian University of Science and Technology (NTNU) and Aalto University respectively. Without the help of everyone mentioned, the full-scale measurements on the SA Agulhas II (SAA II) would not have been possible. The National Research Foundation (NRF), grant number 110737, and the Department of Science and Technology under the South African National Antarctic Programme are gratefully acknowledged for their support and financial assistance towards this research. Moreover, I would like to thank the South African Department of Environmental Affairs (DEA), African Marine Solutions (AMSOL), Captain Knowledge Bengu and the crewmembers for their collaboration in the measurements on board the SAA II and for allowing us to perform the dedicated vessel manoeuvres. Thank you for your interest in our research goals and making our work on board the SAA II possible. Thank you to the chief scientists for planning and leading the Southern oCean seAsonaL Experiment (SCALE) voyages. It was a privilege to be a part of these voyages, to gain valuable insight and to build relationships with fellow scientists from across the world, who contributed to making it an unforgettable experience. Thank you to my family for their love and support. I appreciate all that you do for me and cherish the memories that we share. Lastly, thank you to God for his grace, his steadfast love and for the lessons learnt throughout this time. Thank you for being part of my journey and that I can rest in you Lord.

Table of contents

List of figures

List of tables

Nomenclature

A	Amplitude correction factor for FFT window
a	Scale parameter
Bft	Beaufort number
b	Morlet wavelet transform time shifting parameter
C	Speed of wave propagation
c	Intrinsic mode function component
D	Vessel depth
$D_x(n,p)$	Discrete wavelet transforming coefficient
d	Damping coefficient
F	Force
F_n	Froude number
$F(\omega)$	Fourier transform
$F(\omega,\tau)$	Short-Time Fourier Transform
f	Frequency
f_e	Encounter frequency
f_s	Sampling frequency
G_{qq}	Power spectral density matrix of the inputs
G_{xx}	Power spectral density matrix of the responses
g	Gravitational acceleration
$H(j\omega)$	Frequency response function matrix
H_s	Significant wave height
h	Empirical mode decomposition sifting component
I	Impulse
i	Data element index
k	Spring constant
L	Vessel length
M	Length of the data frame
M_i	Median of the sum of the difference between each element and the median of the series
M_j	Median of the series
MAC	Modal assurance criterion matrix
MAD	Median absolute deviation
m	Mass
N	Number of FFTs
n	Integer for discrete wavelet transform
p	Integer for discrete wavelet transform
$q(t)$	Operational environmental excitation inputs
R^2	Coefficient of determination
r	Residue
S	Singular value matrix
T_W	Mean wave period
t	Time
U	Singular vector matrix
V	Ship velocity
v	Envelope mean
$W_x(a,b)$	Continuous wavelet transforming coefficient
x_i	Element of the series

x_j	Series of original elements
$x(t)$	Signal
β	Parameter determining the geometric shape
$\delta(t)$	*Dirac delta* function
ε	Time constant
ζ	Relation to Froude number assesses the vessel motion relative to waves
η	MAD constant, which is associated with the normality of the data distribution
θ	The angle of ρ measuredpositive from the x-axis in the clockwise direction
κ	Kaiser window leakage
λ	Wavelength
μ	Encounter angle
ξ	Damping ratio
ρ	Perpendicular distance from the origin to a line
σ	Standard deviation
τ	Spectrogram time shifting parameter
Φ	Mode shape matrix
φ	*Mode shape*
ϕ	Initial phase
$\psi(t)$	Mother wavelet
$\psi_{a,b}(t)$	Daughter wavelet
ω	Modulation parameter
ω_c	Wave circular frequency
ω_d	Damped natural frequency
ω_e	Circular encounter frequency
ω_n	Natural frequency

1. Introduction

1.1. Background

The S.A Agulhas II (SAA II) serves as a Polar Supply and Research Vessel (PSRV) in Antarctica and the Southern Ocean for the South African National Antarctic Program (SANAP) since 2012 (Soal, Bienert & Bekker, 2015). The SAA II is exposed to demanding operational conditions, including navigation through pack ice and rough open water storms with waves reaching 12 metres in height (Nickerson & Bekker, 2017). The waves, ice and wind apply forces on the structure and combined with the excitation from the machinery, engines and propellers on board, these excitation mechanisms may dispose the ship structure to excessive vibration and slamming (Soal et al., 2015). Wave slamming affects the comfort of passengers and the long-term safety of the vessel in the harsh offshore environment. This study is of importance for vessel design, crewmembers, scientific operations, financers, insurers and other stakeholders.

Previous research investigated the stern slamming phenomena experienced by the SAA II in the context of human comfort. The relevant ISO standards were applied for the evaluation of human exposure to whole-body vibrations (Soal & Bekker, 2013). Subsequent research indicated that wave slamming negatively effects the crew and vessel structure (Omer, 2016). Operational Modal Analysis (OMA) was also employed to investigate the vessel's global structural dynamic response characteristics, for example, the natural frequencies and mode shapes (Soal *et al.*, 2015). The SAA II was consequently instrumented to perform full scale acceleration measurements to benefit a diverse set of research objectives.

The present investigation is focused on extracting peak values from long acceleration and velocity measurements, which relate to slamming events, as well as determining the site of a slam impact. Due to the possible detrimental effects of wave slamming it is also desirable to quantify the severity of wave slamming experienced and to evaluate the effect on the structural integrity of the vessel. The detection of wave slamming incidents and evaluating their strength is important for investigating the correlation between slamming occurrences and the induced global response of the vessel (Dessi, 2014). The automated detection of slamming events is required to relate the occurrence of wave slamming with compounding factors such as wave parameters and the vessel speed. Measurable inputs will be investigated to determine the operational modes and environmental conditions, which pre-dispose the SAA II to problematic stern slamming.

This project originated from a proposal by my supervisor Prof A. Bekker. It is conducted in partial fulfilment of the requirements for the degree of Master of Mechatronic Engineering at Stellenbosch University. A previous undergraduate project conducted in 2018 is titled "The use of anomaly detection algorithms to detect wave slamming" (Bossau, 2018).

1.2. Research objectives

The primary research objective is to quantify the incidence and the effect of wave slamming on the SAA II. To achieve this research aim, wave slamming is investigated through systematic vessel operations. A slamming detection algorithm is proposed and the ship responses to wave slamming are investigated using full-scale accelerometer measurements. The supporting objectives are summarised as follows:

- To design focused operational manoeuvres so as to gain insight regarding the occurrence of wave slamming.
- To acquire full-scale measurements of ship responses to wave slamming concurrently with vessel operational parameters and environmental conditions during a voyage on the SAA II.
- To propose an optimal automated slamming detection algorithm that extracts the peak acceleration amplitude at the time of a wave slamming impact from multi-channel full-scale accelerometer measurements with long time histories, in conjunction with the segregation of bow and stern slamming events.
- To determine the operational modes and environmental conditions, which pre-dispose the SAA II to problematic stern slamming, based on specified measurable inputs.
- To investigate slamming measurements alongside existing structural standards and regulations with regard to vessel fatigue life.
- To perform an operational modal analysis with the purpose of relating the global bending response of the vessel structure to wave slamming.

2. Literature review

2.1. Slamming and wave induced vibrations

Wave slamming is described as a sudden, high amplitude acceleration force, due to waves impacting the stern, bow or hull bottom of the vessel structure for a short period of time (Kapsenberg, 2011). It produces an impulsive signal with a large acceleration amplitude at the time of the impact. The vessel structure experiences large, high frequency, cyclic oscillations, which diminish over time, in response to impulsive events. The global transient vibration response of the vessel structure is called whipping (Dessi, 2014; White, Lee & Wang, 2012). Resonant wave-induced vibrations, known as springing, also occur due to waves continuously exciting the vessel structure. Springing may therefore be excited when the wave encounter frequency or the sum of two encounter frequencies coincides with the natural frequencies of the hull girders (DNV GL, 2018).

Slamming is a random, non-stationary and non-linear event. The global response subjects the vessel to large shearing forces and bending moments. The local response of the exterior of the vessel, which is subject to repeated impacts, results in local damage (Constantinescu, Alaoui, Nême & Rigo, 2011). The impact location on the vessel structure is used to classify slamming as bottom slamming, bow-flare slamming, breaking wave impacts or wet-deck slamming (Bertram, 2012). Bottom slamming and stern counter slamming may lead to high whipping responses (White *et al.*, 2012). The SAA II is predisposed to stern slamming (Omer & Bekker, 2016).

Springing and whipping occur frequently and simultaneously and may be difficult to differentiate (DNV GL, 2018). Once springing is initiated the hull girder natural vibrations may continue for a significant time period as there is low damping resistance. Whipping induced vertical bending moment oscillations generally damp out rapidly after several wave periods, therefore the total number of whipping cycles in the operational lifetime of a vessel is considered small. It is noted that springing may significantly influence fatigue life as the number of springing stress cycles is very large. However, whipping results in large stresses, whereas the hull girder stresses due to springing are typically lower in magnitude (White *et al.*, 2012). Mao et al. reported that nonlinear responses, such as whipping, contribute to about 30% of the total fatigue damage (Mao, Ringsberg, Rychlik & Storhaug, 2010). Another study showed that high frequency components of strain measurements increased the total fatigue damage by 23% and that this increased to 43% during the worst half hour that was recorded. Moreover, the fatigue damage incurred during the worst day corresponded to approximately two months of typical fatigue loading (Storhaug & Moe, 2007). Consequently, both springing and whipping can increase the fatigue loading, whereas only whipping is considered to significantly increase the extreme loading (DNV GL, 2015).

Whipping is considered more critical than springing for the fatigue life of the SAA II. As the whipping decay coefficient increases fatigue life also increases (Thomas, Davis, Holloway & Roberts, 2015). Springing is typically a concern for ships with large length to depth ratios or ships with low natural frequencies ($\omega_n < 0.5\ Hz$) and speeds above 20 knots (White *et al.*, 2012). The SAA II can reach a maximum velocity of 16 knots and the first natural frequency is around 2 Hz (Department of Environmental Affairs, 2019; Soal, 2014; Van Zijl, 2020). The whipping and springing of a container vessels with a L/D ratio of 13.8 was investigated by Barhoumi and Storhaug (2014), whereas the ratio for the SAA II is 12.7. Special consideration is required for a rule length, that is the distance along the design waterline, greater than 330 m and a breadth greater than 47 m (DNV GL, 2015). The SAA II does not possess these features.

Fatigue life reduces as the peak slam stress increases, wave height increases or the rate of slams increases (Thomas *et al.*, 2015). Consequently, stern slamming experienced by the SAA II, in combination with whipping induced vertical bending moments influences the fatigue life of the vessel. This is a concern for safety and it also has economic implications as it increases maintenance and repair costs (Henry & Bailey 1970). In practise it is the vibration in addition to the wave frequency loading that significantly contributes to the vibration damage for vessels (DNV GL, 2018).

2.2. Structural failure of vessels

In the 1960s and 1970s large local loads exaggerated the problem of fatigue failures of super-tankers, which resulted in thousands of cracks in numerous vessels after only a few years of service (Fricke, 2017). The early 1990s showed a peak in lives and vessels lost due to bulk carrier vessel accidents. This increased concerns regarding safety standards and fatigue design considerations (Lee, 2008). The knowledge of fatigue and material strength has since advanced, vessel design and assessment methods have also been developed. These methods

evaluate the fatigue strength of structures based on stress cycles and once fatigue cracks or defects are detected methods involving fracture mechanics and crack-driving parameters are employed to determine the fitness for continued service. Associated failures are rare these days, provided that local stresses and structural aspects are predictable (Fricke, 2017). Nevertheless, the effects of springing and whipping vibratory phenomena on fatigue life are of concern for vessels which operate in harsh and unpredictable environmental conditions.

The MSC Napoli was a container ship which experienced structural failure of her hull in 2007. Rough seas, with 9 m waves, caused significant pitching while she transited the English Channel. The engine room flooded and the crew abandoned the vessel. It was concluded that the failure did not result from identifiable construction or material deficiencies. It is believed that slamming induced whipping increased the wave loading, however, classification societies are unable to confidently predict the magnitude of increased loading or the effect on a vessel's structure. Empirical data suggests that whipping can increase wave bending moments between 10% and 50% on container ships. It is also believed that adjustments to the MSC Napoli's speed could have influenced the magnitude and frequency of slamming and whipping experienced, thereby reducing the risk of hull failure. The effect of slamming and whipping needs to be considered for vessel design and structural safety (Marine Accident Investigation Branch, 2008).

Another more recent example of structural failure is the five-year-old MOL COMFORT container ship that split into two halves before sinking while in transit in the Indian Ocean in 2013. The ship experienced hogging and this caused the midship to fracture. The significant wave height was 5.5 m with a Beaufort wind force scale of 7. Subsequent safety inspections revealed that 5 of the 6 sister ships showed buckling deformations up to 20 mm in height amidships (Committee on Large Container Ship Safety, 2013). Therefore, stern slamming in combination with whipping induced vertical bending moments experienced by the SAA II requires attention, when taking into consideration the potential of structural failures resulting in catastrophic events. Structural inspections and monitoring systems are necessary to uncover flaws before they propagate in a brittle manner (Lee, 2008).

Accidents are not the only consequence that warrants research attention on the subject of slamming. Slamming is also the main reason for intentional speed reduction of vessels sailing in head and bow-quartering seas. The captain may also decide to avoid storms. This delays the arrival time, which in turn influences the economy of vessel operation and the fuel required for the voyage (Kapsenberg, 2011). The daily running cost of the SAA II in 2013 was around a quarter of a million rand (Melanie Gosling, 2013).

2.3. Review of ship slamming analysis

Analytical solutions exist to study wave slamming on some simple ship structures and can achieve satisfactory results (Wang & Guedes Soares, 2017). The problem of slamming was first analysed using momentum theory by von Kármán almost a hundred years ago (1929). A well-known initial study on statistical characteristics of wave slamming was published by Ochi (1964). The probability of the vessel fore foot emerging and exceeding a re-entry velocity threshold was used to determine

the likelihood of a slam. This is based on the assumption that the relative vertical velocity and motions between vessel structure and wave surfaces are Gaussian. A weakness is that bottom slamming is approximated by a section of the vessel fully emerging from the water and then impacting a flat horizontal fluid surface, whereas sea states with steep breaking waves incur maximum wave impacts. The method applies to short-term statistics, for slamming events relating to a specific wave energy spectrum as well as a constant vessel speed and relative heading. While the seamanship of the captain, for example reducing speed or changing heading, affects the long-term statistics of slamming loads (Kapsenberg, 2011).

Numerical tools have been developed to better analyse complex structures and incorporate complicated factors, such as compressibility effects. Slamming problems are investigated numerically using Computational Fluid Dynamics (CFD) tools. These are often computationally expensive and it is not simple to achieve accurate results, therefore it is recommended that numerical tools are employed to analyse specific structures after the preliminary design phase (Wang & Guedes Soares, 2017). Experimental techniques and model tests of slamming problems have also been investigated (Kapsenberg, 2011). Wang and Guedes Soares (2017) noted that more research has focused on bow slamming, as it has been proven that there is a high probability of severe bow slamming events for high speed vessels in extreme ocean conditions. They also reported that low speed or stationary vessels with a small draft at the stern may encounter frequent wave impacts, especially in following waves. Scale model tests of a 290 m cruise vessel investigated the whipping response. The tests corroborated full scale observations of stern slamming with severe whipping encountered in following seas for vessel speeds below 6 knots and significant wave heights above 3 m. Whipping induced by bow slamming was reported to increase for head seas with higher vessel speeds and larger wave heights (Dessi, 2006; ISSC Committee II.2, 2009).

Kapsenberg (2011) notes that full-scale measurements are necessary to validate slamming calculations and investigate the details of real-life impact phenomena. Long-term measurements may be used to model the captain's seamanship; by adjusting speed and course to avoid extreme conditions. He recommended accelerometers to measure the whipping response and strain gauges to measure global loads as well as local stresses at the site of impact. The importance of measuring environmental conditions is also highlighted (Kapsenberg, 2011). The location of maximum dynamic stress is not generally known for initial installations of strain gauges, however this is not critical for accelerometers, which are easily installed and reusable (Gaberson, 2007). As mentioned previously, the SAA II was instrumented for full-scale acceleration measurements, which limits the present study accordingly. Slamming is also characterized by impulsive pressure peaks and loads when the ship structure impacts the water surface (Wang & Guedes Soares, 2017). However, methods involving pressure gauges are not practical as holes need to be drilled in the hull structure and numerous gages are necessary to capture the localised high-pressure impact (Kapsenberg, 2011).

With regard to fatigue loading, the whipping and springing are superimposed on the wave frequency loading. The total stress history consists of wave frequency stresses and high frequency stresses. From this the total fatigue damage can be calculated. The wave-induced vibration damage consists of the difference between

the total fatigue damage and the wave damage. Full-scale measurements have shown that the vibration damage and wave damage are of comparable magnitude, however it is dependent on the type of vessel and operating conditions. The rainflow counting method is a recognised method to ascertain the fatigue loading history for broadband frequency spectrums (DNV GL, 2015).

The rainflow counting method determines the number of stress-strain cycles incurred by identifying pairs of local maxima and minima in the strain loading, which form a closed stress/strain hysteresis loop that corresponds to the loading and unloading of the material (Amzallag, Gerey, Robert & Bahuaud, 1994; Rychlik, 1987). It is believed to present the most accurate fatigue life predictions. When stress measurements are available for uniaxial loading conditions, the accumulated fatigue damage over a time period is estimated by determining the rainflow cycle ranges and then using an appropriate S-N curve and the Palmgren-Miner law (Mao *et al.*, 2010). Frequency-domain numerical fatigue analysis, such as the narrow-band approximation, is also often used to estimate the fatigue damage during one sea state and it is applicable when measurements of stresses may not be available (Mao *et al.*, 2010). Therefore, in industry strain gauges are used to measure the stress history and to determine the fatigue life of vessels. Nevertheless, the prediction of fatigue life involves uncertainties due to real-life operational conditions and the current design calculation procedures, which do not directly account for the effects of wave induced vibration (Barhoumi & Storhaug, 2014).

Employing digital twin technology to monitor the result of vessel operating conditions is a principal objective of future research on the SAA II (Bekker, 2018). A digital twin is a dynamic digital model, which employs real-time data recorded by sensors to continually represent a physical entity or process. The historical and current operation and physical state of the object or process are simulated and digitally replicated (Erikstad, 2017; Mussomeli, Meeker, Shepley & Schatsky, 2018). Recording and monitoring the structural loading of an asset allows strategic, tactical and operational decisions to be made. The hindsight gained from analysing historical time series can lead to insight and foresight. For example, the model can be developed to aid route planning by assessing forecasted weather and ocean conditions. Similarly, the model can be developed to advise on the optimal speed and heading for specific conditions that are encountered. It can also influence future vessel design considerations (Erikstad, 2018). Therefore, historical and new voyage data, along with operational conditions, can be consolidated using digital twin technology to aid operational decisions related to wave slamming and fatigue life.

2.4. Impulse response

Impulsive phenomena are defined as large magnitude forces or voltages, for example, which act over a short time interval (Boyce & DiPrim, 2001). Figure 2.1 illustrates the modelling of impulsive forces. The impulse of the force is defined in Equation (1), where the magnitude of the impulse can be determined by computing the time integral of the force $F(t)$. The integral is evaluated by calculating the area under the curve, which is defined to be unity for the unit impulse response function. The parameter ε is a small positive constant and as $\varepsilon \to 0$, the impulse tends to

unity, $I(\varepsilon) = 1$. An idealised unit impulse function, the *Dirac delta* function $\delta(t)$, is defined in Equation (2). The magnitude of the impulse is infinitely large at $t = 0$, and it is zero for all other times, t. The duration of the impulse is infinitely small. A unit impulse at time instance, $t = t_0$ is defined in Equation (3) (Boyce & DiPrim, 2001; Inman, 2014).

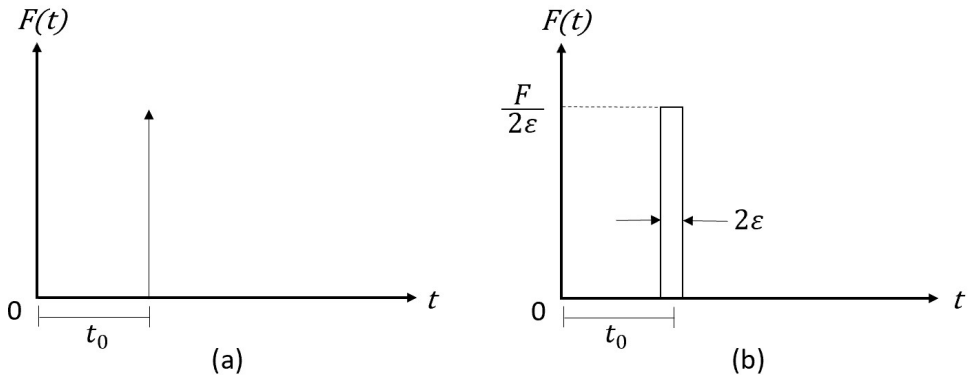

Figure 2.1: Dirac delta function modelling impulsive loading, (a) analytic impulsive force, (b) large magnitude force applied over a short time interval (Inman, 2014)

$$I(\varepsilon) = \int_{t_0-\varepsilon}^{t_0+\varepsilon} F(t)dt = \int_{-\infty}^{\infty} F(t)dt \tag{1}$$

$$\int_{-\infty}^{\infty} \delta(t)dt = 1 \tag{2}$$

$$\int_{-\infty}^{\infty} \delta(t - t_0)dt = 1 \tag{3}$$

The equation of motion for a single degree of freedom (SDOF) system is given in Equation (4), where m is the mass, d is the damping coefficient and k is the spring constant of the system. The response of the system to impulsive excitation is usually expressed in terms of displacement and time, as illustrated in Figure 2.2 for an under-damped system ($\xi < 1$). Figure 2.2 shows the displacement response, but the same impulsive and transient response features can be noted for acceleration. The free impulsive response of such a system is presented in Equation (5), where ϕ is an initial phase value. The signal and those derived from it are analysed for time values that are zero or positive. The natural frequency ω_n and damping ratio ξ are defined from the system parameters as shown in Equation (6) and (7) respectively. For a unit *Dirac delta* impulse excitation, A is given in Equation (8). With the damped natural frequency ω_d given by Equation (9) (Anthony & Simón, 2009).

$$0 = m\ddot{x}(t) + d\dot{x}(t) + kx(t) \tag{4}$$

$$x(t) = Ae^{-\xi\,\omega_n t}\sin(\omega_d t + \phi) \tag{5}$$

$$\omega_n = \sqrt{\frac{k}{m}} \tag{6}$$

$$\xi = \frac{d}{2\sqrt{k\,m}} \tag{7}$$

$$A = \frac{1}{m\,\omega_d} \tag{8}$$

$$\omega_d = \omega_n\sqrt{1-\xi^2} \tag{9}$$

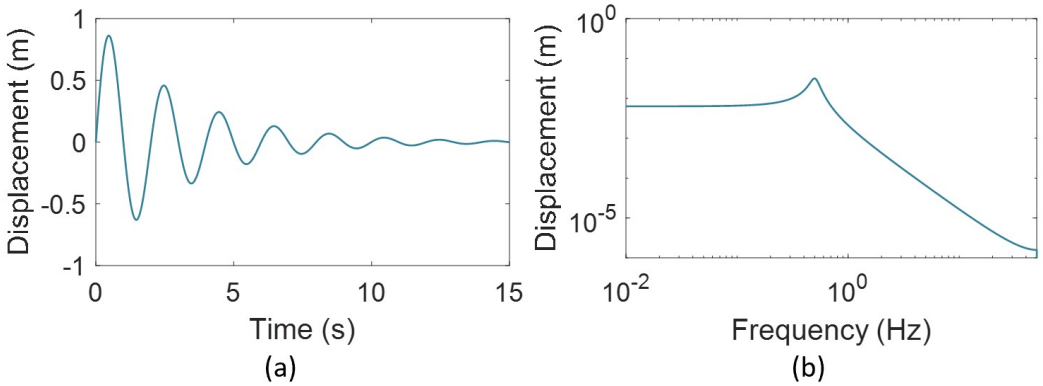

Figure 2.2: (a) Impulse response for an underdamped SDOF system in the time domain, (b) FFT representation of the signal in the frequency domain

As mentioned previously, wave slamming occurs when the vessel structure re-enters the ocean water and the contact area between the surface of the vessel and the fluid expands rapidly, due to a small relative angle between the surface of the vessel and the fluid. The waves impact the vessel structure and impose an impulsive force for a short duration of time (Kapsenberg, 2011). The impulse response due to wave slamming produces large oscillations, which diminish over time, as with an underdamped system. It is experienced throughout the vessel structure and is known as whipping (Dessi, 2014).

2.5. Signal processing techniques in literature

2.5.1. Spectrogram

Wave slamming acceleration signals are non-stationary and present frequency content that varies over time. Spectrograms may be implemented to present the recorded data as a colour plot of the signal, where the magnitude of the signal at each frequency is presented as a function of time using a colour scale (Pijanowski, Villanueva-Rivera, Dumyahn, Farina, Krause, Napoletano, Gage & Pieretti, 2011). The fast Fourier transform (FFT) is a simple approach that transforms data from the time domain into the frequency domain. The Fourier transform is defined in Equation (10).

$$F(\omega) = \int_{-\infty}^{\infty} f(t)e^{-j\omega t}dt \leftrightarrow f(t) = 12\pi\int_{-\infty}^{\infty} F(\omega)e^{j\omega t}d\omega \tag{10}$$

The discrete-time FFT assumes a periodic signal within the time window being analysed. If the signal is not periodic, leakage errors will arise (Öztürk, 1995). If the end of the time record does not smoothly join with the start, as shown in

Figure 2.3 (b), the FFT is computed for a signal with discontinuities. The false jump discontinuities considerably reduce the accuracy of the FFT results (Fan & Liu, 2001). When a signal is truncated in the time domain, the loss of information is characterized as leakage in the frequency domain (Smith, Dahl & Thornhill, 1996). Leakage results in the spread of energy being represented across the surrounding frequencies in the frequency domain, rather than showing each of the signal components as a single line (Brandt, 2011). It is therefore necessary to transform a nonperiodic waveform into a periodic waveform within the window period so that the spectrum magnitude may be calculated more accurately (Öztürk, 1995).

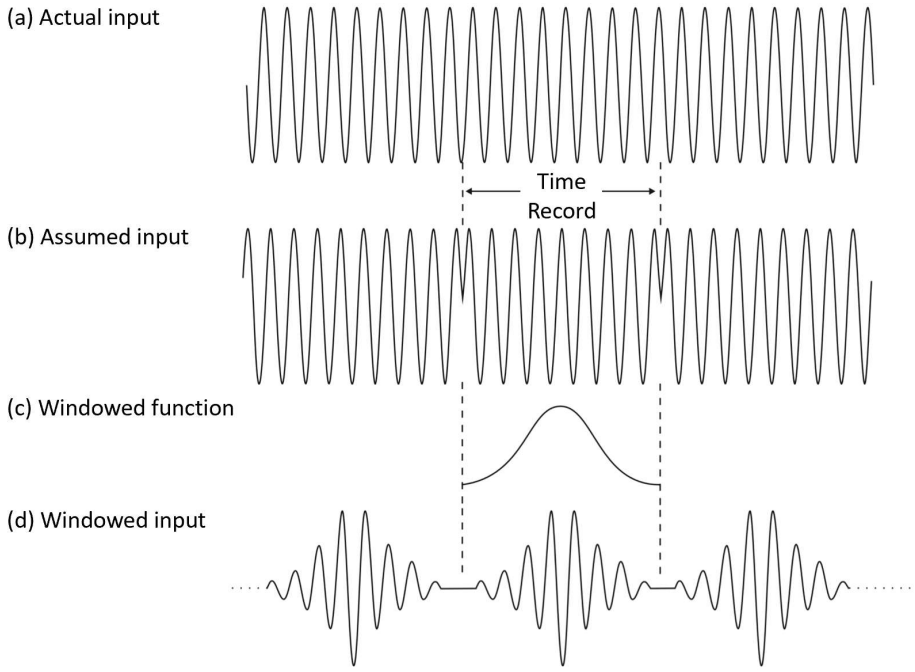

Figure 2.3: Windowing of an input signal which is continuous and not periodic over the time record (Agilent Technologies, 2000)

It is desirable to achieve a high resolution in both the time and frequency domain, however, due to Heisenberg's uncertainty principle, a high resolution cannot exist for both domains concurrently. Therefore, the more precisely one of the values is known, either time or frequency, the less accurately the other value is known (Ghoraani, 2010). To resolve a local temporal signal event, the frequency resolution needs to be sacrificed. This is only true for windowed techniques, such as the spectrogram, where the signal is analysed as subdivided intervals which are assumed to be stationary (Loughlin, Pitton & Atlas, 1992).

$$F(\omega,\tau) = \int_{-\infty}^{\infty} x(t)\psi^*(t-\tau)e^{-j\omega t}dt \qquad (11)$$

The Fourier analysis decomposes a signal into its different frequency components and determines the relative strength of each component. The Short-Time Fourier Transform (STFT) is used to analyse non-stationary signals and is presented in Equation (11). It is used to generate the frequency domain component of the spectrogram. The STFT applies a window function $\psi(t)$ at time τ, and calculates

the Fourier transform of the windowed signal. The window function allows non-stationary signals to be approximated as stationary for Fourier analysis. The statistical characteristics of non-stationary signals change with time (Samundiswary & Subbarao, 2016). The parameters ω and τ control the modulation and translation of the window function respectively. The fixed time window $\psi(t)$ results in a fixed time–frequency resolution (Kıymıka, Güler, Dizibüyük & Akın, 2005). Equation (12) and Equation (13) give the frequency and time resolution respectively and show how both are inversely proportional to one another. The parameter f_s is the sampling frequency and M is the number of the data points being considered (Dressler, 2006).

$$\Delta f = \frac{f_s}{M} \tag{12}$$

$$\Delta t = \frac{M}{f_s} \tag{13}$$

Broadband spectrograms employ a short window duration and can achieve a good time resolution at the expense of frequency resolution. Therefore, broadband spectrograms can localise the temporal occurrence of impulsive events, however, they smear together adjacent component frequencies, known as harmonics. Broadband spectrograms may be used to visualise the natural frequencies and harmonics of the ship and to determine time instances when the vessel experiences wave slamming. Wave slamming results in broadband excitation; therefore, it does not excite the system at a single frequency, instead the impact excites a range of frequencies. Conversely, narrowband spectrograms with a longer window duration, cannot be used to extract slamming incidences. They have good frequency resolution, but the time resolution is not good enough to extract the time at which there is a peak in the acceleration amplitude (Loughlin *et al.*, 1992).

2.5.2. Wavelet transforms

A wavelet is a localized waveform with a rapidly decaying wavelike oscillation of limited duration (Huang & Bai, 2003). Wavelets provide information that relates the time and scale of a signal and are ideal for the analysis of both transient and non-stationary signals. They facilitate the extraction of time varying features and may be more appropriate for data with sharp discontinuities than the sine and cosine functions, which form the basis of Fourier analysis (Graps, 1995). The energy of a signal can be represented in terms of time and frequency as a two-dimensional image. There are two categories of wavelet transforms, specifically the discrete (dwt) and continuous (cwt) wavelet transforms (Khanam, Tandon & Dutt, 2014).

The cwt gathers excessive and often superfluous information as it ascertains numerous coefficients. This results in a high computational cost, which limits its applications (García Plaza & Núñez López, 2018; Kumar & Kumar, 2017). The dwt is significantly less computationally expensive, with significantly less coefficients. A series of low pass and high pass filters decompose the original signal, $x(t)$, into low frequency approximation signals and high frequency detail signals at each level of decomposition, as is illustrated in Figure 2.4. The dwt has been used to analyse impulsive vibration signals in literature, nevertheless, the frequency range

of signal components should be considered for the given application. Impulses generate high frequency components, which emerge in the high frequency range of wavelet decomposition (Khanam *et al.*, 2014). However, the dwt presents limitations for the analysis of high frequency signal components and has a coarser frequency resolution compared to the cwt (García Plaza & Núñez López, 2018).

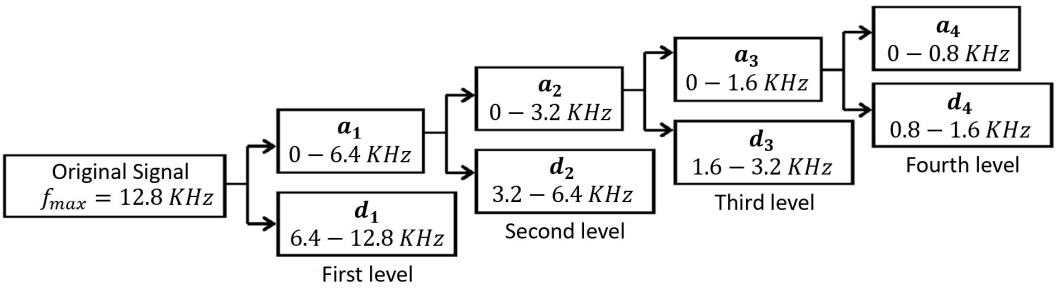

Figure 2.4: Discrete wavelet transform signal decomposition with approximation signals ($\boldsymbol{a_1}$ to $\boldsymbol{a_4}$) and detail signals ($\boldsymbol{d_1}$ to $\boldsymbol{d_4}$) (Khanam *et al.*, 2014)

The continuous wavelet transform of a signal $x(t)$ is defined in Equation (14), where $W_x(a,b)$ characterizes the wavelet transforming coefficient derived from the signal. The scale parameter is defined as a and the time shifting parameter is b. The asterisk, *, denotes a complex conjugate. The mother wavelet is defined as $\psi(t)$. The daughter wavelets, $\psi_{a,b}(t)$, are derived by repeatedly varying both the scale factor and the time shifting parameter. The factor $\frac{1}{\sqrt{a}}$ ensures that energy is preserved as the daughter wavelets are scaled (Yang & Ren, 2004). The discrete wavelet transform is presented in Equtation (15), the terms $2^n\ p$ and 2^n represent the translation and scale parameters respectively and ψ^* is the complex conjugate of the mother wavelet (Khanam *et al.*, 2014).

$$W_x(a,b) = \frac{1}{\sqrt{a}} \int_{-\infty}^{\infty} x(t)\psi^* \left(\frac{t-b}{a}\right) dt \tag{14}$$

$$D_x(n,p) = \frac{1}{\sqrt{2^n}} \int_{-\infty}^{\infty} x(t)\psi^* \left(\frac{t-2^n\ p}{2^n}\right) dt \tag{15}$$

Scaling refers to the process of shrinking and stretching the signal with respect to time. The scale factor is inversely proportional to frequency. A larger scale factor results in a dilated wavelet and lower frequency, as indicated in Figure 2.5 (a). A smaller scale factor results in a compressed wavelet and higher frequency, as shown in Figure 2.5 (c). The scaled wavelet is shifted in time along the length of the signal and is compared with the original signal. Where the scaled wavelet corresponds to original signal, the transform outputs a higher value. This process is repeated for each of the different scales to ascertain coefficients which are a function of the shift parameter and scale factor (Devleker, 2016). Thereby wavelets separate the signal into different frequency components and then measure the similarity between the signal component and the daughter wavelet, with a resolution matched to its scale (Graps, 1995; Yang & Ren, 2004).

A wavelet function is able to precisely extract signal components that have a similar shape (Yang & Ren, 2004). Stretched, low-frequency wavelets act as a large

window and help capture the slowly varying changes in a signal with exceptional frequency resolution. Shrunken, high-frequency wavelets act as a small window and help to capture abrupt and impulsive changes in a signal with a good time resolution (Devleker, 2016; Graps, 1995). This makes high-frequency wavelets with a low scale factor ideal for the detection of impulsive wave slamming signal components, since a good time resolution at high frequencies is necessary to extract the time of impact precisely. The relationship between the time and frequency domain resolution for different scales is illustrated in Figure 2.5 and Figure 2.6. For spectrograms, a single window is used for all frequencies and the resolution is the same across the time-frequency plane (Graps, 1995). However, this time-frequency resolution trade-off is not applicable due to the adaptive time width of the wavelet window function.

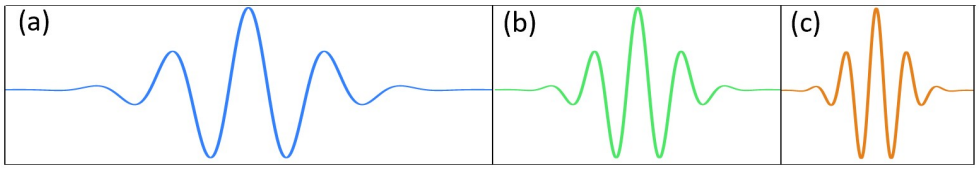

Figure 2.5: Wavelet scaling: (a) large scale factor wavelet, (b) mother wavelet, (c) small scale factor wavelet

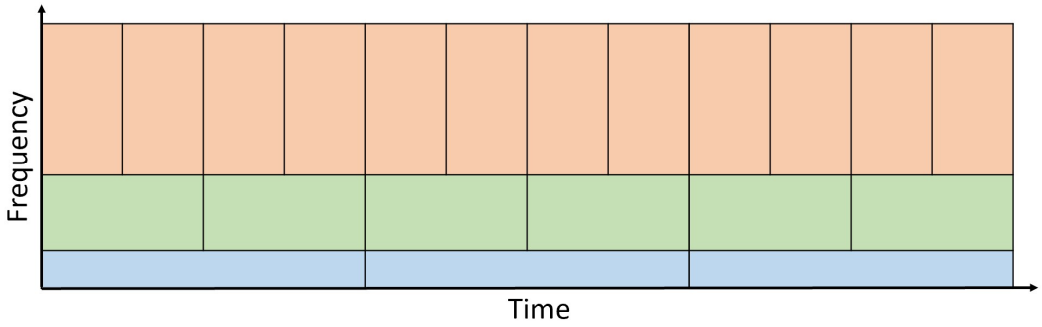

Figure 2.6: Time and frequency resolution at different scales

The complex Morlet wavelet function is given in Equation (16). The β parameter controls the geometric shape of the wavelet. As β approaches zero the function converges to a cosine function with good frequency resolution. This is illustrated in Figure 2.7 (a). As β approaches infinity the function progresses into an impulsive function with good time resolution as demonstrated in Figure 2.7 (c). Therefore, a larger β is advised for the extraction of impulsive events. Furthermore, the wavelet transforms should be performed at a frequency region where the impulse has a significant response, whereas harmonic signals have a limited response (Yang & Ren, 2004). Moreover, the Morlet transform is a type of bandpass filter and the mathematical form of the wavelet is similar to that of an impulse, which was discussed in Section 2.4. Therefore, it can be seen that the impulse response for a SDOF system presented in Figure 2.2 and Equation (5) on page 7 is similar to the Morlet wavelet presented in Figure 2.7 and Equation (16).

$$\psi(t) = \frac{1}{\sqrt{2\pi}} e^{-\left(\frac{t^2}{2}\right)\beta^2} e^{j\omega t} \tag{16}$$

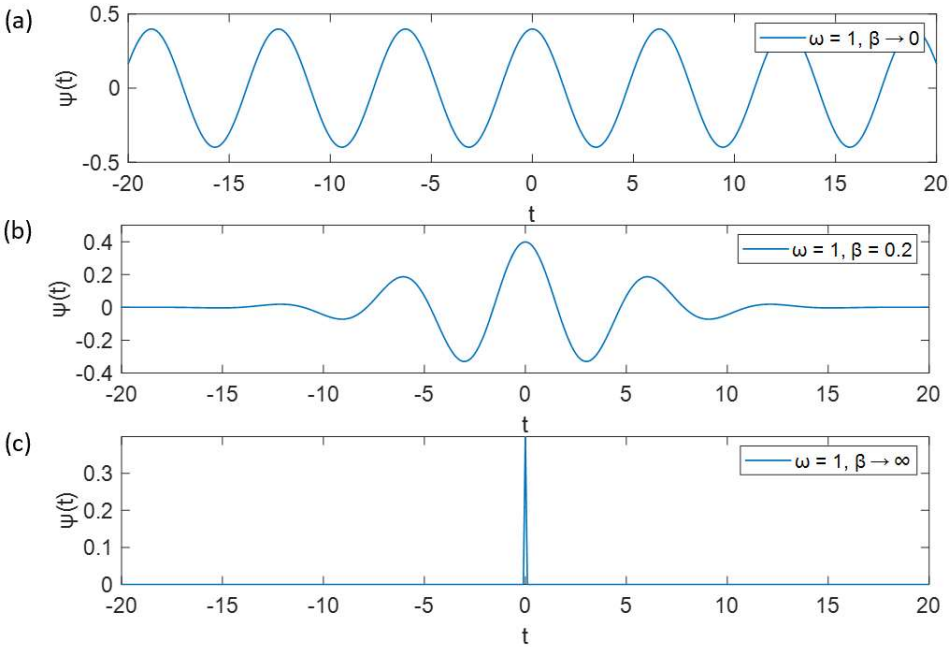

Figure 2.7: Morlet wavelet function for different β values

The Morlet wavelet was used to effectively extract impulsive features in non-stationary vibration signals with good noise suppression (Yang & Ren, 2004). However, Yang et al. (2004) also noted that the wavelet-based envelope analysis required a soft-thresholding method to enhance noise reduction and emphasise significant signal features. Previous research has investigated using the Morlet wavelet to create a scalogram image with striated slamming features (Bekker & Van Zijl, 2019; Bekker, Van Zijl & Saunders, 2018) so that the energy distribution of a vibration signal can be analysed in the time and frequency domain (Sheen, 2009). The resulting scalogram pattern can be used to analyse the characteristic features of the impulsive signal, as illustrated in Figure 2.8 (He & Liu, 2011). More specifically, image processing techniques can be employed to detect line features of the scalogram, which are related to impulsive events in the time signal.

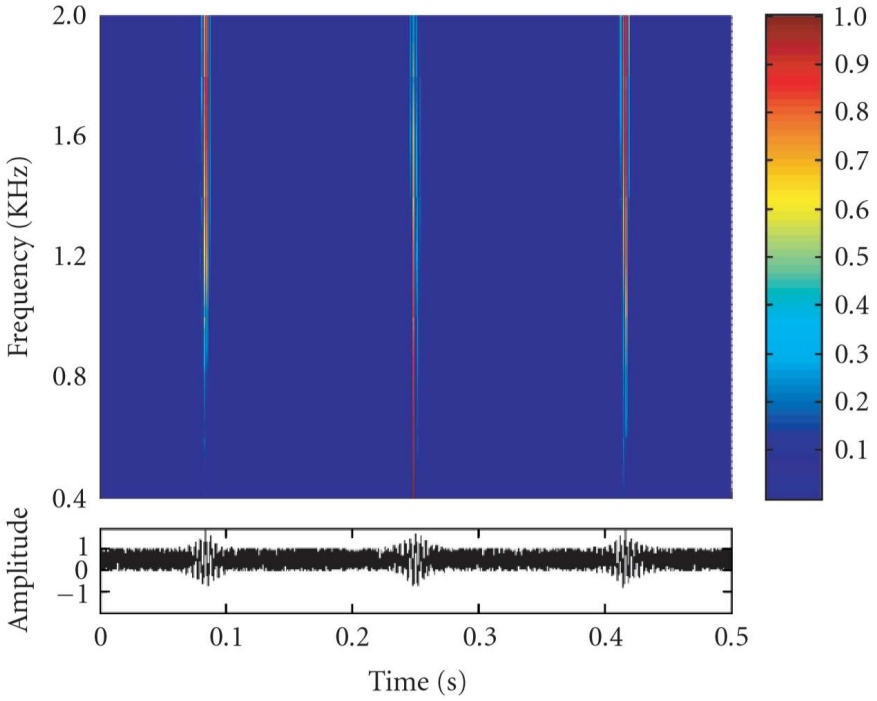

Figure 2.8: Scalogram image of noisy impulse signal (Yang & Ren, 2004)

2.5.3. Empirical mode decomposition

Empirical mode decomposition (EMD) is a data-driven method that presents information on localized amplitudes and frequencies and it is used for time-frequency analysis of non-stationary signals (Rabi, Balusamy & Jawahar, 2019). This method decomposes non-stationary signals into their oscillatory modes, called intrinsic mode functions (IMFs). Every IMF satisfies two conditions. Firstly, the total number of extrema (local minima and maxima) and the total number of zero crossings must be equal or differ by one. Secondly, the mean value of the envelope through the local maxima and the envelope through the local minima is zero (Alickovic, Kevric & Subasi, 2018).

Most of the riding waves of a signal, namely oscillations without a zero crossing between extrema, can be eliminated through a process called sifting (Zeiler, Faltermeier, Keck, Tomé, Puntonet & Lang, 2010). The EMD sifting process components are illustrated in Figure 2.9. The extrema of a signal are identified and the local maxima are connected by a cubic spline to produce the upper envelope, indicated by (a). Another curve is fitted through the local minima for the lower envelope, indicated by (d). The mean of the two envelopes is computed, as illustrated by (c), and the result bisects the data well. Equation (17) demonstrates how the first component h_1 is computed. The mean, v_1, is subtracted from the original signal, $x(t)$, and the result is evaluated to determine if IMF criteria are met. If the component is not an IMF, the process is repeated and h_1 is treated as the input signal. The process is repeated k times, as indicated by Equation (18), until h_{1k} is an IMF. The process is then terminated and the first IMF component of the data is designated as c_1 in Equation (19).

$$h_1 = x(t) - v_1 \tag{17}$$

$$h_{1k} = h_{1(k-1)} - v_{1k} \tag{18}$$

$$c_1 = h_{1k} \tag{19}$$

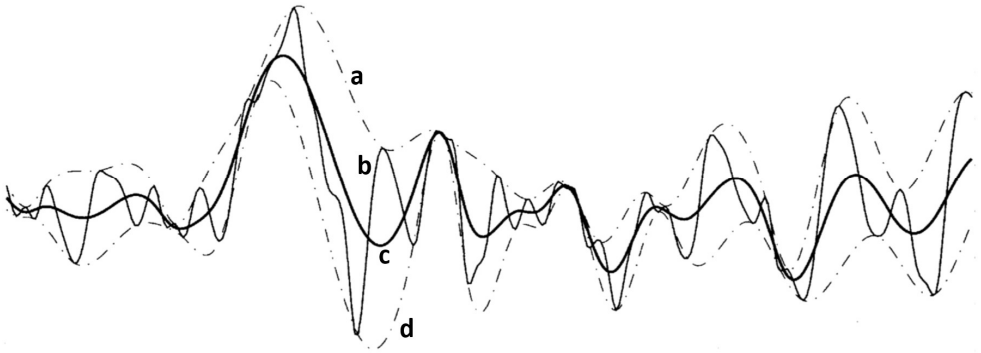

Figure 2.9: EMD sifting process components: (a) upper envelope, (b) original signal, (c) envelope mean, (d) lower envelope (Huang, Zheng & Tung, 1998)

To ensure that the IMF components are physically meaningful in terms of both amplitude and frequency modulations the sifting process is stopped when the standard deviation (σ) of two consecutive sifted signals is smaller than a threshold. The standard deviation computed from the two consecutive sifting results is indicated in Equation (20) (Huang *et al.*, 1998). Additionally, a certain number of sifting iterations may be specified, as over-sifting has a tendency to separate meaningful IMFs into meaningless fragments. Limiting the sifting steps results in more physically significant and realistic IMFs. Oversampling the signal also considerably improves EMD results and prevents over-sifting (Zeiler *et al.*, 2010).

$$\sigma = \sum_{t=0}^{T} \frac{\left|h_{1(k-1)}(t) - h_{1k}(t)\right|^2}{h_{1(k-1)}^2(t)} \tag{20}$$

The first IMF, c_1, is separated from the input signal to produce a residue, r_1, as indicated in Equation (21). Generally, c_1 contains the finest scale or the shortest period, and consequently the highest frequency signal component. The residue contains information of longer period components. The sifting process is then applied to the residue, which is considered the new input signal. This procedure can be repeated to determine all subsequent IMFs and residues. A number of criteria can terminate the sifting process. For example, when the component, c_n, or the residue, r_n, becomes inconsequently small or when the residue becomes a monotonic function and no more IMFs can be removed. The original signal can be reconstructed by adding all of the IMF's and the residue together as shown in Equation (23) (Huang *et al.*, 1998). The IMFs present differences in amplitude and oscillations for different conditions and different applications, these features can be analysed. Each IMF component should contain one unique frequency and one unique mode of vibration (Susanto, Liu, Yamada, Hwang, Tanaka & Sekiya, 2018).

$$r_1 = x(t) - c_1 \tag{21}$$

$$r_n = r_{n-1} - c_n \tag{22}$$

$$x(t) = \sum_{i=1}^{n} c_i + r_n \tag{23}$$

Figure 2.10 illustrates EMD for an acceleration time signal. The first five IMFs obtained from the repeated sifting process is summarised in the figure. Ten IMF components were obtained, which is the default maximum number of IMFs that may be extracted before the decomposition process is terminated (MathWorks, 2018a). It is observed that the first IMF captures the impulsive high frequency signal components well and that subsequent IMFs generally present lower frequency signal components.

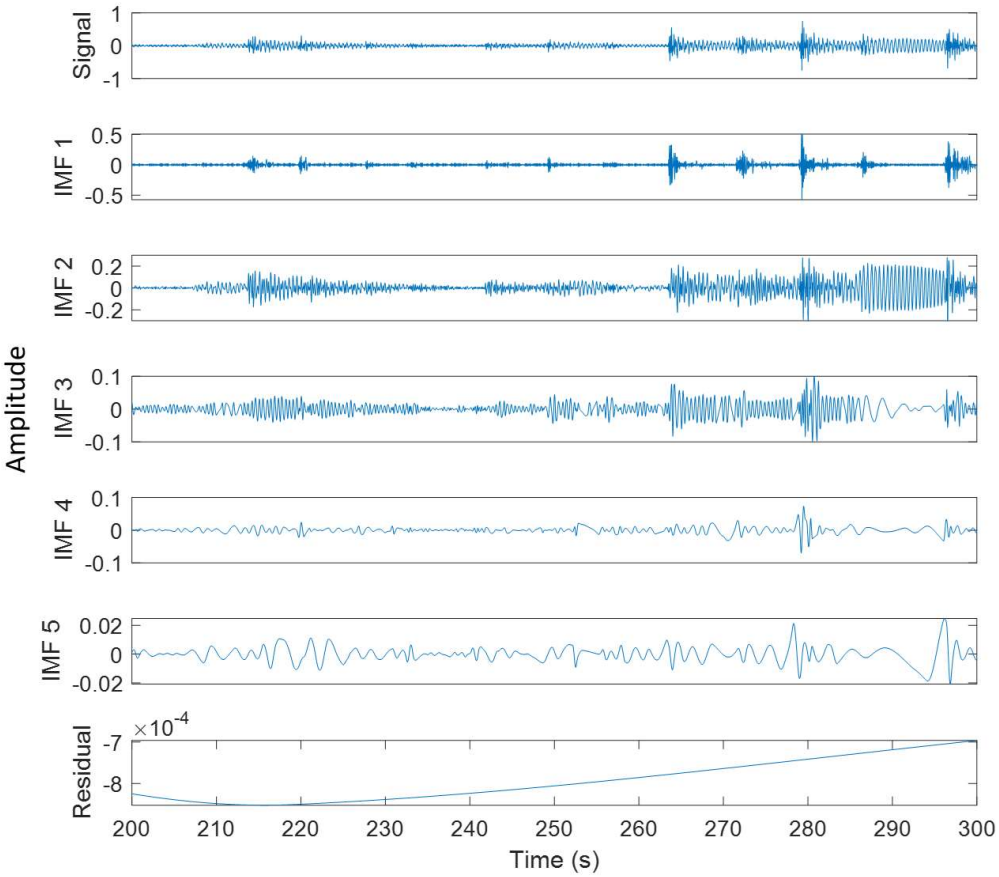

Figure 2.10: Empirical mode decomposition showing the original signal, the IMF components (IMF 1 to IMF 5) and the residual

As previously stated, the dwt may be used to decompose vibration signals, to obtain detailed coefficients and to filter signal noise, resulting in fewer coefficients and a lower computational cost compared to the cwt (García Plaza & Núñez López, 2018; Kumar & Kumar, 2017). Research has shown that EMD is effective for time-frequency analysis and that the IMFs may be used similar to the detailing coefficients obtained from the dwt as it also identifies various scales in the data. The de-noising capability of EMD is found to be equally effective to that of the dwt (Rabi *et al.*, 2019). Generally, the IMFs do possess physical meaning, however, as with other decompositions, this is not guaranteed (Huang *et al.*, 1998; Zeiler *et al.*, 2010).

2.6. Structural vibration analysis

2.6.1. Industry guidelines

As mentioned in Section 2.3 the rainflow counting method is commonly used to obtain an accumulated fatigue damage estimate from stress measurements. To the author's knowledge, there is no generally accepted method in industry that assesses excessive vibration levels in terms of structural fatigue damage. The internationally accredited registrar and classification society DNV GL presents a simplified method through the vibration class notation (VIBR) to state whether the vibration level is potentially a concern for fatigue (DNV GL, 2019). The former Germanischer Lloyd (GL) classification society presented an assessment diagram to determine if the structural vibration level is excessive and damage is probable (Asmussen, Menzel & Mumm, 2001). The limit curves appear to corroborate the limit for the VIBR class. The BS ISO 20283-2:2008 standard provides guidelines for the measurement and diagnostic evaluation of structural vibration of ships, excited by the propulsion plant. The standard primarily focuses on global vibration and brief notes are provided regarding excessive local vibration levels (BS ISO 20283-2:2008, 2008).

Prompted by the need to determine when slamming is excessive, these three sources have been critically evaluated and integrated to investigate whether vibration levels experienced by the SAA II could be a concern for the structural integrity and operational life of the vessel. A summary of the vibration structural analysis specifications is presented in Table 2.1.

Table 2.1: Summary comparison of vibration structural analysis guidelines

	DNV GL	GL	BS ISO 20283-2
Frequency range	4-200 Hz	1-100 Hz	1-80 Hz (Global) 5-100 Hz (local)
Resolution	≥ 400 spectral lines	-	≤ 0.125 Hz
Window	Yes (Flattop)	-	Flattop or Hanning
Time interval	≥ 30 s	-	≥ 60 s
Limit	45 mm/s	30 mm/s (5-100 Hz)	30 mm/s (5-100 Hz)
Parameter	RMS velocity	peak velocity amplitude	peak velocity amplitude

2.6.2. DNV GL

For the structural vibration of steel, vibration velocity levels should not exceed 45 mm/s. Lower vibration levels present a low risk for fatigue cracks. Measurements should be analysed in the frequency domain using FFT techniques. A window function is required for an accurate representation of signal component amplitude values in the frequency spectra, for example, a flattop window (DNV GL, 2019). The vibration limit is specified as a root mean square (RMS) vibration velocity value. Wave slamming, however, has been identified as an impulsive event. Therefore, the RMS value is not an appropriate metric to quantify slamming

events. It should also be noted that the limit is applicable to the vessel structure in locations where equipment, machinery and other components are situated. The structure close to the propellers is also considered, however, the vessel structure in cargo areas is not included (DNV GL, 2019).

The criterion is purposefully related to frequencies above 4 Hz, where the stochastic vibration experienced by machinery is less important. However, wave excitation also present stochastic vibration in the lower frequency range (DNV GL, 2019). Most importantly, the frequency range from 4 to 200 Hz excludes the first two vertical bending modes of the SAA II at 2.09 Hz and 3.76 Hz (Van Zijl & Bekker, 2018). The two-node vertical mode is associated with the lowest natural vibration frequency and is the most dominant vibration shape. It is easily excited and produces the highest vertical bending stress amidships (DNV GL, 2018). Therefore, fatigue damage in the midsection is dominated by stresses that are induced by the large vertical bending moment (Mao *et al.*, 2010). As mentioned previously, the hogging experienced by the MOL COMFORT contributed to catastrophic structural failure (Committee on Large Container Ship Safety, 2013). Therefore, it is perceived that the vertical bending mode frequencies, at 2.09 Hz and 3.76 Hz, should be included in a structural analysis.

2.6.3. Germanisher Loyd

Figure 2.11 presents a simplified diagram for the assessment of structural vibration according to the former Germanischer Lloyd (GL) classification society. The two limit curves are derived from a large number of measurements and may be used as a guide when evaluating the risk of fatigue cracks in local ship structures as a consequence of vibration. The limit curves relate to peak amplitude values (Asmussen *et al.*, 2001). By analysing peak amplitudes in the frequency domain, the results may be more indicative of slamming encountered than RMS values. FFT parameters, such as windows, overlap, block size and frequency resolution are not specified. Therefore, caution is necessary when applying the limit curves as these parameters can significantly affect the results.

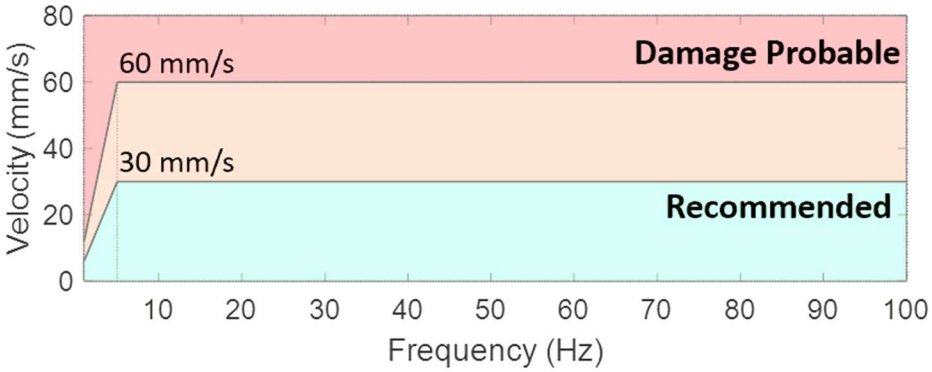

Figure 2.11: Simplified structural vibration limit curves (Asmussen et al.*, 2001)*

It was observed that, in the case of resonance or near-resonance, the risk of inadequate fatigue strength resulting in damage is high (Asmussen *et al.*, 2001). Moreover, the coincidence of structural natural frequencies and excitation frequencies should be avoided and the excitation forces should be minimised if

possible (Lloyd's Register, 2015). This supports the concern that the first two vertical bending modes may significantly influence the structural assessment of the vessel and should be included due to the higher risk of fatigue damage that they pose.

Similar curves are presented by Lloyd's Register (Lloyd's Register, 2006). Locally magnified structural vibrations of steel elements are considered within the frequency range of 5 to 100 Hz. It is recommended that single amplitude peak velocity values remain below ± 30 mm/s at discrete frequencies (Lloyd's Register, 2006, 2015). This corroborates the limit curves presented by Asmussen et al. (2001). Moreover, the limit curves appear to support the limit from the DNV GL VIBR class, but considers the link between displacement, velocity and acceleration for the lower frequency range, below 5 Hz. The peak displacement amplitude is recommended to be lower than 0.25 mm by Lloyd's Register and lower than 1 mm by Germanischer Lloyd. Therefore, the limit curves presented by Germanischer Lloyd are considered to be more conservative.

2.6.4. BS ISO 20283-2:2008

The standard focuses on global vibration. Fatigue due to local structural vibration is considered rare and is briefly considered in an Annex. The standard does also not consider transient vibration excitation such as slamming. The measurements conducted are intended for comparison with theoretical predictions and measurements obtained from other vessels. The measurements should be performed for a frequency range of 1 to 80 Hz. However, if the sea state is greater than 3, with wave heights exceeding 1.25 m and wavelengths larger than 22.5 m (Bertram, 2012), an additional analysis should be conducted after high-pass filtering the signal above 2 Hz. For local structural vibrations a frequency range of 5 to 100 Hz should be considered. Velocity values that exceed 30 mm/s require further attention in order to reduce the risk of structural damage (BS ISO 20283-2:2008, 2008). This agrees with the limit curves presented by Germanischer Lloyd. Similar to GL, it is also recommended that the vibration levels are presented in terms of the peak vibration velocity values.

2.7. Operational modal analysis

Structural resonant modes are of interest because they amplify vibrations. For each mode there is an associated natural frequency at which the structure is oscillating. The modes have a spatial shape and all points along the structure move in or out of phase. The sum of all modes results in a deformation shape at an instant in time. The damping ratio determines the magnitude and duration of the transient whipping response (Brandt, 2011). The ship can be modelled as an undamped elastic free-free beam for low frequency modes and the dynamic whipping response may be obtained through modal superposition. The total vibration response may thus be expressed as a linear combination of the applicable natural vibration modes (Jensen, 2001). Conveniently, whipping typically only involves the first three, low frequency flexural beam modes (Bannister, 1980).

Operational modal analysis derives modal information from operational structural output responses with excitation from typical environmental inputs. Only output measurements are used, as opposed to input-output modal analysis where the input is known. Inputs are assumed to be a realization of a white noise stochastic process with a spatial distribution across the structure (Magalhães & Cunha, 2011). Frequency Domain Decomposition (FDD) is a simple non-parametric frequency-domain OMA technique that is used to identify modes of interest. Unknown inputs $q(t)$ and measured responses $x(t)$ can be related according to Equation (24). The matrix $G_{xx}(j\omega)$ is the power spectral density (PSD) matrix of the responses and $G_{qq}(j\omega)$ is the PSD matrix of the inputs. The complex conjugate and transpose Frequency Response Function (FRF) matrix $H(j\omega)$ are also presented respectively (Brincker, Zhang & Andersen, 2000).

$$G_{xx}(j\omega) = \bar{H}(j\omega)G_{qq}(j\omega)H(j\omega)^T \tag{24}$$

Additionally, any response can be written in modal co-ordinates and the PSD may be transformed to modal coordinates using the mode shape matrix Φ**.** Therefore, $G_{xx}(f)$ represents the PSD matrix of the response measurements in physical coordinates at a frequency line f, and $G_{qq}(f)$ is the PSD matrix in modal coordinates. If the modal coordinates are uncorrelated, then the PSD matrix is diagonal. Therefore, if the mode shapes are orthogonal, Equation (25) becomes a singular value decomposition (SVD) of the vibration response spectral density matrix. The FDD algorithm identifies modal parameters directly from a singular value plot of the spectral density matrix of vibration measurements. The matrix U consists of singular vectors and the diagonal matrix S consists of singular values. The singular values of the spectral density matrix can be used to generate a plot of the auto spectral densities of the modal coordinates. Peaks in the first singular value are used to identify modal frequencies. The corresponding mode shape is acquired from the first singular vector in U (Brincker, Andersen & Jacobsen, 2007).

$$G_{xx}(f) = \Phi\, G_{qq}(f)\, \Phi^T = USU^T \tag{25}$$

2.8. Conclusions

Stern slamming experienced by the SAA II, in combination with whipping induced vertical bending moments, is believed to influence the structural integrity and operational life of the vessel. Wave slamming comprises an impulsive force followed by a transient whipping response. For the detection of wave slamming, accelerometers may record the impulsive response, with a peak acceleration amplitude at the time of impact. Signal processing techniques may then be employed to detect features relating to slamming in both the frequency and time domain. Moreover, vibration levels may indicate if there is potentially a concern for fatigue life and whether damage is probable. Studies have shown that whipping significantly contributes to fatigue damage and that it typically only involves the first three, low frequency flexural beam modes. Therefore, operational modal analysis techniques may be employed to investigate the mode shapes and hull vertical bending response resulting from slamming induced vibration.

3. Vessel and voyages

3.1. The S.A. Agulhas II

Table 3.1 presents the principal vessel specifications. The SAA II is operated by 45 crewmembers and it can accommodate up to 100 passengers in 46 cabins. Electric motors drive the two shaft-lines with four-bladed variable pitch propellers. The diesel generator operates at a constant speed of 750 rpm and comprises of 6 cylinders (Van Zijl & Bekker, 2018). The SAA II has a PC-5 ice rating, which enables it to operate in medium first year ice (0.7 to 1.2 m thick) that may contain old ice inclusions (International Association of Classification Societies, 2016).

Table 3.1: SAA II specifications (Van Zijl & Bekker, 2018)

Length	134.2 m	Speed at MCR*	140 rpm
LBP*	121.25 m	Power at MCR*	4500 kW
Breadth	22 m	Nominal torque	307 kNm
Depth	10.55 m	Main engine maker	Wärtsilä
Classification	DNV	Diesel engine type	6L32
Class notation	1 A1 PC-5/ICE-10	Propeller maker	Rolls Royce
Yard / Year	STX Finland/2012	Blades / Diameter	4 / 4.3m
Electric motor	N3 HXC-1120 LL8	Gross tonnage	12 897 tons

* LBP – Length between perpendiculars, *MCR – Mean Continuous Rating

(a) (b)

Figure 3.1: (a) The S.A. Agulhas II and (b) her flat stern, raised above the water line

The SAA II, shown in Figure 3.1, has a hybrid design, which enables it to navigate through pack ice and operate in open water. The vessel has a raised, flat, extended transom design at the stern, which creates additional deck space for installing scientific container laboratories or cargo storage. The flat, raised stern aids the manoeuvrability of the vessel in ice and reduces propeller ice impacts by affording ample propeller clearance (Omer & Bekker, 2016). The thick rounded bow provides stability and enables the vessel to break ice (Omer, 2016). Bow slamming is anticipated, to a certain extent, for ships with ice-going hull shapes in head seas, due to the increased bow flare angle necessary for successful ice passage (Kapsenberg, 2011). However, the SAA II is pre-disposed to problematic stern slamming, even in calm ocean conditions. Vessels with flat aft designs and relatively small immersion often experience stern slamming, even with wave heights under 1 m (Carlton & Vlašić, 2005). Moreover, the effects of slamming are

exacerbated when the vessel is held stationary during oceanographic activities (Omer & Bekker, 2016).

Research has shown that wave slamming is of critical concern for the vessel structure and equipment. Moderate slamming can result in localized buckling and plastic deformation, which increases maintenance and repair costs. Higher slamming impulses result in unwanted vibrations and whipping which leads to structural fatigue (Henry & Bailey, 1970). Previous research on the SAA II has also shown that wave slamming affects the comfort of crew and passengers on-board. Moreover, vibration caused by wave slamming, has a significant impact on human factors such as sleep, damage to equipment, interference with motor skills and research activities (Omer, 2016).

3.2. Full-scale measurements

Real-time vertical acceleration responses of the ship due to bow and stern slamming were recorded on board the SAA II during the Southern oCean seAsonaL Experiment (SCALE) Winter and Spring Cruises in 2019. Measurements from five DC accelerometers and ten ICP accelerometers, which were placed throughout the vessel structure, are used in the present analysis. An LMS SCADAS Mobile SMO03 master-slave system was employed, in conjunction with LMS Turbine Testing acquisition software, to record data with recording lengths of 5 minutes at a sampling frequency of 2048 Hz. The master and slaves were connected by means of fibre optic cables. Coaxial BNC cables are routed to all measurement locations and connected to each accelerometer by noise-cancelling coaxial ICP-BNC cables. The software initiated and stored the continually generated data. Anti-aliasing filters remove frequency content above half the sampling frequency. The measurement locations and sensors considered are presented in Table 3.2 with reference to Figure 3.2. The sensors and data acquisition system were installed prior to each voyage and removed again afterwards.

Table 3.2: Sensor layout, location, type and sensitivity

Point	Axis	Deck	Side	Description	Type	Sensitivity (mV/g)
1 A	+Z	2	starboard	Steering gear room	ICP	101.9
2 B	+Z	2	starboard	Steering gear room	DC	198.6
3 B	+Z	2	port	Steering gear room	DC	199.2
4 C	+Z	2	starboard	Stern thruster	ICP	100.3
5 C	+Z	2	port	Stern thruster	ICP	97.6
6 D	+Z	2	starboard	Engine store	ICP	101.4
7 D	+Z	2	port	Fresh water room	ICP	101.6
8 E	+Z	9	starboard	Bridge	DC	200.1
9 E	+Z	9	port	Bridge	ICP	99.8
10 F	+Z	3	starboard	Cargo hold aft	ICP	105.2
11 F	+Z	3	port	Cargo hold aft	ICP	102.6
12 G	+Z	3	starboard	Cargo hold forward	ICP	100.6
13 G	+Z	3	port	Cargo hold forward	ICP	102.3
14 H	+Z	4	starboard	Bow chain locker	DC	199.6
15 H	+Z	4	port	Bow chain locker	DC	198.4

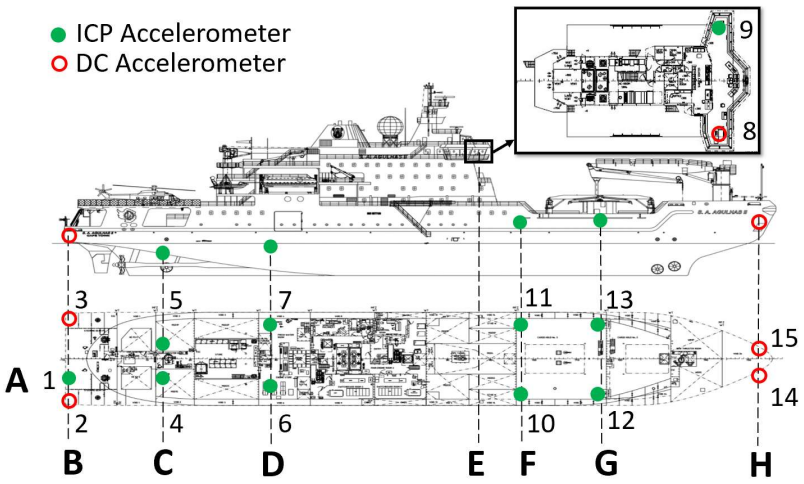

Figure 3.2: Layout of accelerometers used for slamming identification

The sensors were mounted on structural girders to record the global structural response of the vessel to wave slamming. Sensors were situated close to the anticipated slamming locations in the bow and stern of the vessel structure. Sensors were additionally located along the length of the vessel at regular intervals, as close to the waterline as possible (Omer & Bekker, 2016). The operational parameters encountered throughout both voyages were logged hourly in the bridge, by using the automated meteorological and navigational control systems on board the vessel as well as visual observations. Therefore, two sensors located in the bridge are also considered.

During the voyage, the system was continuously monitored to ensure the data quality. Signal characteristics such as the root-mean-square (RMS), mean, kurtosis, skewness and maximum peak value were calculated for each 5-minute record to regularly verify the veracity of the data (Brandt, 2011). Variations in these characteristics were analysed throughout the voyage. Any significant changes in the characteristics were used to identify possible unreliable measurements. If discrepancies in the recordings persisted corrective action could be taken to ensure that sensors and cable connections were secure and that the voltage ranges of the measurement system were set to an appropriate level.

The frequency characteristics of the SAA II are presented in Table 3.3. The first three vertical bending modes are given as determined from a finite element analysis conducted by STX Finland (2010). The damping ratio, ξ , indicates that the vessel is underdamped ($\xi < 1$) for the vertical bending modes (Van Zijl, 2020), which leads to the whipping response. Figure 3.3 illustrates that frequencies close to the first three vertical bending modes are excited in the lower frequency range. There are also several peaks due to machinery excitation.

Table 3.3: SAA II frequency characteristics (Saunders, 2018; Van Zijl, 2020; Van Zijl & Bekker, 2018)

Characteristic	Frequency (Hz)	Damping ratio (%)
1st vertical bending mode	2.09	0.83
2nd vertical bending mode	3.76	0.73
3rd vertical bending mode	5.37	0.85
Shaft frequency at MCR*	2.33	-
Blade pass frequency	9.33	-
Diesel engines	12.50	-

*MCR - Mean Continuous Rating

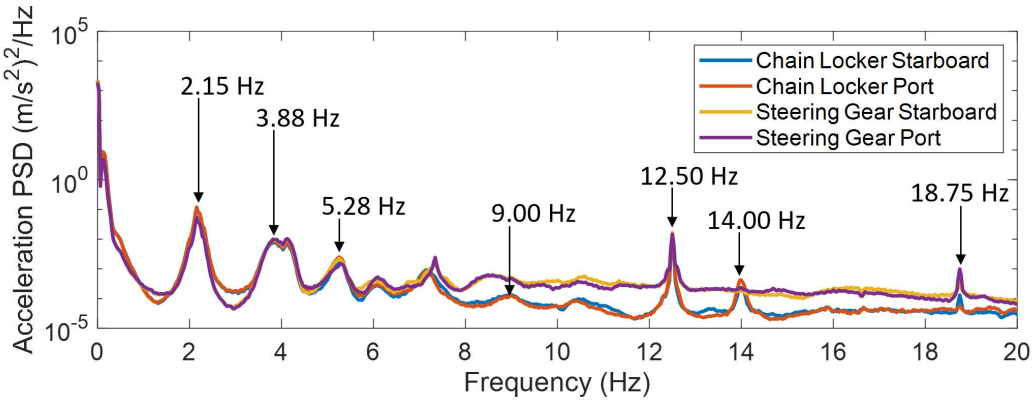

Figure 3.3: PSDs for two channels at the bow and two channels at the stern illustrating the excitation frequencies

3.3. Voyage description

Full-scale measurements were performed during the 2019 SCALE cruises. The cruise route maps are shown in Figure 3.4. The Winter Cruise consisted of a 25-day voyage with a demanding scientific agenda. It took place between 18 July and 12 August 2019. The SAA II departed from Cape Town harbour, she sailed south into the winter pack ice and returned to South Africa. The vessel stopped in East London for the annual SAA II open day awareness programme, which is hosted by the Department of Environmental Affairs (DEA). It remained in the harbour for two days before returning to Cape Town. During this cruise a set of opportunistic open water manoeuvres were conducted to regulate the heading and speed of the vessel. The important dates and time of the open water manoeuvres considered in this thesis are presented in Table 3.4. The time is recorded as Coordinated Universal Time (UTC) ± 00:00.

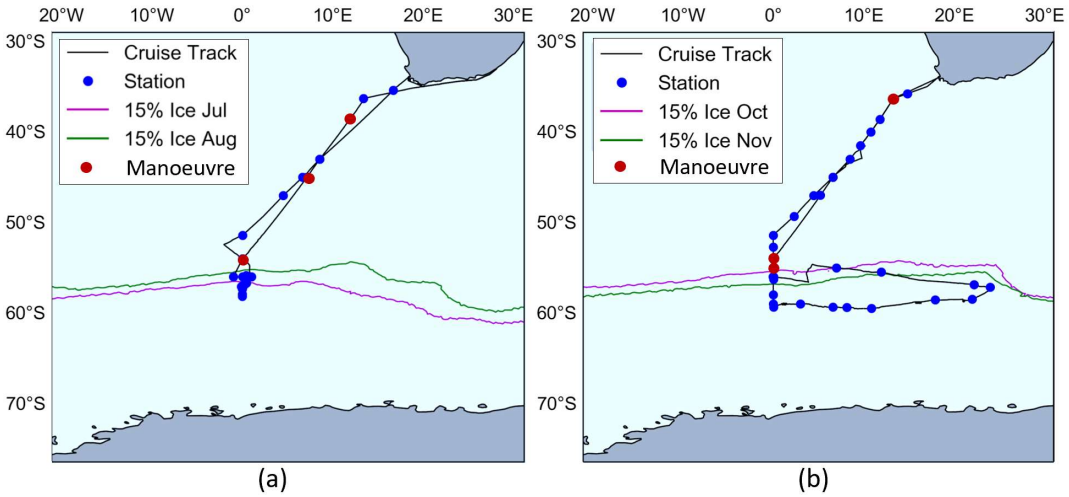

Figure 3.4: Map of (a) Winter and (b) Spring Cruises from the SCALE cruise report, indicating scientific research stations and manoeuvre stations

The Spring Cruise comprised 38 days, from 12 October to 20 November. It is the first voyage that the SAA II has made to the Southern Ocean during spring. The vessel departed from the Cape Town harbour and it returned 8 days earlier than initially planned. A systematic operational study was conducted to regulate the heading and speed of the vessel with more time allocated for dedicated ship manoeuvres to be performed in different sea states. The environmental conditions encountered were recorded throughout the voyages. In general, calmer ocean conditions were encountered in spring.

Table 3.4: Time and location of open water manoeuvres

#	Cruise case	Date	Lat. (°)	Long. (°)	Start time	End time	Total time
1	Winter (0 knots)	22/07/2019	-45.0	7.0	00:30	00:45	1 hr 00 min
		24/07/2019	-54.0	0.0	08:00	08:40	
		04/08/2019	-38.5	11.8	11:25	11:40	
2	Spring (0 knots)	19/10/2019	-54.0	0.0	15:45	17:17	1 hr 32 min
3		18/11/2019	-55.0	-0.3	11:13	12:43	1 hr 30 min
4	Spring (3,6,9 knots)	20/10/2019	-36.2	13.4	15:43	19:32	3 hr 49 min
5		18/11/2019	-36.2	13.4	12:47	16:34	3 hr 47 min

During the Winter Cruise an additional ICP accelerometer was connected to measure the vertical vibration in the starboard steering gear room. Fewer channels could be connected during the Spring Cruise due to module restrictions of the LMS SCADAS Mobile Data Acquisition Units. Therefore, the surplus measurement location (Point 1A) was removed. Moreover, the stern portside DC accelerometer (Point 3B) was inadvertently disconnected from its power supply by crewmembers during the open water manoeuvres performed on 19 October. Consequently, the vibration response to slamming was not measured at this location during the aforementioned set of manoeuvres.

4. Dedicated open water manoeuvres

Stern slamming, in contrast to bow slamming, often occurs less frequently as the ship speed increases. The ship's entrained wave system increases at higher speeds and interrupts the environmental wave system, which protects the aft hull. Slamming is also dependent on the given sea state, which consist of waves induced by local wind superimposed on the underlying swell. The sea state also strongly influences the type of slamming encountered (Carlton & Vlašić 2005). Therefore, the hypothesis is that slamming incidence and severity is dependent on factors such as the speed at which the vessel is traveling (V) and the orientation of the vessel in a given wave state. To investigate operational conditions and the resulting slamming experienced by the vessel a set of open water manoeuvres was conducted.

4.1. Wave parameters

Visual observations of the environmental conditions encountered were conducted every 10 minutes throughout the Winter Cruise and hourly for the duration of the Spring Cruise. The significant wave height is specified as the vertical distance between the trough and crest of a wave and is the average of the highest one-third of waves. The wave period is defined as the average time taken for two successive wave crests to move past a fixed point. The wavelength is the horizontal distance between two successive wave crests and it is calculated according to Equation (26), which is valid for deep water cases. Where T_W represents the mean wave period and λ represents the wavelength. The Beaufort number (Bft) is an empirical measure used to categorize wind speeds and related sea states. It relates these parameters on a scale that ranges from 0 to 12, which represents calm and hurricane ocean conditions respectively (Bertram, 2012).

$$\lambda = 1.56\, {T_W}^2 \tag{26}$$

The wave period T_W is used to calculate the circular frequency ω_c, given in Equation (27), which is needed to calculate the encounter frequency ω_e in Equation (28). Gravitational acceleration g is 9.81 m/s^2. The encounter frequency is also a function of the ship speed V and the encounter angle μ, which are defined according to the fixed coordinate system and a reference coordinate system moving with ship speed V as presented in Figure 4.1. For the stationary vessel the encounter frequency and circular wave frequency are equal, however, for a moving vessel the waves appear to change frequency. The encounter frequency is thus the circular frequency experienced by the ship (Bertram, 2012).

$$\omega_c = \frac{2\pi}{T_W} \tag{27}$$

$$\omega_e = \left| \omega_c - \frac{{\omega_c}^2 V}{g} \cos\mu \right| \tag{28}$$

If the vessel course is against the sea (μ > 90°), the vessel encounters waves at a higher frequency than the incident wave frequency ω_c. If the vessel course is with

the sea (μ < 90°), the encounter frequency is generally lower than the incident wave frequency. An exception is when the vessel passes following waves with short wavelengths. The dimensionless Froude number is the ratio of inertial and gravitational forces and it governs the nature of flow in open channels (Çengel & Cimbala, 2014). The Froude number is calculated according to Equation (29) and if the relation in Equation (31) holds true, the vessel passes the waves (Bertram, 2012).

$$F_n = \frac{V}{\sqrt{gL}} \tag{29}$$

$$\zeta = \frac{0.4}{\cos\mu}\sqrt{\frac{\lambda}{L}} \tag{30}$$

$$F_n > \zeta \tag{31}$$

4.2. Design for manoeuvres

Two separate types of manoeuvres were conducted. For the first manoeuvre, the vessel was held on station, in similar environmental conditions, and the relative direction of waves approaching the vessel was regulated. This relative heading is demonstrated in Figure 4.1, where the red arrows labelled A to E indicate different vessel orientations, with the waves approaching the vessel at 0°, 45°, 90°, 135° and 180° respectively. Position A indicates head on waves, approaching at the bow. Position E indicates following waves, approaching at the stern.

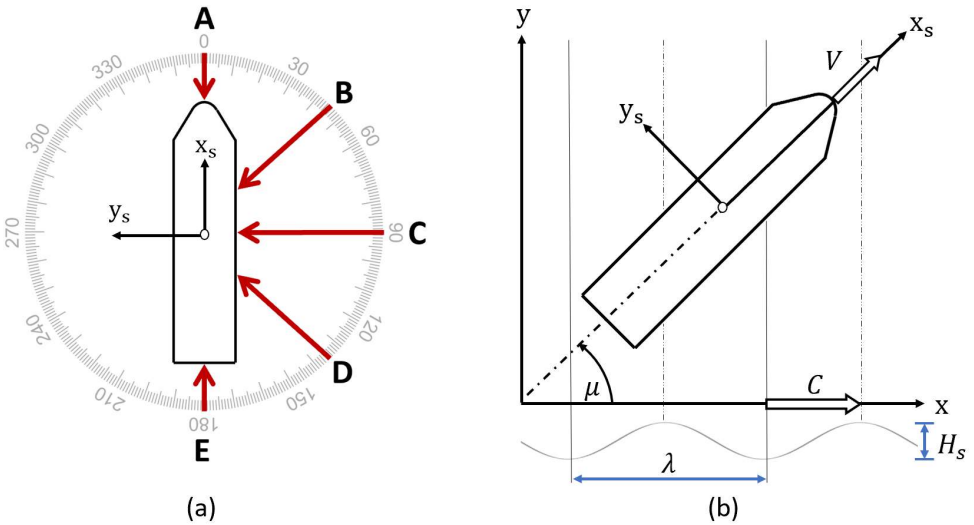

Figure 4.1: (a) Relative heading for ship axis system with waves approaching the vessel at (A) 0°, (B) 45°, (C) 90°, (D) 135°, (E) 180°, (b) Encounter angle for fixed x-y reference system (Bertram, 2012)

The ship was maintained in a stationary position for 15 minutes at each angle, or the respective mirror image angle, with waves approaching on the portside. A total of one and a half hours of ship time was used to complete one such manoeuvre. This manoeuvre sequence was repeated a total of three times during the winter

and Spring Cruises for various sea states. During the Winter Cruise, however, no data was recorded for beam waves, which approach the vessel at 90°.

Observers, situated in the bridge for the duration of the manoeuvres recorded the operational conditions of the vessel and wave state encountered as seen in Figure 4.2. Observers also noted how often slamming was encountered. A slam event was identified by observers experiencing the global response of the vessel structure following an impulsive event, which is often felt as vibrations that propagate throughout the vessel structure, and is known as whipping.

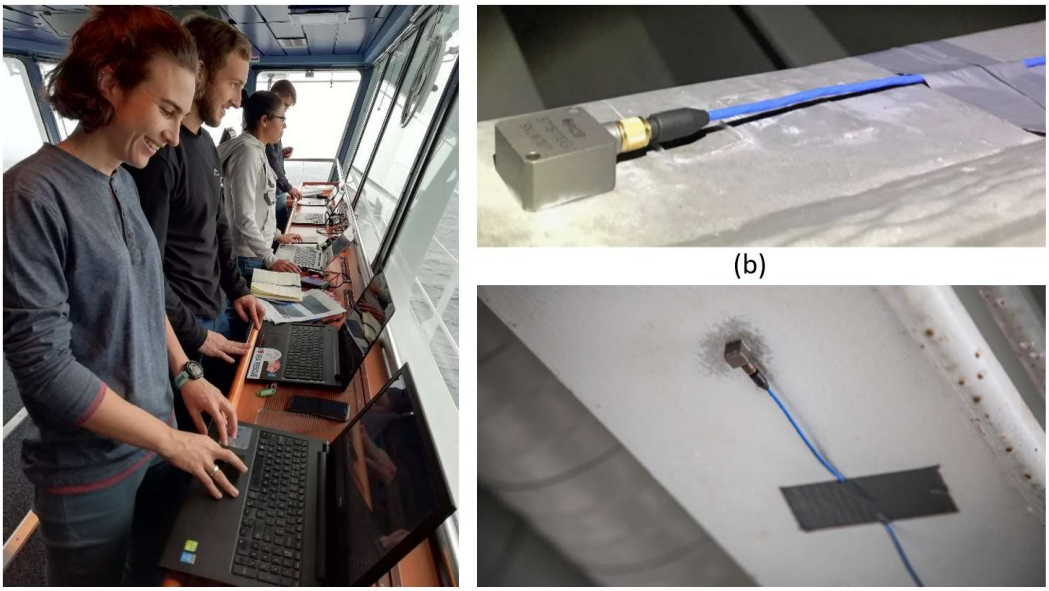

Figure 4.2: (a) Wave state and slamming observations conducted from the bridge by human sensors, (b) DC accelerometer, (c) ICP accelerometer

The second manoeuvre consisted of maintaining the relative heading of the vessel for the wave state encountered and travelling at a specified constant speed. For example, the vessel was orientated with waves approaching head on, then the course would be maintained and the vessel would obtain a constant speed of 3 knots. The relative heading and speed would be kept constant for a total of 15 minutes. The vessel speed would then be adjusted to a constant speed of 6 knots, followed by a constant speed of 9 knots and maintained at each speed for a total of 15 minutes. This was repeated for each of the relative headings considered, namely 0°, 45°, 135° and 180°. The complete sequence of the manoeuvre was performed twice during the Spring Cruise. Each complete case study took around three hours and fifty minutes of ship time.

The crew were consulted regarding the chosen vessel speeds. The SAA II can typically reach a velocity of 12 knots. When the ship is in Ice Mode, all four engines are employed and the vessel can reach a maximum velocity of 16 knots (Department of Environmental Affairs, 2019). However, environmental conditions significantly influence speed capabilities, for example, the swell height and the speed and direction of the wind. It was considered that the vessel is often able to

travel at 10 knots, therefore, to minimise limitations due to environmental conditions, a maximum velocity of 9 knots was selected for the experiment. Moreover, to ensure an incremental range in operational conditions with low, moderate and relatively high-speed case studies, the velocities considered were set to 3, 6 and 9 knots. Environmental factors such as wind and ocean currents also influence the capability of maintaining a constant relative vessel heading as well as the economy of fuel consumption.

4.3. Manoeuvre operational conditions

Table 4.1 presents the observed ocean conditions as well as the mean wave period (T_W) and the average significant wave height (H_s) of the combined wind waves and swell obtained from the ERA5 Climate Data Store (CDS). ERA5 is the fifth generation of the European Centre for Medium-Range Weather Forecasts (ECMWF) and is a global climate reanalysis tool, which provides hourly data of atmospheric and sea-state parameters (Copernicus Climate Change Service (C3S), 2018). The respective average wave heights are plotted in Figure 4.3 (a) with an observer error between 7% and 34% when compared to ERA5. The wave periods plotted in Figure 4.3 (b) indicate an observer error between 1% and 24%.

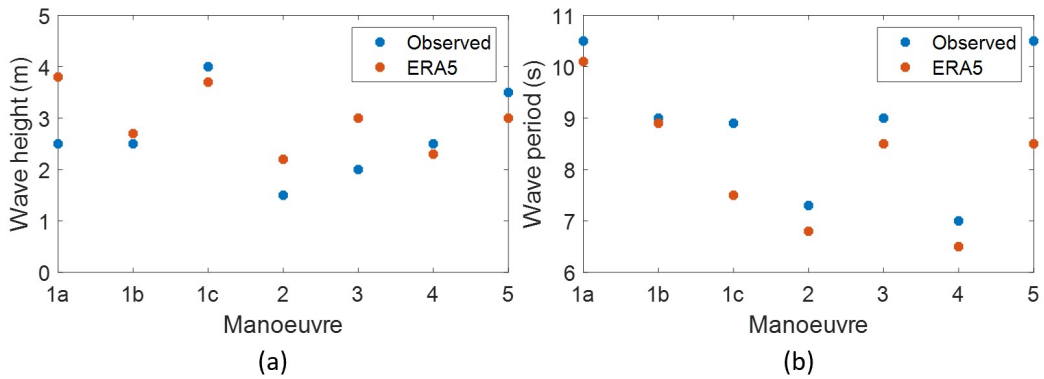

Figure 4.3: The mean observed and the corresponding ERA5 (a) wave height and (b) wave period

Table 4.1: Open water manoeuvre operational conditions

Case	Date (2019)	V (kn)	Wind speed (kn)	Observed			ERA5		Wavelength	
				Bft	H_s (m)	T_W (s)	H_s (m)	T_W (s)	λ (m)	λ/L
1a	22/07	0	16-17	5	2-3	10.5	3.8	10.1	159	1.19
1b	24/07	0	16-18	5	2-3	9.0	2.7	8.9	124	0.92
1c	04/08	0	31-42	8	3-5	8.9	3.7	7.5	88	0.65
2	19/10	0	13-31	5	1-2	7.3	2.2	6.8	72	0.54
3	18/11	0	19-26	5	1-3	9.0	3.0	8.5	113	0.84
4	20/10	3,6,9	12-39	4	1-4	7.0	2.3	6.5	66	0.49
5	18/11	3,6,9	16-28	5	2-5	10.5	3.0	8.5	113	0.84

The visual observations correspond reasonably well with the ERA5 data. The observed significant wave height (H_s) is presented as the average range. The wind speed range given in Table 4.1 was recorded at 10-minute intervals by the

automated meteorological and navigational control systems on board the vessel. The wavelength is calculated using the ERA5 mean wave period according to Equation (26). The wavelength is considered with regard to the length of the vessel (L), which is 134 m. Therefore, the wavelength is generally shorter than the vessel length, as seen for the ratio (λ/L), given in Table 4.1.

Case 1 consists of manoeuvres conducted throughout the Winter Cruise with the vessel held on station. The experiment was conducted on three separate occasions to accommodate the demanding scientific agenda. The subsequent cases present results recorded during the Spring Cruise during more focused manoeuvres. Consequently, Case 1 shows large variations in the environmental conditions. The larger wave heights reaching 5 m and high wind speed of 42 knots were recorded on 4 August when the vessel was held on station with head on waves. More consistent parameters were recorded for the other relative angles considered (45°, 135° and 180°), with wave heights between 2 to 3 m and wind speeds of around 17 kn. Nevertheless, during Case 2 and 3 the wind speed also increased significantly, although it was recorded sequentially over a period of approximately 90 minutes.

The circular frequency and encounter frequency are given in Table 4.2. The Froude number was also calculated according to Equation (29) and assessed according to Equation (31) of Section 4.1. This confirmed that for a relative heading of 0° and 45° (μ > 90°) the vessel passes the waves, whereas for a relative heading of 135° and 180° (μ < 90°) the waves pass the vessel, for the manoeuvres at speed considered.

Table 4.2: Encounter frequency of waves

Stationary Manoeuvres											
Case	Relative heading (°)			ω_c (rad/s)	V (kn)	ω_e (rad/s)		f_e (Hz)		
1a	45			0.62	0	0.62		0.10		
1b	135, 180			0.71	0	0.71		0.11		
1c	0			0.84	0	0.84		0.13		
2	0, 45, 90, 135, 180			0.92	0	0.92		0.15		
3	0, 45, 90, 135, 180			0.74	0	0.74		0.12		
Manoeuvres at speed											
Case	Relative heading (°)	ω_c (rad/s)	μ (°)	ζ	ω_e (rad/s)			f_e (Hz)		
					V=3 (kn)	V=6 (kn)	V=9 (kn)	V=3 (kn)	V=6 (kn)	V=9 (kn)
4	0	0.97	180	-0.28	1.11	1.26	1.41	0.18	0.20	0.22
	45		135	-0.40	1.07	1.17	1.28	0.17	0.19	0.20
	135		45	0.40	0.86	0.76	0.65	0.14	0.12	0.10
	180		0	0.28	0.82	0.67	0.53	0.13	0.11	0.08
5	0	0.74	180	-0.37	0.83	0.91	1.00	0.13	0.15	0.16
	45		135	-0.52	0.80	0.86	0.92	0.13	0.14	0.15
	135		45	0.52	0.68	0.62	0.56	0.11	0.10	0.09
	180		0	0.37	0.65	0.57	0.48	0.10	0.09	0.08
				F_n	0.04	0.09	0.13	0.04	0.09	0.13

5. Slamming detection concept implementation

5.1. Slamming detection overview

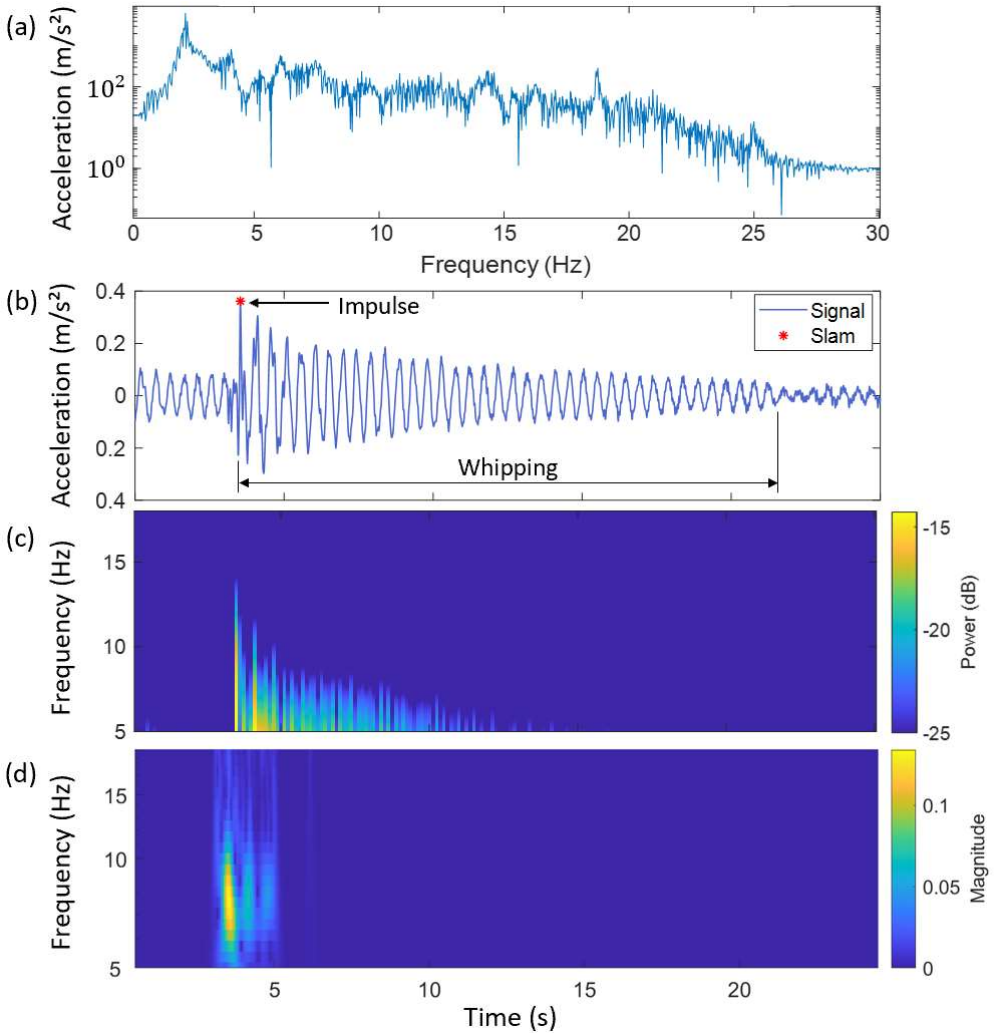

Figure 5.1: Slamming event recorded by an ICP accelerometer at the port side stern thruster, represented in (a) the frequency domain, (b) the time domain, (c) a time and frequency domain spectrogram image (d) a time and frequency domain scalogram image

Wave slamming produces an impulsive signal with a large acceleration amplitude at the time of the impact, followed by a transient whipping response as illustrated in Figure 5.1 (b). The impulsive event, followed by transient oscillations, is an anomaly in the data. The Fast Fourier Transform (FFT) is one method that transforms digitised data from the time domain to the frequency domain, as illustrated in Figure 5.1 (a). Wave slamming results in broadband excitation. Therefore, the impact does not excite the system at a single frequency; instead, it excites a range of frequencies. Spectrograms may be implemented to depict both the frequency and time components of a signal, where the impact appears as a line across numerous frequencies, as seen in Figure 5.1 (c). The figure also shows prominent frequency components that are excited on the lower end of the frequency spectrum following the impulsive event. Therefore, the whipping

presents lower frequency signal content with a smaller magnitude. Similarly, a scalogram image, generated using a continuous Morlet wavelet transform, also presents both time and frequency information as shown in Figure 5.1 (d). For longer analysis time periods the impulsive slamming line features are finer and more distinct. These lines can then be detected across higher frequencies due to abrupt changes in pixel brightness.

Three concepts were generated and implemented to detect slamming events within the acceleration time signal. The process diagram in Figure 5.2 illustrates the basic framework for each concept, as discussed in the following Sections. For all three methods, the acceleration signals are selected and pre-processed. Both the continuous Morlet wavelet transform and the spectrogram method rely on a line detection algorithm to extract slamming features from the time-frequency images. The extracted slam time and corresponding acceleration values from the three methods are further investigated as described in Section 5.7. A single slamming event that is detected across multiple channels is then represented as a single peak acceleration amplitude at the earliest time extracted.

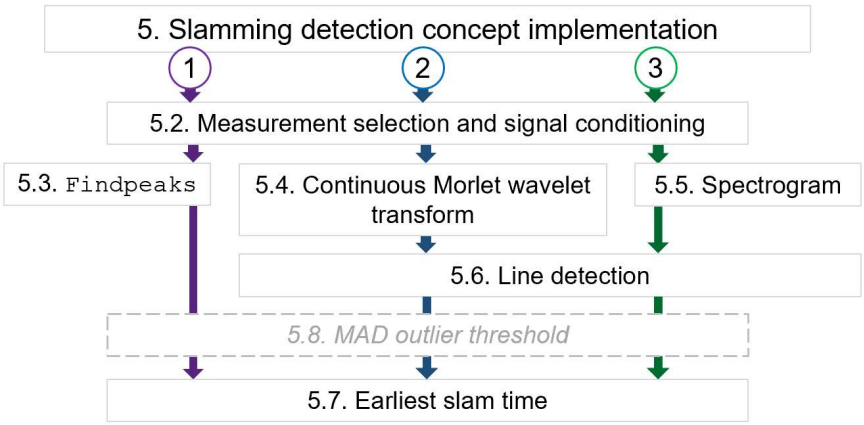

Figure 5.2: Slamming detection concepts process diagram associated with the following sections

5.2. Measurement selection and signal conditioning

Specific inputs may be adjusted according to user requirements. The data folder directory is selected and the first and last files to be processed are entered. A total of 30 channels recorded data during the voyages, however, only 15 channels are considered for the present analysis, as indicated in Figure 3.2. The data for the duration of interest is located and loaded. The 5-minute recording files are concatenated for each channel to generate a signal for the duration of interest before signal conditioning is implemented. However, the three signal processing methods all analyse the signal according to the 5-minute recording intervals of the generic file structure. Folders are also created within the data folder directory to store the results.

As the sensors include DC accelerometers, some acceleration measurements contain low frequency information on rigid body motion. Therefore, the acceleration signals were first conditioned by de-trending to remove the DC zero offset before

applying filtering. A high-pass filter is required to remove rigid body motion and allow ICP and DC time signals to be compared. As recommended by the BS ISO 20283-2 standard (BS ISO 20283-2:2008, 2008) the signal is high-pass filtered above 2 Hz so that all sea states are accounted for. A High-pass Butterworth filter, with a pass band of 2 Hz, was employed. To eliminate filter settling artefacts in the time domain, the detrended signals are padded with zero data prior to filtering.

The Butterworth infinite impulse response (IIR) filter is a common filter with a maximum flat gain characteristic and a relatively linear phase characteristic (Brandt, 2011). The normal high-pass Butterworth filter magnitude and phase response as well as the group delay are illustrated in Figure 5.3. The phase should be linear with frequency so that the same relative phase between different frequencies is maintained and not distorted after passing the signal through the filter. To produce linear phase characteristics the MATLAB `filtfilt` command is used. The data is therefore filtered normally in the time direction and then the filter is run backwards in time. The output is also scaled so that the filter gain characteristic is the same as it would be for a filter applied conventionally, only in the time direction. Most digital filters introduce a time delay by some number of samples. For a linear-phase filter the group delay is constant and not frequency dependant (Brandt, 2011). The high-pass filtered and unfiltered signals were compared to ensure that the output was reasonable, without a significant time delay, as it is desirable to extract the time at which slamming events occur.

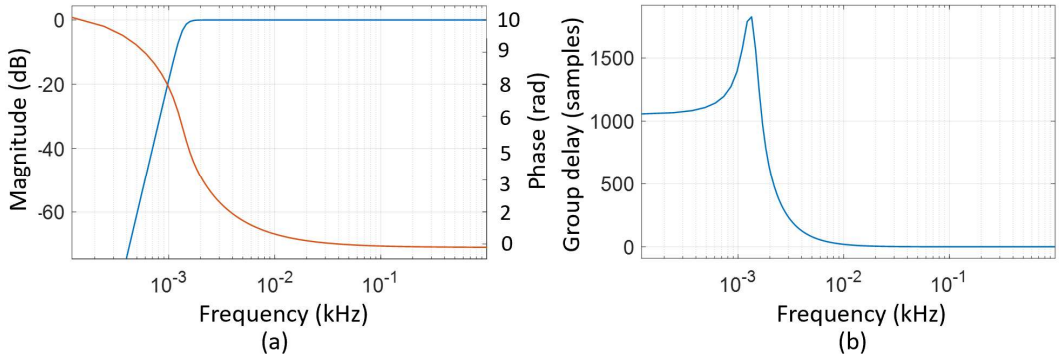

Figure 5.3: High-pass Butterworth filter (a) magnitude and phase response, (b) group delay

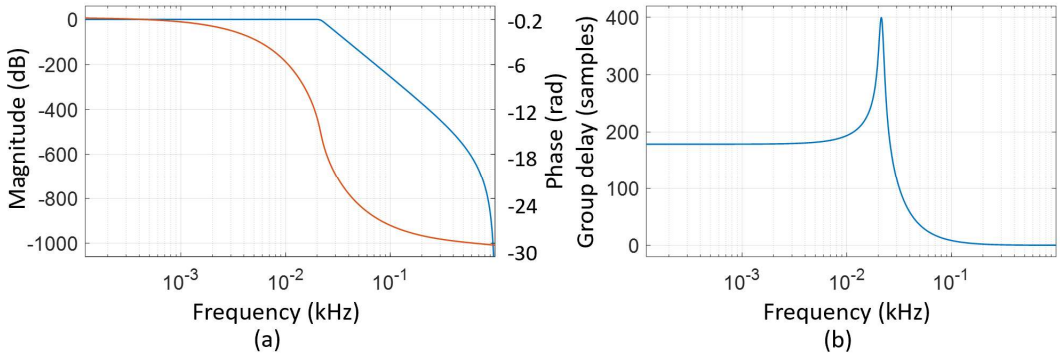

Figure 5.4: Low-pass Butterworth filter (a) magnitude and phase response, (b) group delay

A low-pass Butterworth filter with a pass band of 20 Hz was applied to remove higher engine harmonics. It was also identified that excitation frequencies of wave slamming on the SAA II are best detected in the frequency range between 2 Hz and 16 Hz (Bekker, Van Zijl, *et al.*, 2018). Moreover, the frequency range from 5 to 20 Hz is considered significant for global ship vibration and natural frequencies up to 20 Hz are often modelled and analysed (Bertram, 2012; Lloyd's Register, 2015). The normal low-pass Butterworth filter magnitude, phase and group delay response are shown in Figure 5.4. The `filtfilt` function is again used to produce linear phase characteristics. However, it introduces transients at the start and end of the signal, therefore the first and last 0.2 seconds of the signal for the duration of interest had to be removed after filtering to eliminate filter transients. The amplitude of the filtered signal is represented well in the time domain due to the high oversampling ratio. Accurate peak acceleration amplitudes may thus be extracted from the time signal. The frequency domain spectrum is also accurate as the sampling frequency of 2048 Hz is well above the Nyquist frequency for the frequency range of interest. The filtered signal is demonstrated in Figure 5.5 for an ICP and DC signal.

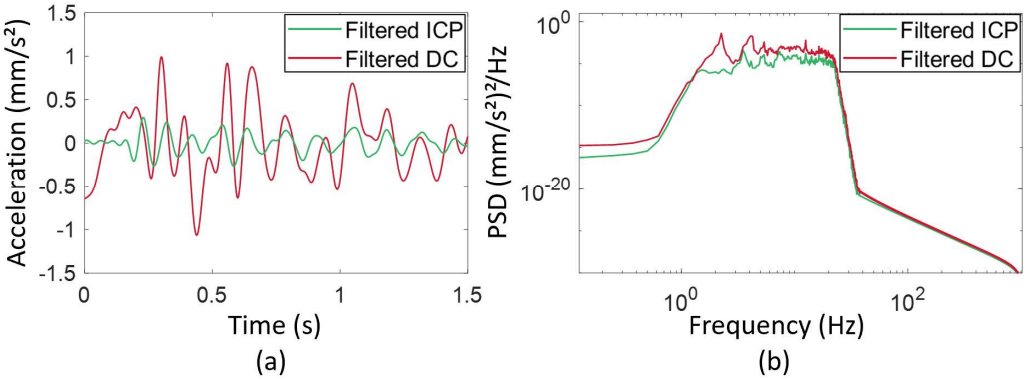

Figure 5.5: Filtered ICP and DC signals recorded in the steering gear room during the Winter Cruise in (a) the time domain and (b) a PSD of the frequency domain illustrating the signal filtered between 2 and 20 Hz (a Hanning window was applied and the resolution is 0.125 Hz)

5.3. `Findpeaks`

```
minpeakdist=round(60/10/(1/fs));
[acceleration,locs]=findpeaks(sig_thresh,'npeaks',...
            tRecord,'minpeakdistance',minpeakdist,...
            'minpeakprominence',Thresh);
```
(1)

The `findpeaks` MATLAB function is a concept for peak detection and it is used to detect local maxima in a signal. The full code is shown in Appendix B.1.2., but code extract (1) shows some important parameters. It requires the minimum distance between adjacent peaks to be determined and specified according to the number of samples. The maximum number of peaks that may be detected is also specified (MathWorks, 2007). An initial guess is required to set a minimum time of recurrence. For the present analysis the maximum number of slams was set to be 10 slams per minute, which is equivalent to one slam every 6 seconds. This sets the minimum distance between adjacent peaks to be 12288 sample points as

indicated in Figure 5.6 (b). The minimum time between peaks should be set so that the whipping response may be ignored. However, an impulsive wave slam that occurs shortly after a previous slam may also accidentally be missed or ignored.

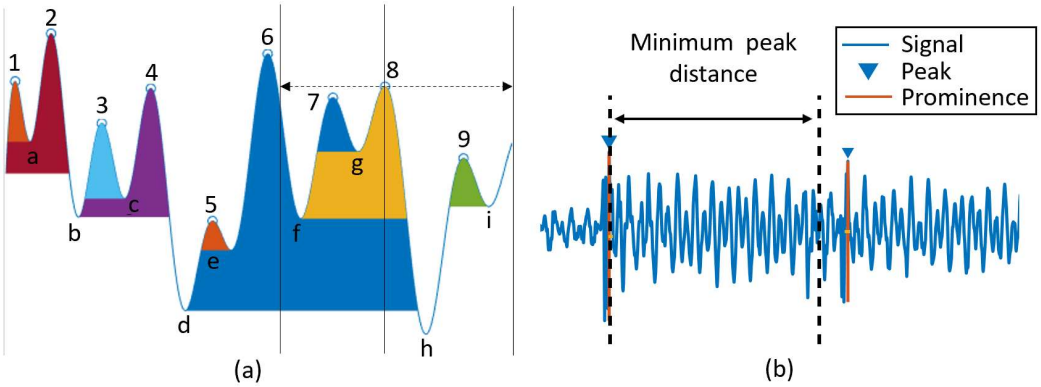

Figure 5.6: Parameters of the `findpeaks` *function* (MathWorks, 2007)

The minimum peak prominence that should be detected also needs to be specified. This is a measure of how much the peak protrudes from the rest of the signal due to its relative proximity to other peaks and its inherent height. The peak prominence is the minimum vertical distance on either side of a peak that the signal needs to descend before either the signal ascends to a level higher than the peak or the signal endpoint is reached. A low and isolated peak can be more prominent than a higher peak that is surrounded by a range of tall peaks. The method for determining the prominence is illustrated in Figure 5.6 (a). With reference to peak 8 as an example, a horizontal line is extended to either side of the peak until it crosses the signal due to the presence of a higher peak (left side) or a signal endpoint is reached (right side). The local minima of the signal within each of the two intervals are determined to be points h and f. The higher of these two local minima, point f, is used as a reference level and the height of the peak above this level is defined as the peak prominence (MathWorks, 2007).

A threshold is required to establish the minimum peak prominence, above which peaks should be detected. Setting a reasonable threshold is important for the peak detection process. If peak amplitudes are very close to the threshold value, or if a significant number of the peaks fall slightly below the threshold, the algorithm will fail to identify these peaks. In contrast, if the threshold is set too low, additional peaks are incorrectly identified. In the second case, the parameter that specifies the minimum distance between nearby peaks dominates as a constraining factor for peak detection. Whether the algorithm fails to detect peaks or if it detects false peaks, it will not present an accurate measurement of slamming events.

The peaks due to slamming events are considered statistical outliers as the value significantly deviates from the value of the surrounding data points and the standard statistical properties of a distribution. The MATLAB `isoutlier` function returns the upper and lower thresholds for determining outliers, as well as the centre value of a data distribution. The function employs the median absolute deviation (MAD) to detect outliers present in the data, thus an outlier is defined as a value that is further than three scaled median absolute deviations away from the

median value (MathWorks, 2017a). Three MAD is considered a conservative approach to select an outlier threshold (Leys, Ley, Klein, Bernard & Licata, 2013). Therefore, only acceleration values that exceed the lower and upper bounds of the thresholds are considered outliers and may be extracted.

The mean and standard deviation are commonly used to detect outliers; however, they are sensitive to outliers. The MAD is a more robust measure of how spread out data is and it is unaffected by sample size. It is also insensitive to the presence of outliers or non-normal distributions (Leys *et al.*, 2013). The breakdown point is the maximum number of extreme values, for example, values that are set to infinity, which can be introduced into a sample without the estimator yielding a false result. A single infinite value will result in the mean becoming infinite. Therefore, the breakdown point is zero. The median is more robust and is only affected when more than half of the values are contaminated, resulting in a breakdown point of 0.5 (Leys *et al.*, 2013). The MAD is determined according to Equation (32). The median is calculated and subtracted from each constituent of the data series. The absolute values of the differences are determined, placed in ascending order and the median is determined once more. The constant η is associated with the normality of the data distribution (Leys *et al.*, 2013).

$$MAD = \eta\, M_i\left(\left|x_i - M_j\left(x_j\right)\right|\right) \tag{32}$$

Due to variable ocean conditions the noise floor of the signal shifts up and down. The noise floor also varies for each sensor. The outlier threshold is determined for the entire duration of the signal being considered and is therefore tailored for each individual signal. Figure 5.7 illustrates how the outlier threshold changes for two different operational conditions. Both signals were recorded in the starboard steering gear room. The environmental conditions encountered were similar; however, the relative orientation of the vessel in a given wave state was changed. The first 5 minutes show a signal record for the stationary vessel confronting following waves. The following 5 minutes show a signal record for the vessel encountering head on waves. It can be seen that the threshold is set higher for following waves due to a higher noise floor, with larger and more frequent peaks present. In contrast, the threshold is set lower for head on waves due to a lower noise floor with fewer, smaller peaks present.

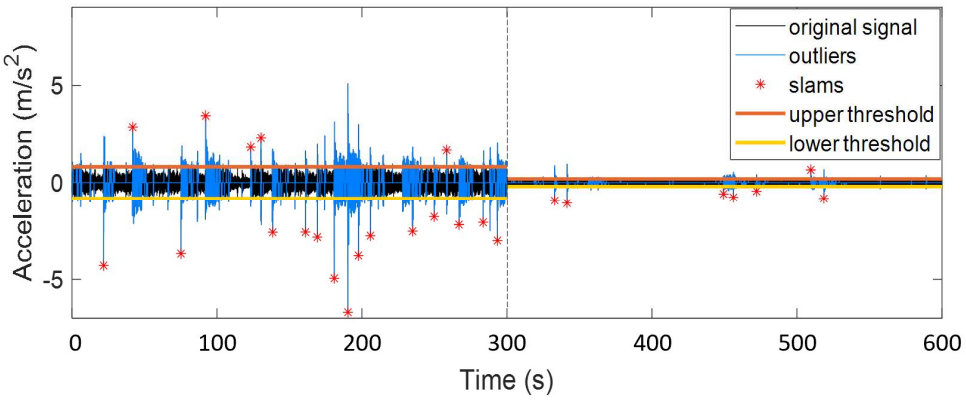

Figure 5.7: Outlier threshold for two different operational conditions

The peak detection procedure is shown in Figure 5.8. For Step 2 of the procedure, with reference to the code extract (2), the upper and lower threshold is statistically determined and the larger of the two threshold magnitudes is set as the absolute threshold. The threshold is used as a guideline in the `findpeaks` function for the minimum peak prominence required. This reduces the prospect of detecting false peaks with the caveat that a threshold is required for analysis. In Step 3 the absolute values of the original signal are considered because `findpeaks` only extracts positive peaks. The peaks that are detected are shown in Step 4. It is evident that the slams extracted are considered statistical outliers.

```
[TFb,Lb,Ub,Cb] = isoutlier(y(y~=0));
Thresh=max(abs([Ub Lb]));
```
(2)

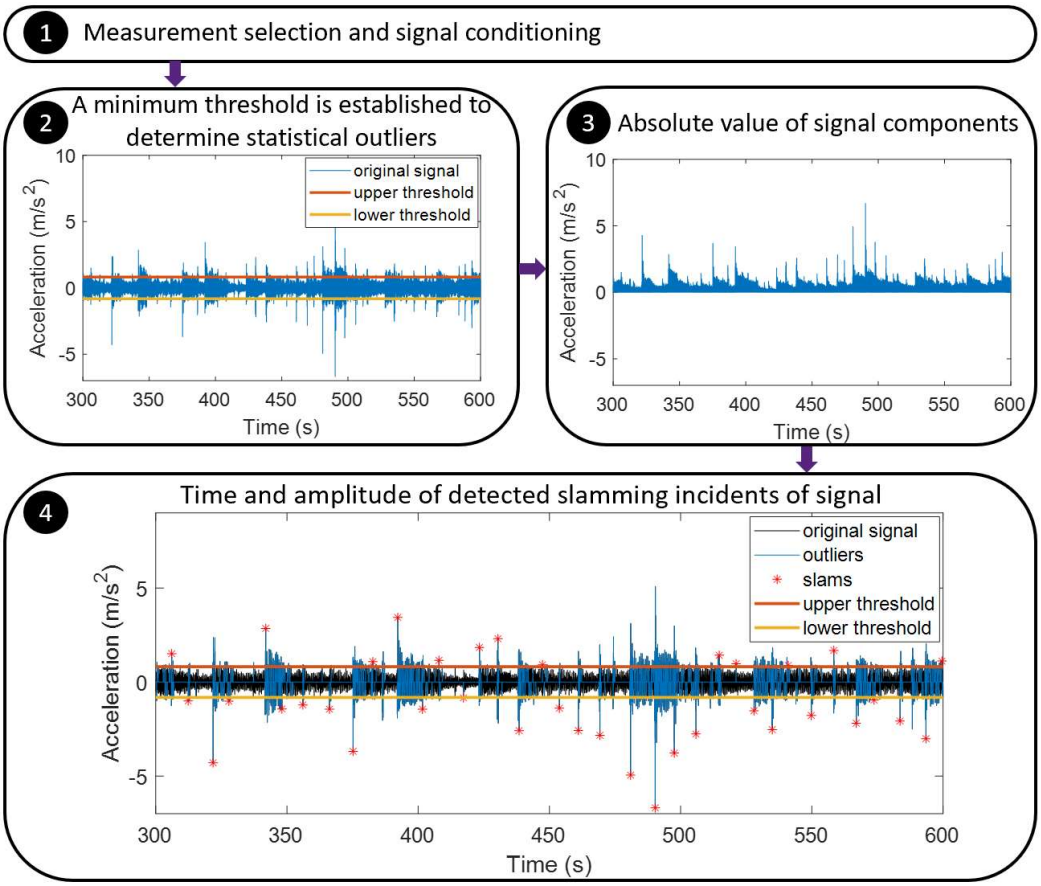

Figure 5.8: `Findpeaks` slamming detection procedure

5.4. Continuous Morlet wavelet transform

Empirical mode decomposition is used to decompose the signal into its oscillatory modes, called intrinsic mode functions (Huang *et al.*, 1998). The first IMF is obtained through a sifting process and generally contains the highest frequency component of the signal as described in Section 2.5.3 and is obtained according to code extract (3). It is noted that EMD may result in border distortion and an incorrect instantaneous frequency may be calculated at both ends of the signal. The EMD may also produce undesirable low-frequency components (Xun & Yan,

2008). However, only frequencies in the higher frequency range will be considered for wave slamming identification and border distortion does not present a problem for broadband frequency line detection, especially since lines are not detected directly at the scalogram borders.

```
[imf]=emd(Y_f(:,idx),'Interpolation','pchip');
numIMF=1;
IMF=imf(:,numIMF);
```
(3)

Similar to the `findpeaks` method, the median absolute deviation is used to detect outliers for the IMF signal. All absolute value signal components above the statistically determined threshold are set to one and all components below are set to zero. The product of the resulting vector and the original signal is then determined. Therefore, signal components with an absolute magnitude larger than the threshold are preserved, whereas components which lie below the threshold are set to zero and neglected. The continuous Morlet wavelet transform is applied to the resulting signal. The process of obtaining a clearer image is demonstrated in Figure 5.9. Using the first IMF component generates a clearer signal, containing high frequency signal content. Applying a threshold further enables a clearer image to be created, with more distinct lines which represent slam events and fewer lines that may be present due to noise. The prospect of detecting false peaks is thereby reduced with the caveat that a threshold is used for analysis.

The function `cwtfilterbank` in code extract (4) creates a continuous wavelet transform (cwt) filter bank. The filter bank precomputes the filters once and then passes them as an input to the `cwt` function. This improves the computational efficiency when multiple signals are analysed (MathWorks, 2018b). The properties of the filter bank are specified as input arguments. The length of the signal is specified as the number of samples present in a 5-minute recording. The analysis wavelet type is stipulated as `'amor'`, which denotes the Morlet wavelet. The sampling frequency of the signal is conveyed and the frequency limits are set as values in Hertz.

```
fb=cwtfilterbank('SignalLength',tRecord/period,...
    'Wavelet','amor','SamplingFrequency',fs,...
    'FrequencyLimits',[10 15]);
cwt(signal_thresh,'FilterBank',fb);
```
(4)

Previous research investigated using the Morlet wavelet to create a scalogram image with striated slamming features. It was identified that the excitation frequencies of wave slamming on the SAA II can be detected in the frequency range between 2 Hz and 16 Hz (Bekker, Van Zijl, *et al.*, 2018). However, the previous study did not incorporate the EMD and thresholding steps shown in Figure 5.9. The scalogram image for the present analysis is set to analyse signal components in the higher frequency range, with frequencies between 10 and 15 Hz. Therefore, the execution time is reduced and the line detection procedure can be applied to a clearer image which presents the frequencies of interest with a good time resolution. The scalogram represents the absolute value of the continuous wavelet transform, plotted as a function of time and frequency. The `cwt`

function uses L1 normalization, therefore, equal amplitude oscillatory signal components at different scales will have equal magnitude in the cwt. This is considered a more accurate representation of the signal than L2 normalisation, which reduces high-frequency amplitudes (MathWorks, 2016).

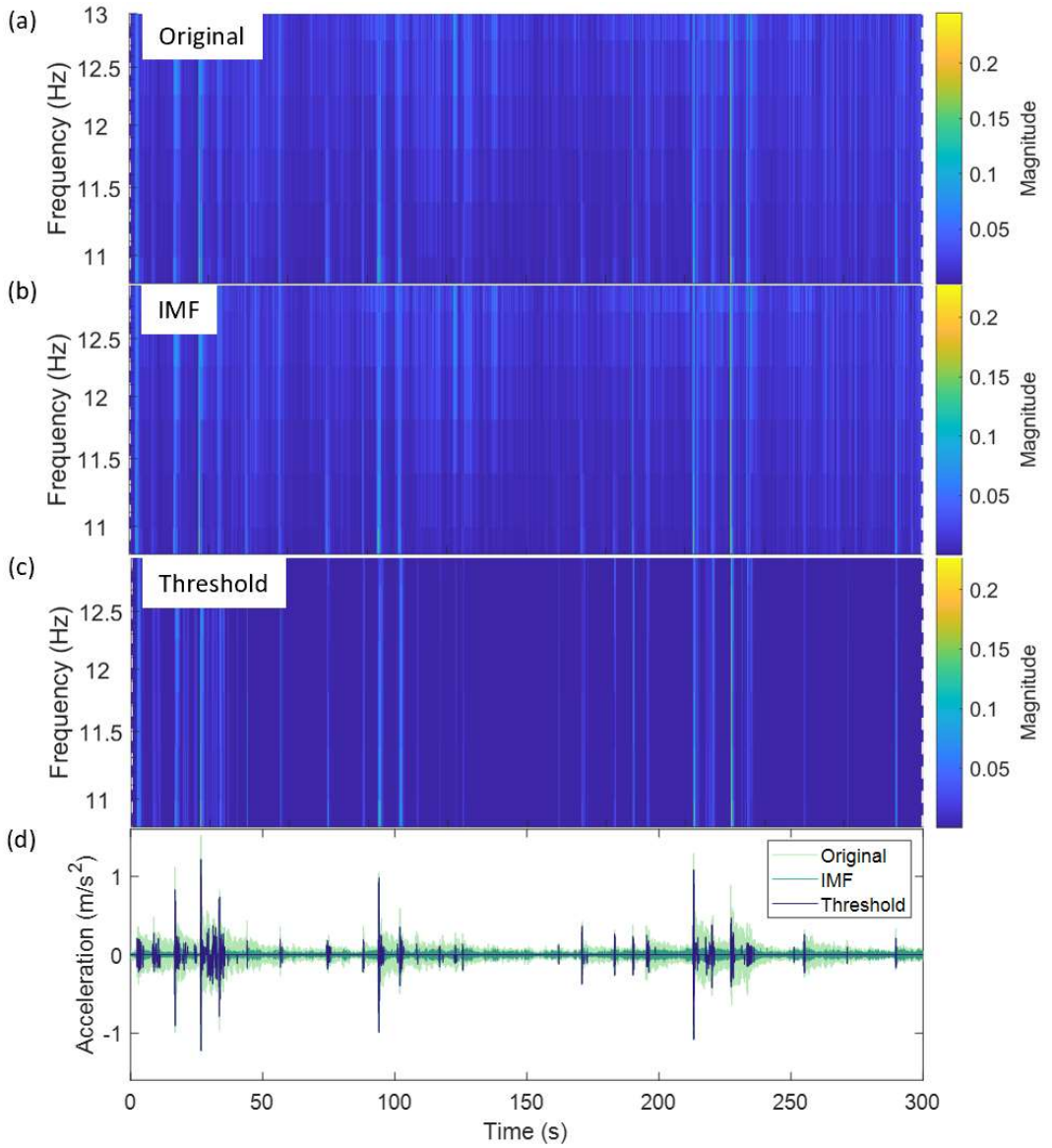

Figure 5.9: A scalogram image generated from (a) the original signal, (b) the first IMF of EMD, (c) the first IMF after a threshold is applied and (d) shows the time domain representation of the signal used in (a) to (c)

Lines are detected in the scalogram image as discussed in Section 5.6. The detected lines are scaled to the original signal, not the IMF signal, and only impacts larger than the IMF determined threshold are extracted. The important parameters, namely the acceleration amplitude extracted at the time of a slam impact, are saved in the results folder. The full code is shown in Appendix B.1.4.

5.5. Spectrogram

The MATLAB function `pspectrum` generates the short-term, time-localized power spectrum of the signal (MathWorks, 2017b). As shown in code extract (5) the sampling frequency and the spectrogram method is specified. The whipping presents lower frequency signal content with a smaller magnitude. The frequency limits are therefore set to analyse the higher frequency signal content. Figure 3.3 indicates a high peak in all four PSDs at 12.5 Hz, which is the diesel engine rotation frequency, and 18.75 Hz. Therefore, the frequency limits are set to the frequency range between 13 and 18 Hz with a lower energy content. The energy content within this level will therefore increase more noticeably due to broadband frequency slamming excitation, with little influence from the energy content due to modal frequencies and machinery excitation. The impulsive slamming line features can then be detected across higher frequencies due to abrupt changes in pixel brightness.

```
if ismember(idx,DC)==1
 pspectrum(ysect,fs,'spectrogram','FrequencyLimits',...
 [13 18],'Leakage',0.85,'OverlapPercent',50,...
 'TimeResolution',0.5,'MinThreshold',-25)
else                                                          (5)
 pspectrum (ysect,fs,'spectrogram','FrequencyLimits',...
 [13 18],'Leakage',0.85,'OverlapPercent',50,...
 'TimeResolution',0.5,'MinThreshold',-35)
end
```

The STFT generates the frequency domain component of the spectrogram. A window function is applied so that the Fourier transform ignores the ends of the time record and discontinuities are removed. This reduces the loss of information in the frequency domain, known as spectral leakage (Smith *et al.*, 1996). A compromise needs to be made between reducing leakage and improving spectral resolution. Quantitatively, the resolution relates to the main lobe width and the amount of leakage relates to the height of the side lobes (MathWorks, 2017b). Leakage can be reduced by attenuating the height of the first side lobe level or increasing the asymptotic roll-off rate of higher side lobes. However, these properties can only be improved at the expense of increasing the main lobe width (Brandt, 2011). Table 5.1 provides a comparison of these properties for the windows considered in this thesis. A small leakage factor is achieved by applying a window with a wide main lobe and high sidelobe suppression.

Table 5.1: Comparison of 1024-point window functions

Window type	Leakage factor (%)	Relative side lobe attenuation (dB)	Main lobe width (-3 dB)
Rectangular	9.15	-13.3	0.00171
Flattop	0.00	-93.6	0.00708
Hanning	0.05	-31.5	0.00269
Kaiser	0.01	-41.7	0.00244

According to the BS ISO 20283-2 (2008) standards, either a flattop or Hanning window should be used when generating frequency spectra from a vibration time signal. The Hanning window is the most common window, it is defined as a half period of a cosine, with the first value at zero. The first side lobe is approximately -31.5 dB below the maximum main lobe value and the roll-off rate is -18 dB/octave. The main lobe is wider than the rectangular window, this results in a maximum amplitude error of -15%. Therefore, the flattop window may be used when a smaller amplitude error is required, for example, for calibration purposes. However, there is a trade-off between frequency and amplitude accuracy. The flattop window has a wider main lobe, which results in a larger uncertainty of the exact frequency of the tone. It should only be applied to signals for which it is known that there are no closely spaced tones within the spectrum. Consequently, the Hanning window provides a good compromise between amplitude accuracy and frequency resolution (Brandt, 2011).

Moreover, due to its wide main lobe, the flattop window should never be used for random signals. The main lobe smooths the spectral density. For sharp peaks in the spectrum, for example resonance peaks due to vibrations on systems with low damping, there is an undesired broadening of the resonance peaks. The most common time window for random signals is the Hanning window and it is the primary window used for spectral calculations of noise and vibration signals (Brandt, 2011). The `pspectrum` function inherently applies a Kaiser window. The spectral leakage is regulated by specifying a real value between 0 and 1. This controls the Kaiser window sidelobe attenuation relative to the main lobe width. A leakage value of $\kappa = 0.85$ is selected as it approximates a Hanning window. Equivalently, a Kaiser window with a shape factor β value of 5.7 approximates a Hanning window, as demonstrated in Figure 5.10. The two parameters are related by Equation (33). The shape factor determines the fraction of the signal energy captured by the main lobe (MathWorks, 2017b). Moreover, the parameters of the Hanning and Kaiser window implemented for a 1024-point segment are shown in Table 5.1 to be similar.

$$\beta = 40(1 - \kappa) \tag{33}$$

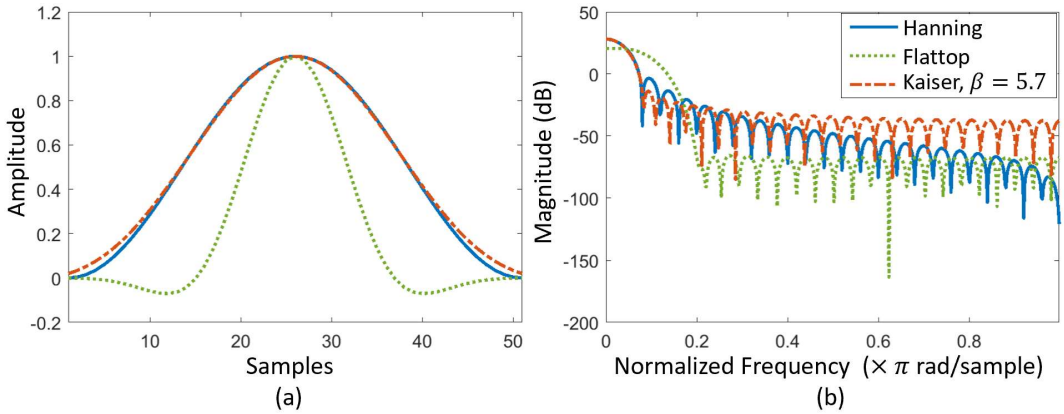

Figure 5.10: 51-point Hanning, Flattop and Kaiser window with β = 5.7 in (a) the time domain and (b) the frequency domain

To compute the time frequency representation, the signal is first divided into segments of equal length, which are short enough so that the frequency content does not change significantly within a segment. The overlap percentage between adjoining segments is set as 50% of the segment length. A Kaiser window is applied to each segment and the STFT is computed. The time resolution is specified as 0.5 seconds, which is equivalent to 1024 samples. The number of samples controls the length of the segments which are used to compute the STFT. If the last segment extends beyond the signal endpoint, the signal is zero-padded. The segment spectra are then used to construct the spectrogram image, where the power of each spectrum is displayed in decibels for each segment using a colour bar (MathWorks, 2017b).

The DC signals generally exhibit a higher power level. Therefore, it was necessary to generate the signal power spectrum differently for the DC and the ICP sensors. The `'MinThreshold'` argument sets elements of the power spectral representation, which are below the threshold, to zero. This increases the intensity contrast and allows lines with a higher power rating to become more visible. It also prevents lower power signal content from being presented and detected as lines for both calm water instances and cases where slamming is prevalent. The threshold was adjusted to -25 dB for DC sensors and -35 dB for ICP sensors, based on the average signal power determined using the `bandpower` function. The DC sensors therefore need to be specified by the user.

Lines are detected in the spectrogram image as discussed in Section 5.6. The detected lines are scaled to the original signal. The time extracted and the corresponding acceleration amplitude relating to a detected slam event are saved in the results folder. The full code is shown in Appendix B.1.3.

5.6. Line detection

The procedure for slamming detection for both the Morlet wavelet transform and spectrogram method is illustrated in Figure 5.11. Step 1 is discussed in Section 5.2 and is applicable to all three methods. Step 2 shows a time-frequency representation of the signal. The details of generating a scalogram image is discussed in Section 5.4 for the continuous Morlet wavelet transform and Section 5.5 for the spectrogram image. The line detection process can be subdivided into three sections. Therefore, a function was written to implement each aspect as given in Appendices B.1.5. to B.1.7. The first function generates a black and white image, the second implements the Hough transform and the third uses the image coordinates of detected lines to identify slams in the time domain.

The scalogram generated by the cwt and the spectrogram are both images; therefore, it is proposed to use image processing techniques to extract the line features. A digital image can be represented as a $N \times M$ matrix. The elements consist of integers or floating point numbers which correspond to colour pixels of the image (Pitas, 2000). In MATLAB the pixel colour is stored in a three-element row vector that specifies the intensity of the red, green and blue constituents. The intensity is denoted as values between zero and one (MathWorks, n.d.). An edge detection algorithm is useful to determine the boundaries, discontinuities and patterns within an image. These features can be detected due to abrupt changes

in pixel brightness. An edge comprises of pixels, which are a different brightness when compared to neighbouring pixels (Dharampal & Mutneja, 2015).

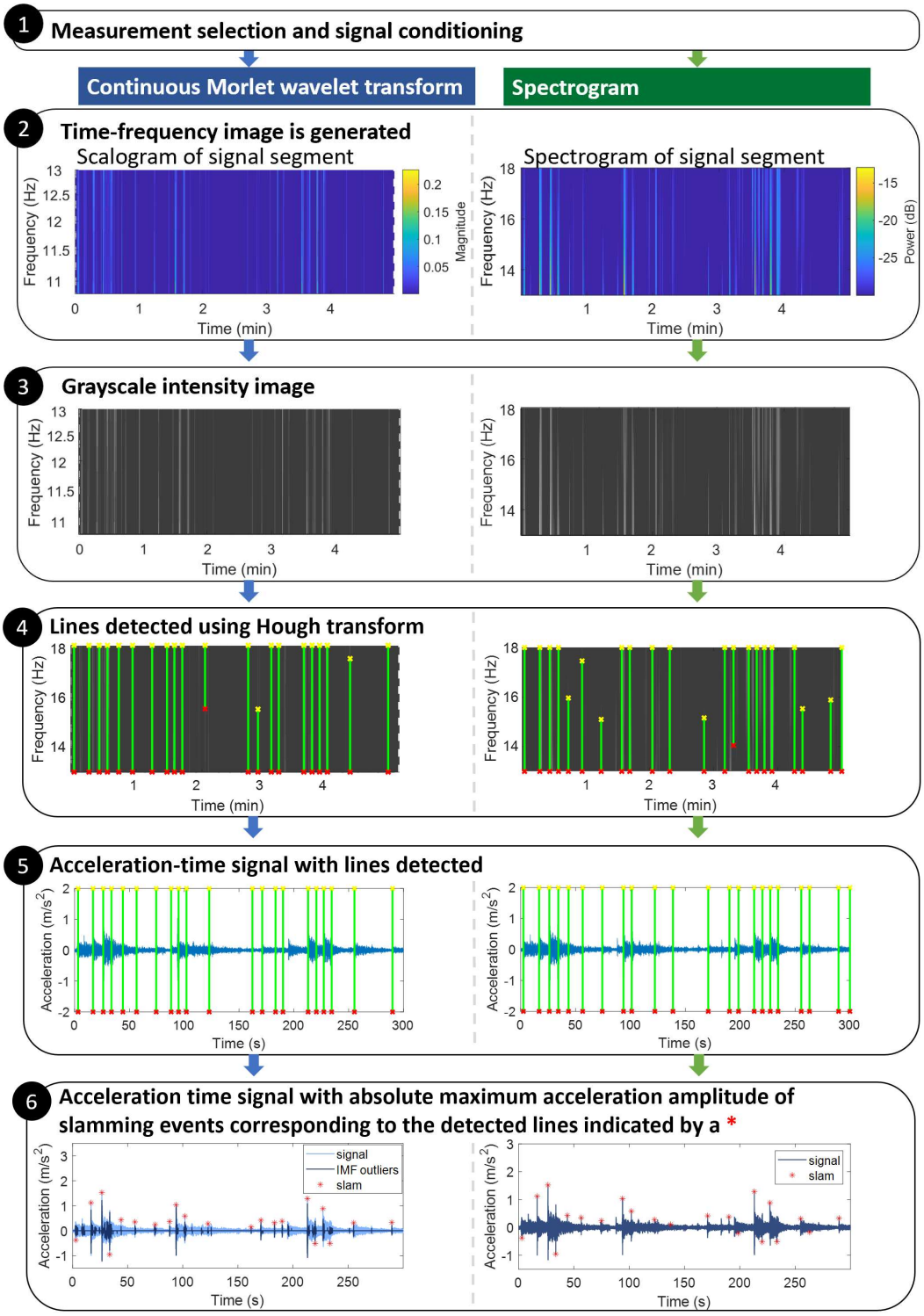

Figure 5.11: Continuous Morlet wavelet transform and spectrogram slamming detection procedure

The image is first captured and converted to a grayscale intensity image before it is converted to a black and white image, using a threshold for the grayscale intensity of the pixels. This presents more distinct lines than the Canny edge detection technique used in an earlier investigation (Bekker, van Zijl & Saunders, 2018). The MATLAB `hough` transform, presented in code extract (6), is then implemented to detect lines. The standard Hough transform uses the parametric depiction of the line, presented in Equation (34), to detect lines (Duda & Hart, 1972). It is computed for a black and white image and the output is shown in Figure 5.12 (b). The original image is represented as an xy-plane, as illustrated in Figure 5.12 (a). The parameter ρ signifies the perpendicular distance from the origin to the line. The angle, denoted as θ, is the angle which the perpendicular line makes with the positive x-axis and it is measured in the clockwise direction (MathWorks, n.d.). Wave slamming produces broadband excitation, whereby a range of frequencies are excited. This materialises on the spectrogram and cwt scalogram as a vertical line at the time of impact. Therefore, the angle θ is limited to the range of -0.01˚ and 0.01˚ when measured from the positive x-axis, so that only vertical lines are detected. The spacing of Hough transform bins along the ρ-axis may be specified as a value between zero and the length of the pixelated image's diagonal. The default value of one is maintained as it is not specified as an argument for the `hough` function (MathWorks, n.d.).

```
[H,Th,Ro] = hough(BW,'Theta',(-0.01:0.01:0.01));
numpeaks = round(tRecord);
P = houghpeaks(H,numpeaks,'Threshold',...
    ceil(0.2*max(H(:))),'Theta',Th);
lines = houghlines(BW,Th,Ro,P,'FillGap',20,'MinLength',40);
```

(6)

$$\rho = x \times \cos(\theta) + y \times \sin(\theta) \tag{34}$$

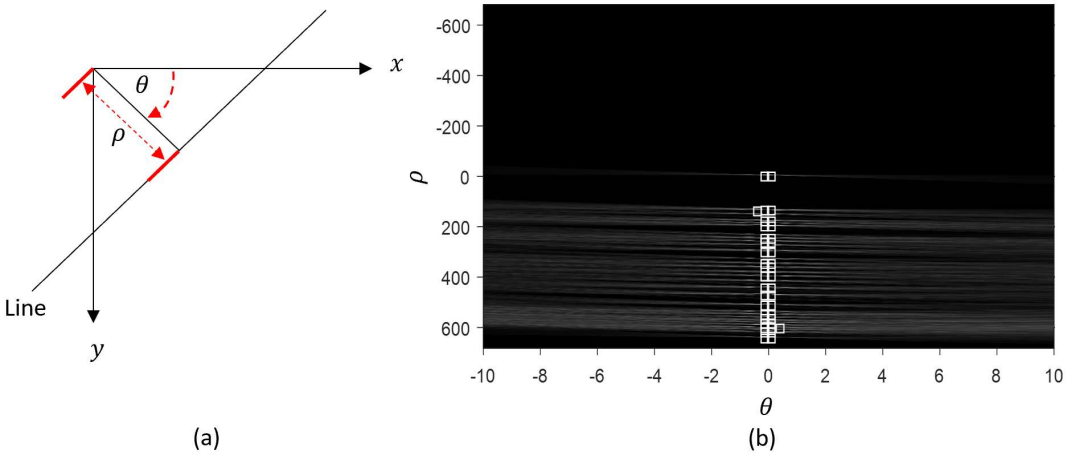

Figure 5.12: (a) The parametric representation of a line, (b) Hough peaks in Hough space for a vertical line

The MATLAB function `houghpeaks` ascertains peak values in the Hough transform matrix. The peak values represent potential lines. To ensure that the maximum number of peaks that may be detected is not restricted, the maximum number of peaks is set to the duration of the signal time record in seconds. The

default intensity threshold is specified as half the maximum value obtained from the Hough transform matrix, `H`. The intensity threshold is set to be lower than the default at `0.2*max(H(:))`. Values which fall below this threshold will not be regarded as peaks.

The `houghlines` function establishes the line segments associated with the peak values in the black and white image. Line segments that are associated with the same Hough transform bin are detected. The `FillGap` argument merges two line segments which are separated by less than the specified minimum distance into a single line fragment. The minimum length that characterises a line segment is also stipulated and merged line segments which are shorter are discarded. A single line may be detected multiple times, therefore, any repeated lines detected are excluded from the lines structure array. The lines which are detected are shown on the greyscale image in Step 4. Not all lines which are visually recognisable by the human eye are detected by the algorithm. The accuracy is improved through the spectrogram power threshold as well as through the IMF and threshold that generate a clearer scalogram image.

The lines, which are detected as pixel coordinates by the Hough transform, are scaled from the image to correspond to the x-axis of the filtered signal in the time domain. The time interval that relates to the pixel width of a detected line is resolved. The absolute maximum acceleration amplitude is extracted from the signal, in the locality of the time interval identified. The result is shown in Step 6 of Figure 5.11. However, since the algorithm seeks out the maximum absolute acceleration value in the vicinity of a detected line, the exact time and magnitude of the extracted slam may not be accurate.

5.7. Earliest slam time

The severity of bow slamming compared to stern slamming is also investigated. The acceleration vibration response due to slamming results in transient oscillations which take time to propagate the length of the structure (Omer & Bekker, 2016). The hypothesis is that an accelerometer located closest to the site of an impact will show a peak in the acceleration amplitude at an earlier time compared to the peak recorded by accelerometers situated further away (Bekker, Van Zijl, *et al.*, 2018). Identifying the sensor closest to the site of impact will establish whether bow or stern slams are more prevalent. Additionally, the peak acceleration amplitude extracted will indicate the magnitude of bow and stern slams encountered.

The process for determining the earliest slam time extracted across all the channels is illustrated in Figure 5.13. The time extracted for a slamming event is first rounded to the nearest second for each channel. If multiple channels detect a single slam event across the same or adjacent second intervals, the time of the slam is first set to the earliest second at which a peak is detected for all of the sensors, as indicated in Step 2. The exact earliest time and corresponding sensor channel are then extracted from the slam event interval identified. The acceleration magnitude corresponding to the earliest slam time is also determined. There are 6 accelerometers associated with both the fore and the aft of the vessel

independently. A slamming event results in a global vibration response and should be detected as a peak by at least two accelerometers (17% of the sensors). This prevents isolated local peaks, due to ship activities or smaller wave interactions, from being detected as slams. Consequently, a single slamming event that is detected across multiple channels is reduced to reflect only one peak acceleration amplitude at the earliest extracted time.

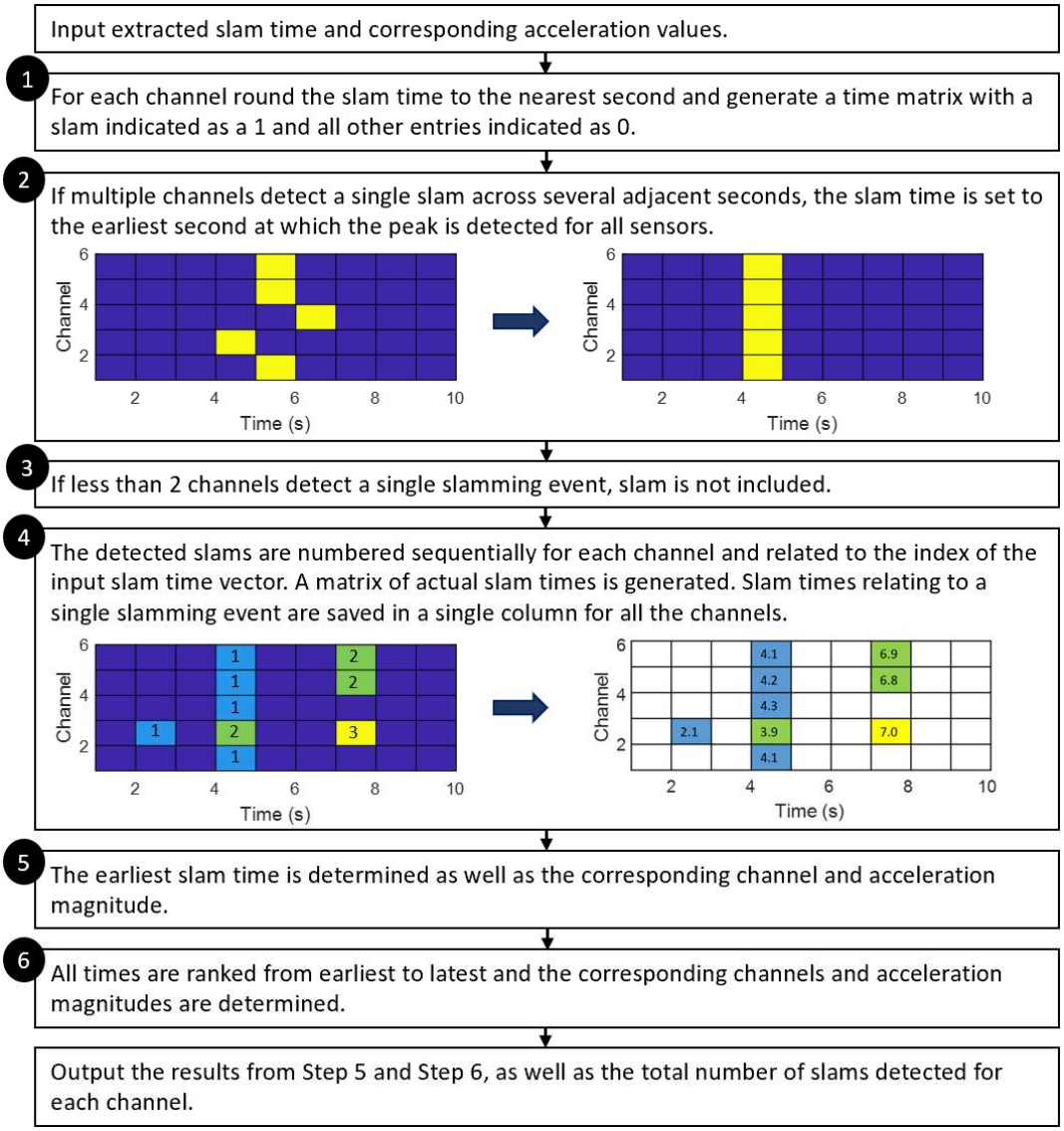

Figure 5.13: Process diagram for earliest slam time function

5.8. Median absolute deviation outlier threshold

It was determined that slams which are extracted by the algorithms developed need to be benchmarked against a threshold to identify the significant slamming events, which should be detected. A statistical outlier analysis of voyage data was previously conducted for voyages that took place in 2016 and 2017. Only data representative of open water navigation was considered. A MAD outlier threshold was determined for these voyages from the maximum acceleration amplitudes

obtained across the voyages for 2 second intervals of data, after applying a Butterworth filter with a cut-off frequency of 0.7 Hz (Saunders, 2018).

The BS ISO 20283-2 (2008) standard states that global vibration measurements should be performed for a frequency range of 1 to 80 Hz. For local structural vibrations a range of 5 to 100 Hz is advised. Therefore, a frequency range from 1 to 100 Hz, which includes both is considered. This frequency range is also comparable to that considered by the Germanisher Loyd limit curves (Asmussen *et al.*, 2001). Moreover, it removes low frequency rigid body motion, while nevertheless including the first vertical bending mode around 2 Hz (Van Zijl & Bekker, 2018). Therefore, the signal was high pass filtered above 1 Hz using a Butterworth filter and low pass filtered below 100 Hz. The signal was resampled with a sample frequency of 1000 Hz, with an oversampling factor of 10. This ensures an accurate time domain representation of the resampled signal, while reducing the sampling frequency of 2048 Hz and thus the processing time.

The absolute maximum acceleration value was obtained from two second intervals from the acceleration data captured during the open water transit of the Winter Cruise and Spring Cruise. This was done according to Equation (35), for the i to j data elements within each two second interval. The highest wave encounter frequency is 0.22 Hz (4.5 s), for the wave states confronted during the manoeuvre case studies. Moreover, human observers situated in the bridge and tasked with recording slamming events noted a minimum time interval of around 2 to 3 seconds between slams. Therefore, a single slam may be captured per two second interval, even with short time periods between successive slams. This ensures that two slamming events are not represented by a single time interval. The first vertical bending mode is around 2 Hz. Therefore a 2 second interval also captures at least four oscillations of this bending mode (Saunders, 2018).

$$peak = \max\left(\left|x_i, x_{i+1}, \dots, x_j\right|\right) \tag{35}$$

The MATLAB `isoutlier` function was used to compute the median absolute deviation (MAD) of the 2 second interval maximum absolute values, to detect the outliers present in the data. An outlier is defined as a value that is further than three scaled median absolute deviations away from the median value (MathWorks, 2017a; Saunders, 2018). The results obtained for the sensors considered are compared in Table 5.2 to the thresholds obtained by Saunders (2018), which were converted from g to mm/s^2. The 2019 Cruise results are shown for both port and starboard sensors separately. The acceleration upper outlier thresholds for the 2019 Cruise data are somewhat similar to those obtained by Saunders (2018). The thresholds are mostly lower for the 2019 data; however, the bow thresholds are higher. These thresholds are dependent on the environmental conditions encountered. A smaller frequency range is considered for the analysis of the 2019 Cruise data, which will also influence the results.

Since BS ISO 20283-2 (2008) recommends that vibration levels are presented in terms of the peak vibration velocity values, the MAD outlier threshold is also presented for velocity values in the frequency range of 1 to 100 Hz. The signal is integrated from acceleration to velocity in mm/s using the `timeint` function of the

ABRAVIBE toolbox (Brandt, 2013). A high-performance eighth-order IIR filter integrator is implemented (Pintelon & Schoukens, 1990). The integration constant, or low-frequency signal variations may influence numerical integration results, therefore the `timeint` function high-pass filters the signal above 1 Hz prior to integration. The linear phase FIR high-pass filter also improves the stability of the IIR filter. For good performance, the signal should be oversampled by a factor of 4. With the sampling rate of 2048 Hz, the oversampling rate meets this requirement with a factor of 20. The filter introduces a time delay of exactly 23 samples (an insignificant 0.0112 seconds). Therefore, the first 23 samples are removed so that the integrated data is shifted to be synchronous with the acceleration time signal (Brandt, 2011). The signal is then appended with 23 zero samples so that the signal length is conserved.

Table 5.2: The MAD thresholds for the 2019 Winter Cruise, for both port (P) and starboard (S) sensors, are compared to the threshold obtained for the 2016/2017 Antarctic relief voyage and 2017 Winter Cruise

	Winter and Spring Cruise 2019				(Saunders, 2018)
	Velocity (mm/s)		Acceleration (mm/s^2)		Acceleration (mm/s^2)
Location	P	S	P	S	
Bow	31.71	31.22	553	539	415
Cargo hold fwd	8.38	8.06	159	138	204
Cargo hold aft	8.83	8.74	162	150	474
Bridge	21.16	9.10	274	171	-
Engine store	5.57	5.70	202	186	484
Stern thruster	9.98	10.13	221	225	422
Steering gear DC	25.70	25.04	607	573	812
Steering gear ICP	-	6.34	-	269	-

The histograms of the maximum absolute velocity and acceleration values extracted for the bow and stern of the vessel are plotted in Figure 5.14. The outliers are also indicated for the combined port side and starboard side sensors. It can be seen that there are a large number of high amplitude outliers in the 2019 Winter Cruise and Spring Cruise data for open water navigation. Table 5.2 and Figure 5.14 indicate the highest velocity outlier thresholds at the bow around 31.5 mm/s, whereas the acceleration outlier thresholds observed at the stern around 591.7 mm/s^2 are slightly higher than those observed at the bow.

Vibration values above the outlier threshold levels are expected to relate to significant slamming events. These sensor thresholds serve as a definition of significant slamming events that is customized for each individual sensor. There is a considerable variance in the acceleration and velocity magnitudes captured by different sensors. This is related to the sensor locations; however, the largest difference is seen between DC and ICP sensors. The DC accelerometers located at the bow and stern capture rigid body motion, whereas the ICP accelerometers are limited to a frequency range greater than 0.7 Hz. The type of sensor therefore also influences the measurement capabilities.

The hypothesis is that the extreme acceleration amplitude values exist as a result of impulsive wave slamming forces. The slamming detection algorithms extract

peak acceleration amplitudes at the time of impact. Velocity is widely used for vibration monitoring as it is proportional to stress, and independent of frequency. The velocity measurement range is also comparatively small since stress values are limited (Gaberson, 2007). Studies have shown that velocity shows a strong correlation with damage over a wide range of frequencies (Gaberson & Chalmers, 1969). Acceleration tends to emphasise higher frequencies, whereas displacement emphasises lower frequencies (Lloyd's Register, 2006). Therefore, extreme velocity amplitudes may indicate structurally significant slams which may contribute to fatigue damage.

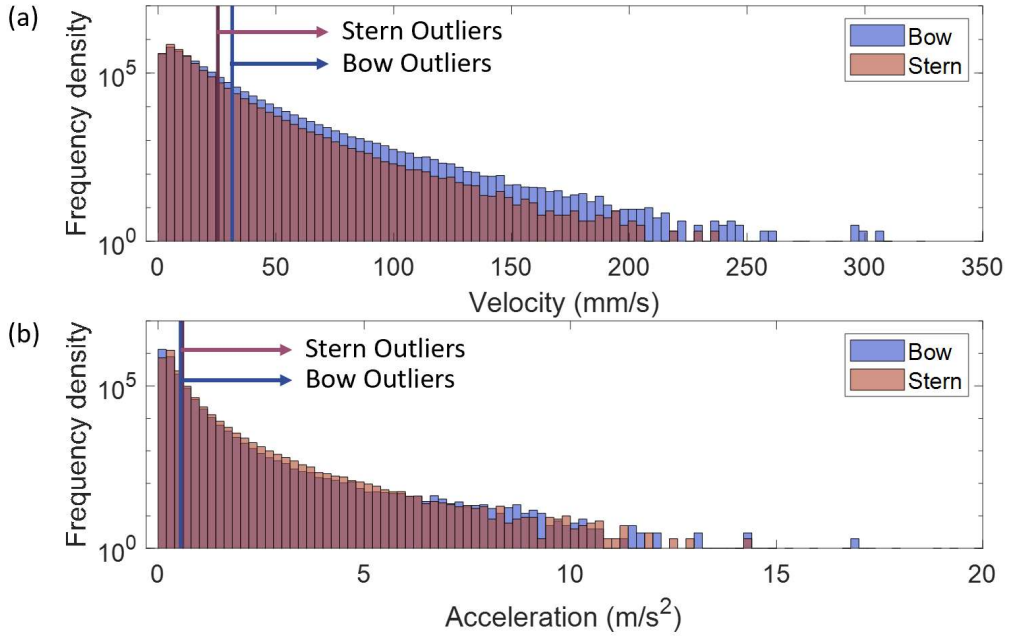

Figure 5.14: Histograms of (a) the absolute peak velocity values and (b) the absolute peak acceleration values extracted across the 2019 Winter Cruise and Spring Cruise at the bow and stern for two second intervals

5.9. Conclusions

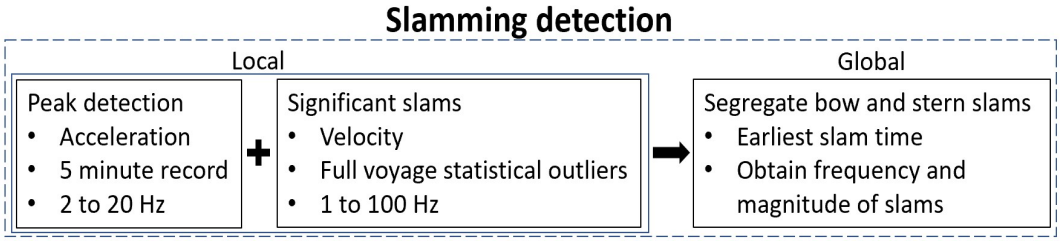

Figure 5.15: Graphical representation of the slamming detection process

The thresholds may consequently assist the identification of significant local slamming events. Nevertheless, to define global slamming events one additionally has to consider the propagation of the vibration along the length of the hull. Therefore, for the slamming detection process shown in Figure 5.15, the peaks in the acceleration signal are first detected using the `findpeaks`, cwt and spectrogram methods. The peaks denoting slams are then related to peaks in the

velocity for the frequency range of 1 to 100 Hz, which are benchmarked against the velocity statistical outlier thresholds presented in Table 5.2, so that only structurally significant local slam events are detected. Finally, the earliest slam time of the extracted slamming events identifies the sensor closest to the site of impact as discussed in Section 5.7. To reflect a single slamming event as only one peak acceleration amplitude at the earliest extracted time.

6. Manoeuvre case studies

6.1. Observed and extracted slams

The human detection of slams should underpin the automated slamming detection analysis to give a sense of the number of slamming events tangibly encountered, which have a magnitude large enough to elicit a global transient whipping response. After applying the different slamming detection techniques to the manoeuvre case studies and comparing the results with the number of observed slams, it was decided that a threshold was required to extract significant slams and reject slams of smaller magnitude. Figure 6.1 shows the average number of slams detected per minute by an observer as well as the total number of earliest time slam events extracted per minute across the length of the vessel by the spectrogram, Morlet wavelet and `findpeaks` methods respectively.

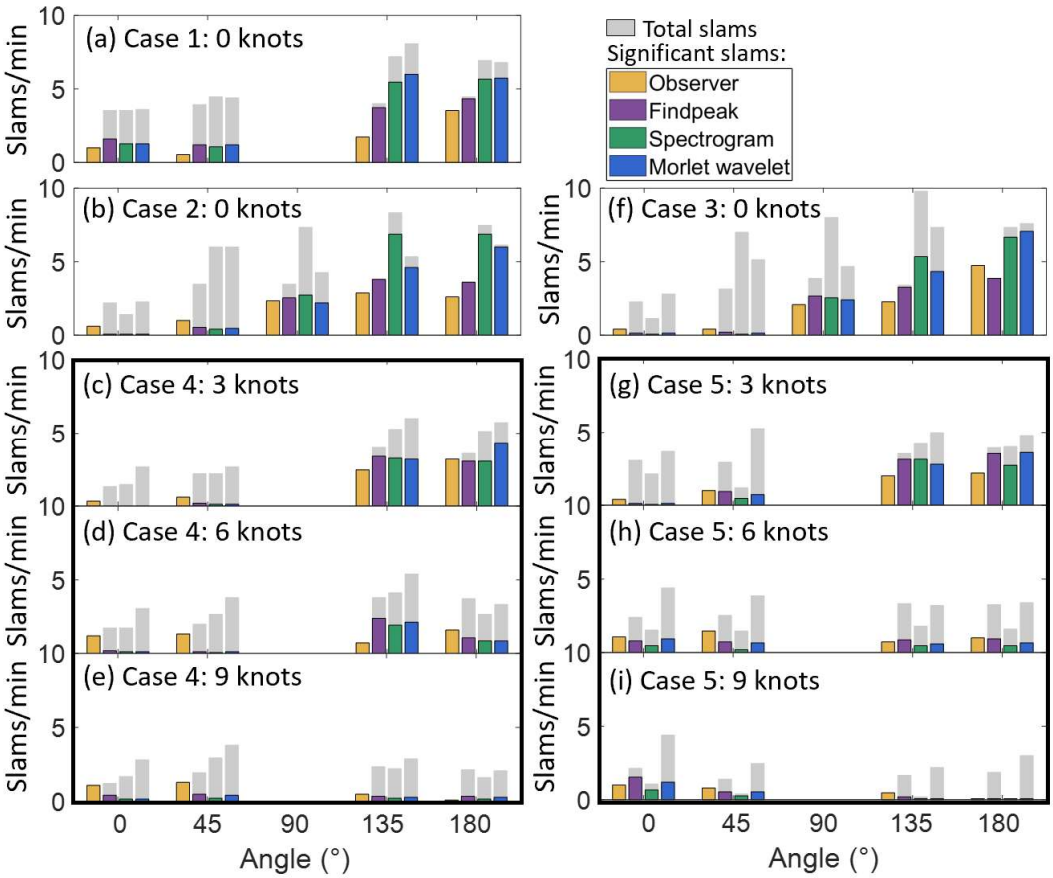

Figure 6.1: The total number of slams detected per minute for the different case studies at each of the relative headings considered as well as the number of significant slams per minute extracted after applying an outlier threshold

It can be seen that the three signal processing methods extract different number of slamming events over the 15-minute periods. All three methods typically extract more slams than the number of slams recorded by the observer, as shown by the total number of slams indicated in grey. This is expected because waves are constantly impacting and exciting the ship, but not all of these impacts are felt by people. Observers reported that slamming could occur as often as 5 times per minute, whereas the spectrogram method extracted up to 9 slams per minute and up to 7 significant slams per minute. The maximum number of slams recorded by the Morlet wavelet and `findpeaks` methods were 8 and 4 slams per minute, with the maximum number of significant slams at 7 and 4 slams per minute, respectively.

The three methods follow a similar trend to the observed slam rating, and the results appear to correlate better after only considering significant slams, which are statistical outliers. It is noted that when approximately 1 slam per minute or less slamming is reported by observers, the methods may underestimate the slamming encountered. Nevertheless, it is considered more appropriate to only extract significant slams that may induce a greater structural whipping response and higher vibration levels, as these slams are believed to be more critical for evaluating the structural integrity of the vessel.

6.2. Frequency and magnitude of slamming associated with the manoeuvre operational conditions

The similarity between the number of significant slams extracted for each of the different methods is further illustrated in Figure 6.2 (a), such that the bar graphs presented in Figure 6.1 (a) to (i) are summarized in sections (A) to (I). Additionally, the average of the extracted peak acceleration amplitudes was determined for each accelerometer channel and the maximum mean value is presented in Figure 6.2 (b). The different signal processing techniques are presented in Figure 6.2 from left to right as the `findpeaks`, spectrogram and Morlet wavelet methods respectively for each ship velocity manoeuvre sequence, as illustrated.

As stated earlier, the methods show similar results for the number of slams encountered for each case. For the stationary manoeuvres, the number of slams extracted do follow the same trend of fewer slams detected with head on waves and more slams detected with following waves and waves approaching the vessel from the aft quarter. For Case 1 the number of slams extracted for a relative heading of 0° is marginally higher than for 45°. This may be due to larger significant wave heights and Beaufort number recorded as well as the higher encounter frequency. For Case 3 the results are also similar for these two relative headings.

By comparing Figure 6.2 (a) and (b), the frequency and magnitude of slams generally show similar trends when comparing the relative headings for each manoeuvre sequence, especially when the vessel is held on station. The magnitude of slams is recorded to be significantly lower for waves approaching at 0° and 45°, whereas the magnitude of slamming is recorded to be higher with waves approaching at 180° and 135°. It is believed that both the magnitude and frequency of slams encountered influence the observer ratings for the number of slams that are felt.

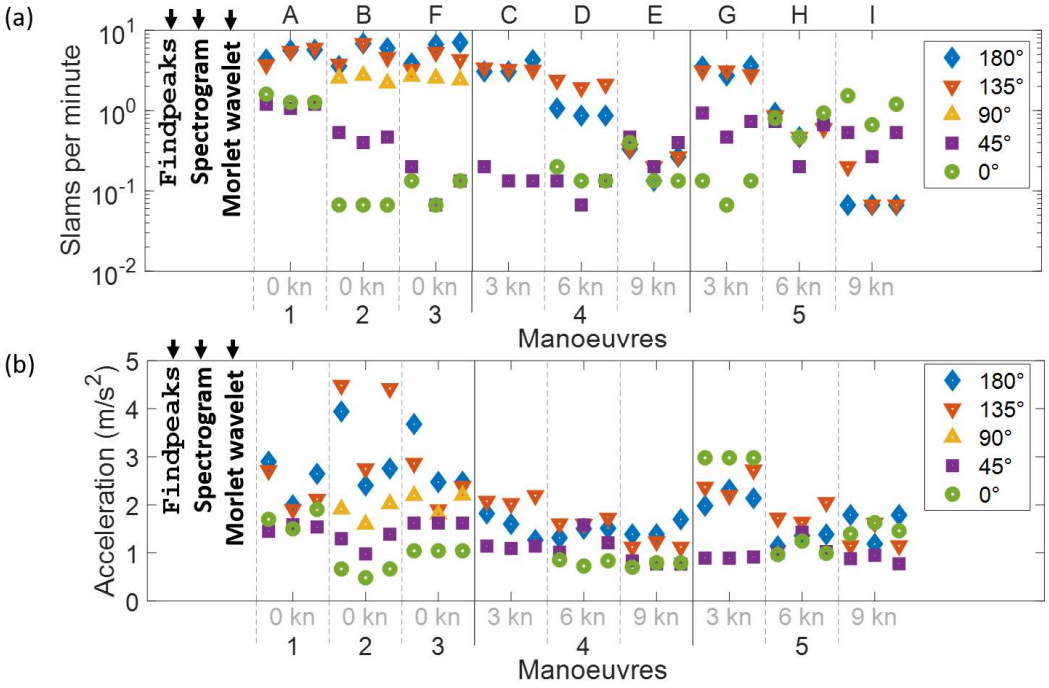

Figure 6.2: (a) Extracted frequency of slamming events and (b) maximum average magnitude of slamming events, for the different slamming detection techniques

For the manoeuvres at speed, the lower speeds indicate a larger number of slams extracted for following and stern-quartering seas, as seen for the stationary vessel. However, as the speed increases, more slamming may be encountered for head and bow-quartering seas, as shown for Case 5 at a vessel speed of 9 knots. The mean magnitude of slamming encounter for following and stern quartering waves is relatively high for all operational conditions when compared to that obtained for other relative headings. Nonetheless, the largest average magnitude of slams is seen for the stationary vessel and slams of comparable, lower magnitudes are extracted for the higher speeds.

6.3. Site of impact

The three signal processing techniques were applied to the case studies to extract the significant peak acceleration amplitudes, which correspond to the time of wave slamming events. The data from the 15 accelerometer channels is processed for each 15-minute period of the manoeuvre sequences. The time of the earliest acceleration peak corresponding to a slamming event was determined across the accelerometer channels to locate the sensor closest to the site of impact. Table 6.1 presents the number of significant slams extracted by the `findpeaks`, spectrogram and Morlet wavelet methods respectively, at the site of impact. Table 6.2 presents the acceleration amplitude extracted from the sensor with the earliest peak in the acceleration-time signal, at the site of impact, for the respective signal processing methods. The port side and starboard side accelerometers are distinguished as left and right of the centreline respectively.

Table 6.1: Number of slams extracted per minute at the site of impact for 15-minute periods

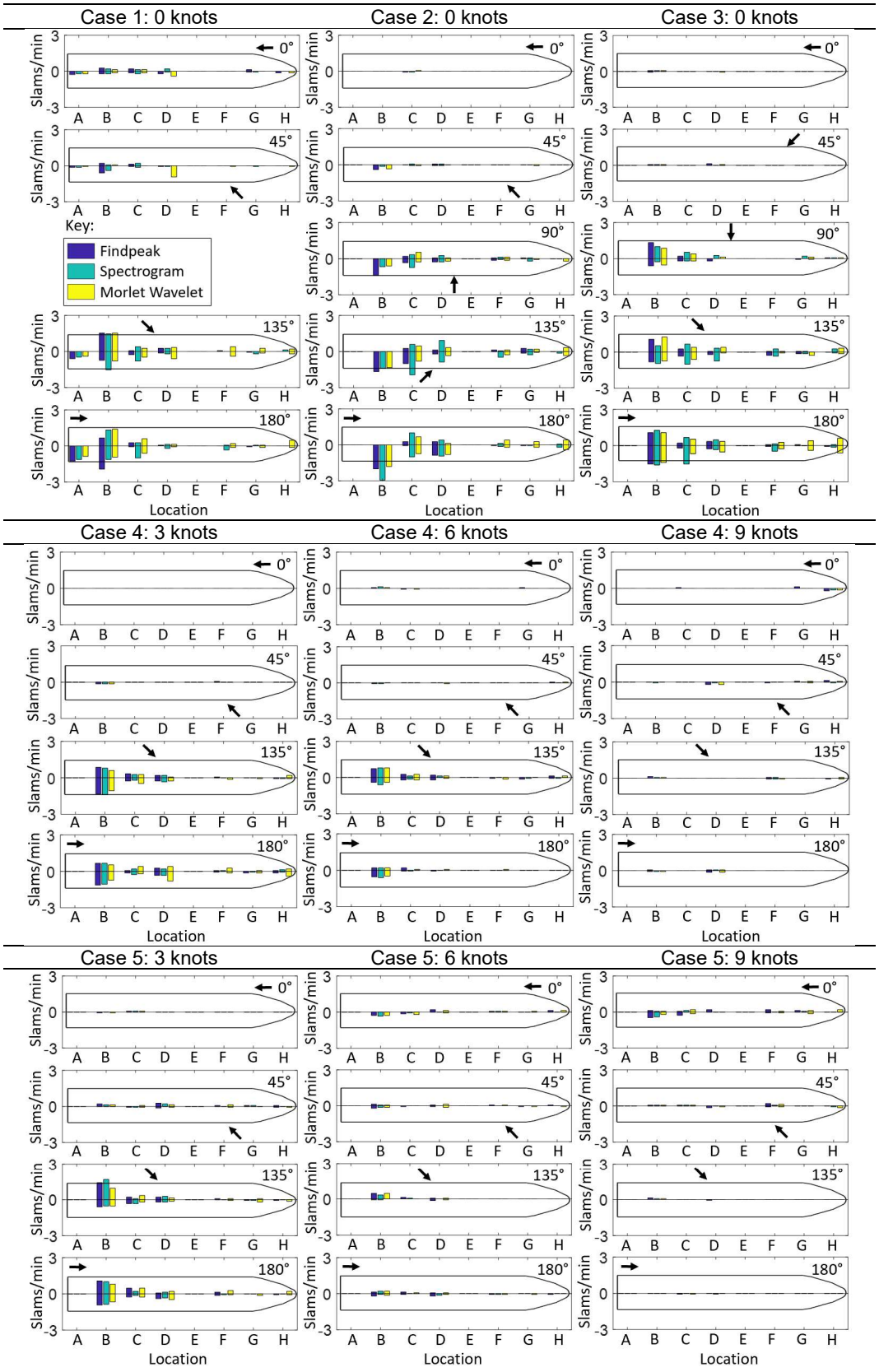

Table 6.2: Absolute peak acceleration amplitude extracted at the site of impact

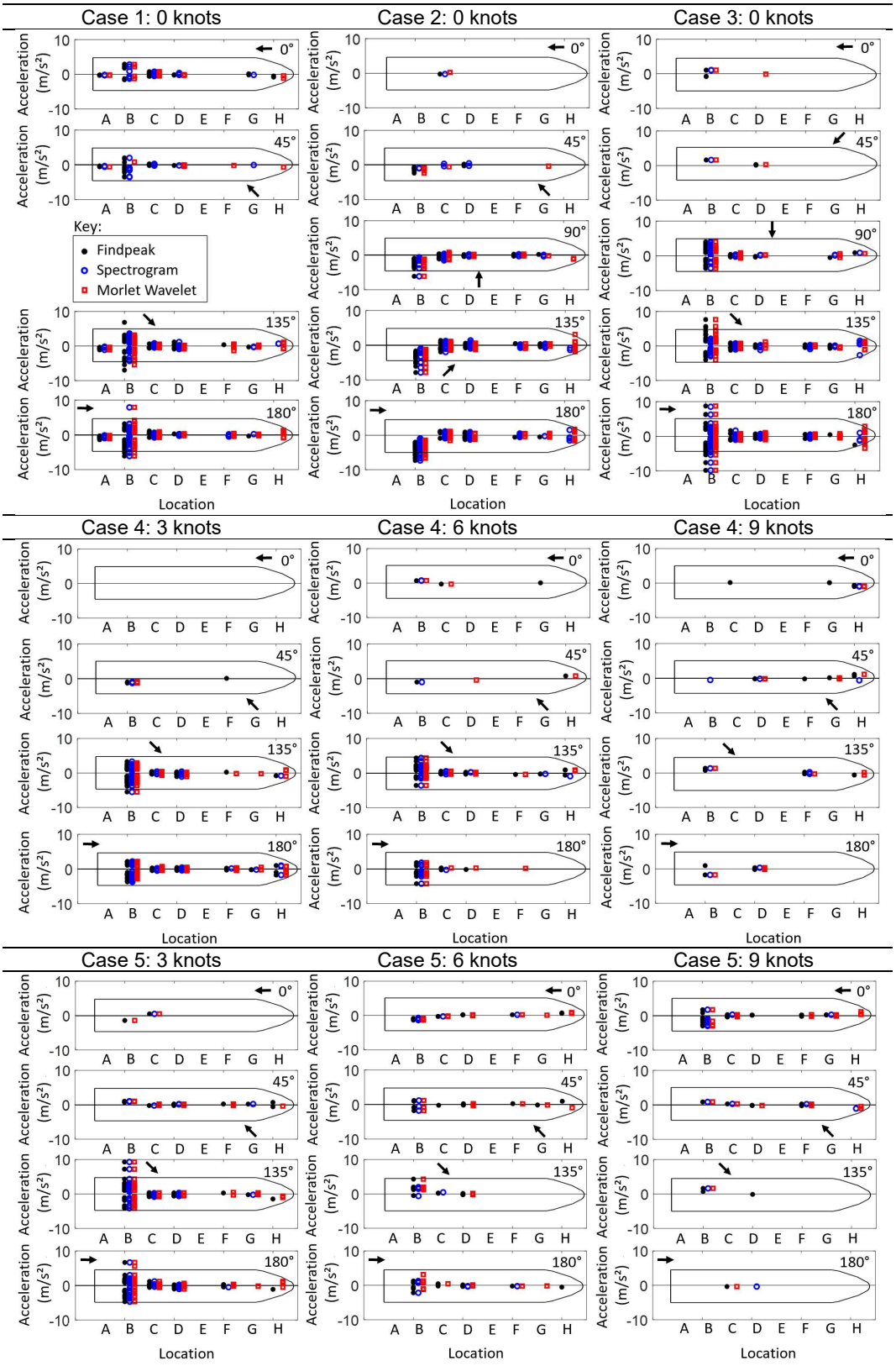

It can be seen in Table 6.1 that the methods give similar results for the site of impact. The methods also show comparable results in Table 6.2, and the range of acceleration magnitudes extracted at the site of impact for the different methods is very similar. With reference to Table 6.1, on average more stern slams are detected than bow slams. The corresponding acceleration amplitude extracted is also much higher at the stern, as shown in Table 6.2. The highest acceleration values occur at location B under the transom, close to the hull transition at the stern. This is where waves rush in under the hull as the hull structure emerges and re-enters the water. This corroborates the fact that the SAA II is predisposed to stern slamming.

The magnitude and frequency of slamming appears to be highest with following and stern-quartering seas when the vessel is held on station. The slamming magnitude and frequency remains high for low vessel speeds of 3 knots. Significant slamming is also seen for Case 4 with the vessel cruising at 6 knots under these conditions. Therefore, stern slamming is reduced with an increase in vessel speed. An increase in vessel speed may also increase slamming for head and bow quartering seas as seen for Case 5 with a relative heading of 0°. Similarly, Case 4 shows an increase in bow slams with a relative heading of 45°.

With waves approaching the vessel at a relative angle of 45°, 90° and 135°, higher acceleration amplitudes typically appear to be extracted at the stern, on the side of the approaching waves (port or starboard). One exception to this is Case 4, with stern-quartering seas and a vessel speed of 3 knots. For Case 2, only the sensors between the bow and the stern thrusters, location H and C respectively, should be considered for this, due to the portside stern accelerometer being switched off during the manoeuvres.

6.4. Conclusions

The results show that the slamming detection methods present similar results. More stern slams are typically detected than bow slams and the corresponding acceleration amplitude extracted is also much higher at the stern. The magnitude and frequency of slamming appears to be highest with following and stern quartering seas when the vessel is held on station. For the manoeuvres at speed with following and stern-quartering seas, the slamming magnitude and frequency remains high at lower vessel speeds, whereas stern slamming is reduced with an increase in vessel speed. Conversely, as the speed increases, more slamming may be encountered for head and bow-quartering seas.

7. Comparison of slamming detection techniques

7.1. Simulation testing slam detection capabilities

Wave slamming data was simulated by extracting an expected wave slamming event, comprising a characteristic impulsive acceleration response, followed by a decaying transient vibration response, as shown in Figure 7.1 (a) and (b). The extracted slam was inserted in an acceleration time signal recorded during calmer ocean conditions, for the same measurement points, where no slams were previously detected. The time interval between slams and the magnitude of the slam was adjusted. The spectrogram, cwt and `findpeaks` techniques are applied to the generated signals and the slamming detection capabilities are compared. The technique fails when embedded slams are not detected accurately. All detected slams are indicated and the MAD outlier threshold of Section 5.8 for resolving significant slams is not applied. Alternatively, an experiment could have been conducted using a suspended beam and an impulse hammer to validate the different methods with a known input (Bossau, 2018). However, it is not guaranteed that the slamming detection capabilities will be the same for both ideal experimental data, with very clear impulsive signals and very little signal noise, and the practical full-scale data.

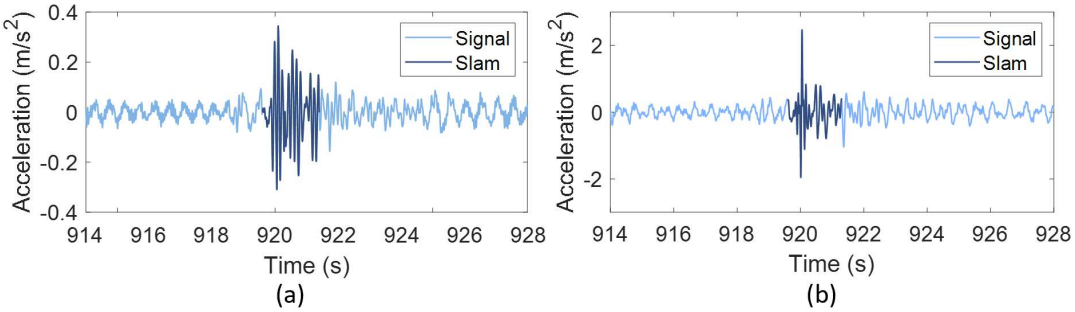

Figure 7.1: Slam event extracted from: (a) an ICP accelerometer time signal measured in the portside stern thruster shaft compartment, (b) a DC accelerometer time signal measured in the portside steering gear room

Firstly, the time interval between slams was maintained at 50 seconds and the magnitude of the impulsive signal was varied. The three techniques were applied to the generated signal and the detected slams are shown in Table 7.1. The slam event with the minimum acceleration amplitude that is correctly extracted is highlighted for each method and the exact acceleration amplitude is stated below. The outlier thresholds used by the `findpeaks` and cwt methods are dependent on the given signal and will therefore vary accordingly. For the calm water signals, signal components above 0.021 m/s^2 and 0.112 m/s^2 are considered statistical outliers for the ICP and DC signals respectively. The outlier thresholds are limiting parameters for detecting slams of varying magnitude and slams below the thresholds will be rejected. The `findpeaks` and cwt method are able to extract slams of similar amplitude for both signals. The lowest magnitude slams extracted for the `findpeaks` and cwt method, namely 0.03 m/s^2 for ICP and 0.25 m/s^2 for DC, are slightly above the outlier threshold for each signal. The lowest amplitude slams extracted by the spectrogram method of 0.09 m/s^2 and 0.37 m/s^2 are only slightly larger.

Table 7.1: Slams of decreasing magnitude extracted by the spectrogram, Morlet wavelet and `findpeaks` methods

ICP	DC
Spectrogram	
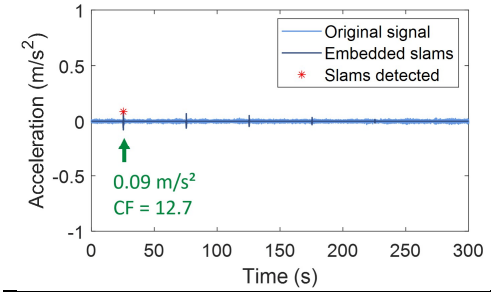	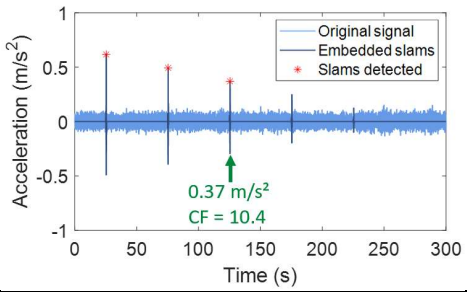
Morlet wavelet	
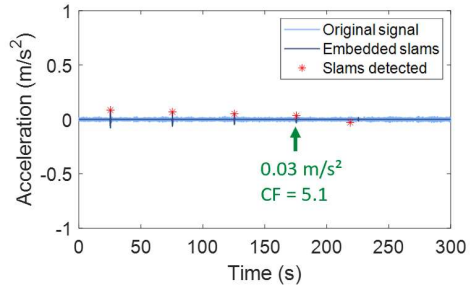	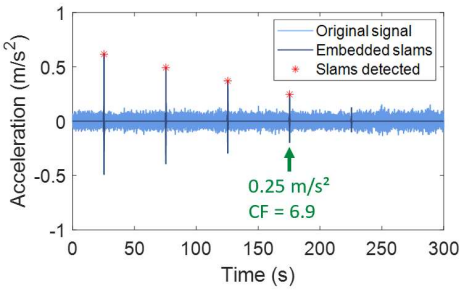
`Findpeaks`	
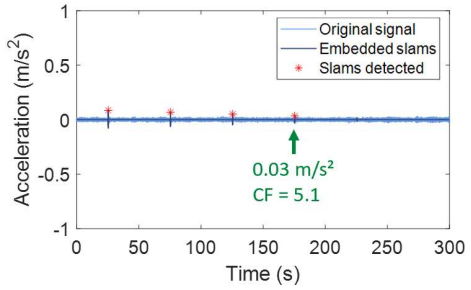	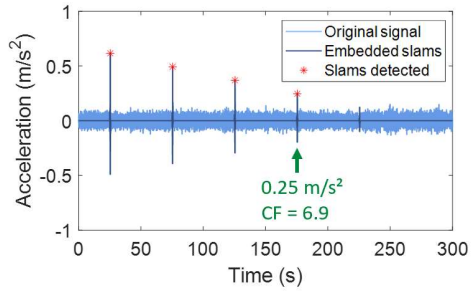

The outlier threshold and the minimum amplitudes extracted are only true for the simulated signal being considered. To allow comparison of the minimum amplitude values extracted from different signals, for example the ICP and DC signals, the crest factor (CF) was calculated and is also shown in Table 7.1. It should be noted that in practice, if the crest factor is greater than 9, the RMS value is considered a less useful measure of the vibration severity (Kowalska-Koczwara & Stypuła, 2018). The crest factor is defined as the ratio of the absolute instantaneous peak acceleration amplitude to the root mean square (RMS) of the signal, as given in Equation (12) (Kowalska-Koczwara & Stypuła, 2018). The calm water signal RMS is therefore utilized as a reference for how large the peak magnitude is. In Table 7.1, the CF values for ICP and DC signals are of a similar magnitude and are much higher for the spectrogram method. The `findpeaks` and cwt methods show identical CF values. The spectrogram method CF values of 12.7 and 10.4 are almost double the 5.1 and 6.9 of the other two methods. Therefore, the `findpeaks` and cwt methods may detect slams with lower magnitudes more accurately than the spectrogram method.

$$CF = \frac{|x_{peak}|}{x_{RMS}} \tag{12}$$

Secondly, the peak amplitude of slam events was maintained above the calm water outlier threshold and the time interval between slams was successively reduced by 0.1 seconds. The three techniques were again applied to the simulated signal and the results are presented in Table 7.2. The time interval at which each method fails to detect successive slams is indicated in the figures by a green arrow and the value is given seconds.

Table 7.2: Slams with decreasing time intervals extracted by the spectrogram, Morlet wavelet and `findpeaks` methods

ICP	DC
Spectrogram	
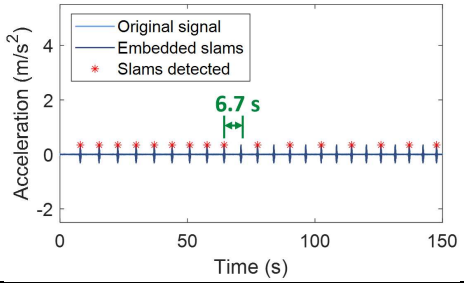	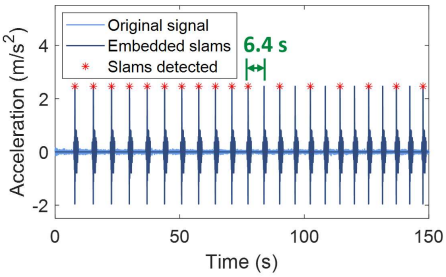
Morlet wavelet	
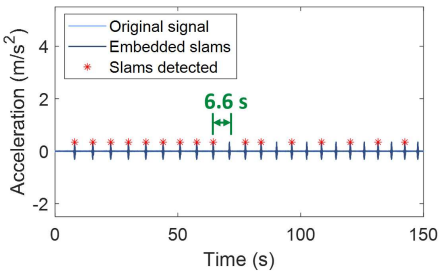	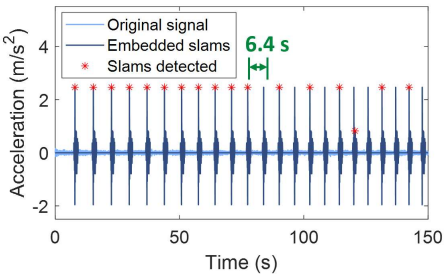
`Findpeaks`	
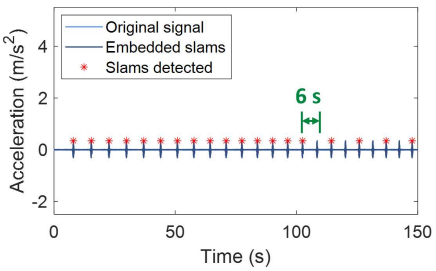	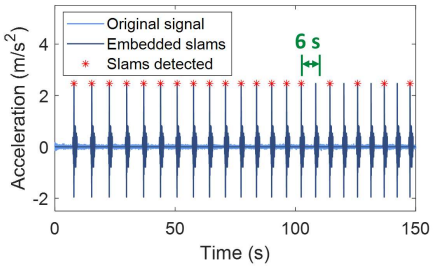

The different methods show similar results. For the spectrogram method all consecutive slams are correctly detected before the 6.7 s interval for the ICP signal and the 6.4 s interval for the DC signal. The Morlet wavelet fails at the 6.6 s interval for the ICP and the 6.4 s interval for the DC signal. These two methods show similar results, as the Hough transform line detection process is governed by the size of the Hough transform bins. Moreover, the search interval relating lines detected as pixels to the time signal is approximately 2.77 seconds for the spectrogram and 1.84 seconds for the scalogram image. The `findpeaks` method

fails for the 6 s intervals, which is in accordance with the time of recurrence specified in Section 5.3, code extract (1). Slams are still extracted after the time interval where the methods first fail, however several slams are not detected. Therefore, all three algorithms have difficulty detecting slams that are less than 7 seconds apart.

The detection of slamming events is therefore dependant on both the magnitude of the slam event relative to the RMS of signal content as well as the time interval between slams. A minority of additional false slams may be detected in the signal which are not true slamming events. This may be due to smaller, less impulsive wave interactions or local peaks in the acceleration levels due to activities on the ship close to the sensor. Additionally, false slams may be detected due to the limitations of the signal processing techniques. For example, for the line detection procedure, the maximum peak extracted corresponding to the detected line may not correspond to the actual slam peak. This is due to limitations in the search interval corresponding to the pixel width and can be seen in Table 7.2 for the DC signal of the cwt method. Additionally, for the `findpeaks` method, any peaks in the signal which satisfy the conditions regarding the time of recurrence, minimum amplitude and peak prominence, may be detected as slams.

7.2. Slamming detection for case studies

To elucidate some of the differences between the slamming detection techniques four 5-minute signal recordings are shown in Figure 7.2, with the slams extracted for each of the techniques. The signals were selected from the stern sensors during Case 3, with the vessel held on station. Both the port and starboard side steering gear room recordings are considered. The signal segments shown in Figure 7.2 (a) and (b) were recorded for the condition of head on waves, whereas (c) and (d) were recorded with following waves. Only three significant slams are detected for the signal record relating to head on waves, as highlighted in Figure 7.2 (a) and (b). In contrast, for the signal record associated with following waves, most slams identified within the given segment are considered significant. It should be noted that the scale of the y-axis of Figure 7.2 (a) and (b) is different from that of (c) and (d) to allow the extracted slams to be seen more clearly.

Peaks *a, c, h, i, j,* and *k* are not detected by the cwt method. The magnitude of the peaks is low and therefore no prominent broadband frequency line is portrayed in the scalogram image at the respective time instances. The associated scalogram and spectrogram images are presented in Appendix A.2. It is expected that the port and starboard side stern sensors will reflect a similar number of slams, this can be seen in that both signals indicate peaks at similar time instances. Points *a, c,* and *i* indicate slams detected by the spectrogram method in only one of the signal segments. This is due to the power threshold, which governs the prominence of broadband frequency lines portrayed by the spectrogram image. Therefore, the corresponding peaks have small magnitudes, which do not manifest as broadband frequency lines in the spectrogram image for the other signal at the respective time instances. Similarly, the `findpeaks` method for peaks *a*, *g* and *i* is limited by the peak prominence. Although, peak *i* is only 5.8 seconds after the preceding slam, which is a limitation for all three peak detection methods.

At point *e* in Figure 7.2 (a), for the starboard side signal, the methods detect a second peak in the whipping response following a slam. For the `findpeaks` method the criteria for peak detection are satisfied as the peak prominence of the whipping response is above the outlier threshold and the supposed slam is located 6.2 seconds after the previous slam. The cwt and spectrogram method also detect a slam 10 seconds after the previous slam. This is more credible as it corresponds to a more prominent peak which can be seen in Figure 7.2 (b), for the port side signal. The broadband frequency line which appears in the spectrogram and scalogram images makes it possible to detect this peak although it appears to be hidden by the whipping response in the time domain. This is an advantage of the methods which employ time-frequency representations of the signal.

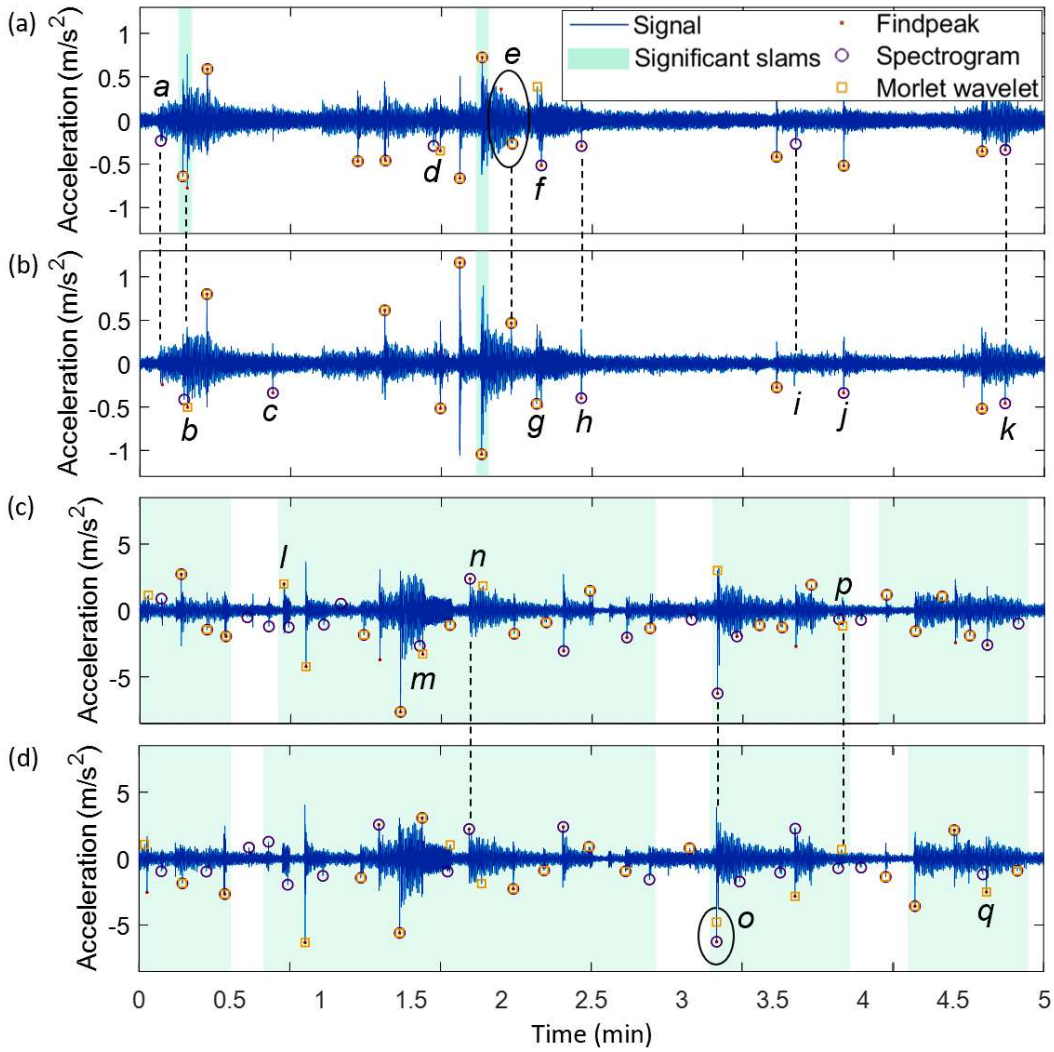

Figure 7.2: Comparison of slamming detection methods for 5-minute acceleration records for (a) the starboard and (b) the port side steering gear room during Case 3 with head on waves as well as (c) the starboard and (d) the port side steering gear room during Case 3 with following waves

Points *b, d, f* and g show peaks in the signal which are very close together, these peaks either relate to two successive slam events or they may relate to a high

whipping response following a single slamming event. The `findpeaks` method classifies the peak with the larger peak prominence as a slamming event. The spectrogram appears to detect the first of the two peaks, unless the magnitude of the second peak is significantly larger with a more prominent broadband frequency line that may be detected. The search interval relating lines detected as pixels to the time signal is 2.77 seconds for the spectrogram. For point *f*, the more prominent peak is 1.3 seconds after the first peak, therefore, both peaks are within the search interval and the absolute maximum peak will be detected as the slam event. For the cwt it seems that the more prominent line and the associated peak is detected as the slam event. A disadvantage of the search interval relating detected lines to signal peaks is that the largest absolute maximum peak associated with a slam event may lie outside of the search interval. Consequently, the extracted acceleration value may be underestimated and the extracted time instance may be offset from the actual time of impact, as seen for peak *o* in Figure 7.2 (d) for the cwt method.

In Figure 7.2 (c) and (d) not many slams are detected by all three methods. The `findpeaks` method detects the least number of slams because it is limited by the outlier threshold associated with the acceleration signal considered, which is used to assess the peak prominence for slamming detection. Even though lower magnitude slams detected by the cwt and spectrogram method are considered significant slams according to the corresponding velocity levels, they are not considered statistical outliers for the 15-minute acceleration-time record related to following waves.

The number of slams extracted by the cwt and spectrogram methods correspond better, although the extracted slam time and acceleration values may be slightly different as observed for points *l, m, n, o, p* and *q*. As discussed previously, this may be due to the search intervals which relate detected lines to peaks in the time domain. Other disparities between these methods may be due to the magnitude or power of the broadband frequency lines displayed by the spectrogram and scalogram images. For the spectrogram method the power threshold determines the prominence of lines portrayed in the spectrogram image. The higher magnitude slams for the case study with following waves results in more lines with a high pixel brightness above the power threshold being displayed in the spectrogram image, compared to the case study with head on waves. This power threshold results in more smaller magnitude peaks that are detected by the spectrogram method, which are not detected by the cwt method.

7.3. Critical discussion of slamming detection techniques

One of the drawbacks of the cwt function is the amount of time taken to generate the scalogram images. Figure 7.3 shows the execution time corresponding to the number of files processed. The signal is analysed according to the 5-minute recording intervals for each of the 14 accelerometer channels. In Figure 7.3 the execution time increases steadily as the number of files analysed increases, for all three slamming detection methods, as indicated by the linear regression lines. The execution time considers only the relevant slamming detection procedure and excludes the measurement selection and signal conditioning execution times, which is presented separately and is applicable to all three methods.

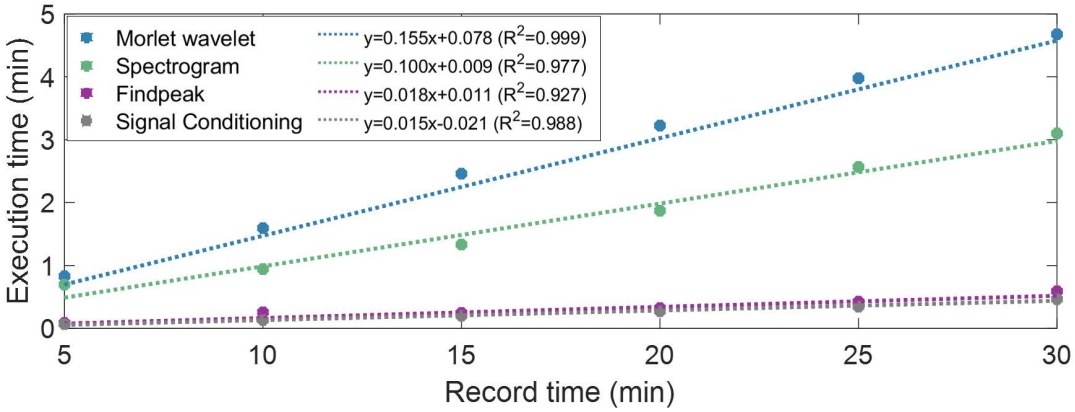

Figure 7.3: Execution time for slamming detection methods and linear regression lines

Despite only looking at higher frequency scales to reduce the execution time, the cwt method takes the longest to complete. Six files with a total recording length of 30 minutes take around 4.7 minutes to process. The spectrogram method is approximately 34% faster at 3.1 minutes for 30 minutes of data. The `findpeaks` method is by far the fastest at around 35.5 seconds, with a similar processing time as the measurement selection and signal conditioning. The `findpeaks` method is consistently an average of 8.83 times faster than the cwt method. The high computational cost of the cwt lies in generating a scalogram image and the EMD also increases the execution time. Similarly, generating a spectrogram image is also computationally expensive, but less so than generating a cwt image.

Full-scale vibration data is sampled at 2048 Hz for voyages with a duration of up to 76 days (Van Zijl & Bekker, 2018). Therefore, the lengthy time histories of data that is recorded must be processed accurately, efficiently and in an automated manner. All three methods are viable for real time processing as the processing time is less than the recording time. However, as voyages consist of several days or weeks of open water transit the `findpeaks` method is the most viable method for post voyage data processing. The `findpeaks` method is nonetheless the most computationally inexpensive method.

All three methods inherently require a threshold to reduce the prospect of detecting false peaks with the caveat that a threshold is required for analysis. The `findpeaks` method uses the MAD to determine statistical outliers and only acceleration values that exceed the lower and upper bounds of the thresholds may be extracted. The minimum peak prominence is also set. For the cwt, the first IMF is considered for high frequency signal components and a clearer scalogram image is produced by setting signal components below a statistical outlier threshold to zero. Similarly, the spectrogram requires the `'MinThreshold'` argument to set elements which are below a threshold to zero, so that lines with a higher power rating become more visible.

These thresholds govern the minimum amplitude which can be detected by each of the methods. Moreover, some form of threshold is required for each of these techniques to make the slamming detection more robust and reduce the number of false peaks detected. A signal may be recorded for calm ocean conditions, with

a low noise floor and small peak values due to smaller local wave impacts. Or a signal may be recorded for conditions with high vibration levels and large peaks due to slamming. In both cases the slam detection algorithms will detect peaks in the signal, which may not necessarily indicate impulsive slamming events, even after applying the thresholds mentioned above. Therefore, it is necessary to incorporate a further 'filtering' technique for all of the methods to evaluate whether the peaks detected correspond to significant slamming events. Significant slams are of greater interest than smaller magnitude local wave impacts, which do not elicit a global response and are less of a concern for human comfort or the fatigue life of the vessel.

The spectrogram method inherently applies a hard threshold, through the `'MinThreshold'` argument, which is not dependent on the given signal, but remains consistent as the vibration levels change. This enables it to distinguish calm ocean conditions from periods with frequent slamming more easily than the `findpeaks` and cwt methods, which determine data driven statistical outliers that are specific to the signal being processed and are dependent on the respective vibration levels. The MAD velocity outlier threshold based on data from two full voyages presents a second hard threshold and is employed to determine significant slams for all of the methods considered. Although, from the signals presented in Figure 7.2, the peak prominence specified by the `findpeaks` method may limit the detection of significant slams for cases where slamming is prevalent as smaller magnitude significant slams are extracted by the other two methods.

Omer and Bekker (2016) showed that whipping responses on the SAA II may last for as long as 40 seconds. The encounter frequency ranges between 0.08 Hz (12.5 s) and 0.22 Hz (4.5 s) for the wave states confronted during the manoeuvre case studies. Moreover, observers noted a minimum time of 2 seconds between successive slam events, but an average of 42 seconds between slams. Therefore, the limitation of slamming detection methods failing to detect slams which are less than 6 seconds apart is considered reasonable as shorter intervals are uncommon. The disadvantage of the 6 second limitation for slamming detection is that long whipping responses with large acceleration magnitudes may be detected as false peaks, which do not correspond to the initial slamming impact as seen for point *e* in Figure 7.2 (a).

Furthermore, it is considered more accurate to employ time-frequency representations of the signal for slamming detection, rather than the `findpeaks` method, which uses peak prominence and a minimum time of recurrence to detect slams. The spectrogram and cwt methods show similar slamming detection capabilities. Provided that the processing time of long-time histories is not the limiting factor, the cwt method is considered a good choice for slamming detection. It employs a data driven threshold that is dependent on the given signal vibration levels, before the MAD velocity threshold is applied to determine significant slamming events. Additionally, literature shows that the mathematical form of the wavelet resembles an impulse response, which fundamentally promotes it as a suitable method for impulsive slamming detection.

8. Structural vibration analysis

8.1. Germanischer Loyd velocity limit curves

Prompted by the need to determine when slamming is excessive due to limitations experienced by the peak detection methods, publications by DNV GL (DNV GL, 2019), the former GL classification society (Asmussen *et al.*, 2001) as well as the International Organization for Standardization (BS ISO 20283-2:2008, 2008) were consulted with the aim of conducting a structural analysis, that is relatable to the assessment of slamming experienced by the SAA II. These sources are critically evaluated in Section 2.6.

DNV GL evaluated the RMS velocity, which is not considered an optimal parameter for the assessment of slamming events. Additionally, it excludes the first two vertical bending modes of the vessel by only considering frequencies above 4 Hz. For this reason, it was is decided that the GL limit curves are more appropriate for investigating possible structural limit exceedances due to wave slamming based on peak amplitude velocity values at discrete frequencies. FFT parameters, such as windows, overlap and block size, are not specified for the application of the GL limit curves for signal analysis. Due to similarities in the structural vibration analysis recommendations in the BS ISO 20283-2 (2008) standard, it was decided that FFT specifications provided by the ISO standard would be used as a guideline for the GL limit curve analysis.

The integral steps of the GL limit curve structural analysis procedure are shown in Figure 8.1. The relevant files containing the signal of interest are loaded, data for the relevant channels is extracted and the units are converted from g to mm/s^2. The signal is detrended to remove the mean from the signal and consequently the DC accelerometer offset is removed. The signal is then integrated from acceleration to velocity mm/s using the `timeint` function of the ABRAVIBE toolbox (Brandt, 2013), which is explained in detail for Section 5.8.

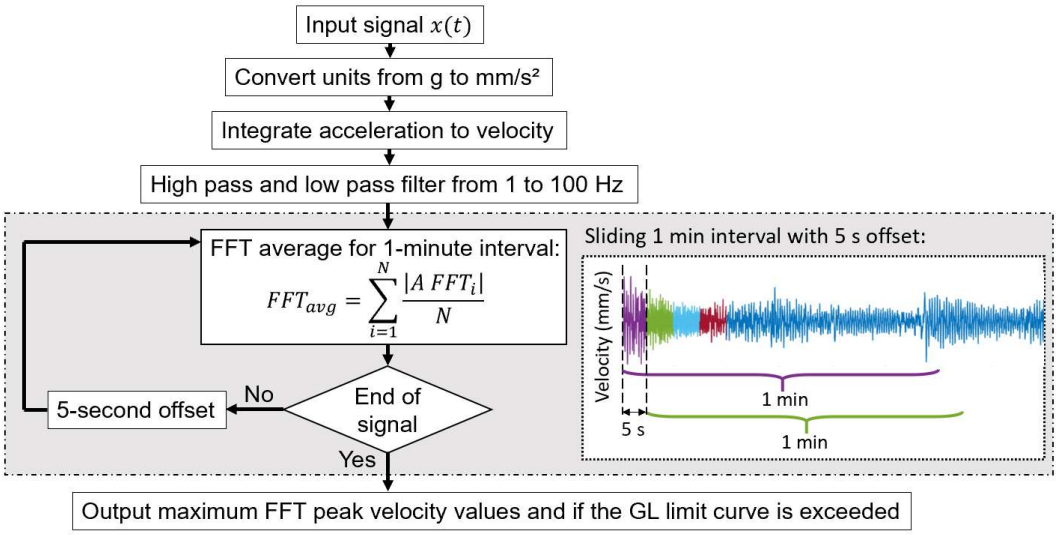

Figure 8.1: Process diagram of FFT structural vibration analysis according to GL limit curves

The frequency range is set to be 1 to 100 Hz so that the GL velocity limit curves may be applied. It is considered sufficient to high-pass filter the signal above 1 Hz to remove low frequency information on rigid body motion. For this reason, a Butterworth high-pass filter is applied with a pass band of 1 Hz. To produce linear phase characteristics the MATLAB `filtfilt` command is used. As a result of the FFT analysis in the frequency domain the MATLAB `resample` command is used as a lowpass filter. The signal is resampled down to a sampling frequency of 200 Hz, which is twice the bandwidth required. This is equivalent to filtering the original signal using a very sharp lowpass filter with nearly ideal characteristics. The frequency spectra can accurately be calculated from the resulting signal, but some time domain information cannot be extracted directly (Brandt, 2011). Given that the signal is not analysed in the time domain it is not considered necessary to up-sample the signal to achieve a higher oversampling ratio. After filtering, any section of the signal that is not part of analysis time period is removed before the FFT analysis begins.

The time interval for the FFT analysis is set to 1 minute, which meets the minimum requirement specified in BS ISO 20283-2 and is nevertheless larger than the minimum recording time interval of 30 seconds required by DNV GL. Each minute interval is supported by 12000 samples and would contain at most 60 periods of the lowest frequency signal component of 1 Hz. Rather than employing a consecutive interval method a sliding interval method is used. A consecutive interval method may not present an accurate result, since the 1-minute interval used for assessment is not necessarily synchronised with the time interval that will present maximum peak velocity values in the FFT spectrum. A sliding interval is able to more accurately determine the maximum exceedance of the limit curves during the period of interest. An offset of 5 seconds between analysis intervals is considered sufficient to allow for a single slamming event to influence the maximum peak velocity spectrum results, as illustrated in Figure 8.1.

A 2048-point Hanning window is applied with a 50% overlap. Therefore, a total of 10 FFTs are calculated and averaged for each 1-minute interval. A window amplitude correction factor of 2 is applied for the Hanning window (Brandt, 2011). The `alinspec` ABRAVIBE function was used as a guideline, however, the resulting spectrum indicates peak velocity values rather than RMS velocity values. This results in a frequency resolution of 0.0977 Hz, for the sampling frequency of 200 Hz, which is a finer resolution than the ISO standard requires. Additionally, it generates 1024 spectral lines, which exceeds the 400 spectral lines required by DNV GL.

Each FFT is evaluated to determine if the lower limit curve is exceeded. Figure 8.2 presents a summary of the FFT results from each stationary manoeuvre. In Figure 8.2 column (b), each FFT which exceeds the lower limit curve is plotted to present a general trend in the FFT frequency spectrum and the FFT with the largest exceedance of this curve is highlighted. The corresponding PSD is indicated in Figure 8.2 column (a). Of the total number of FFTs generated for Case 1 to Case 3 11.2%, 13.9% and 11.7% of the FFTs exceed the limit curves for each of the respective cases.

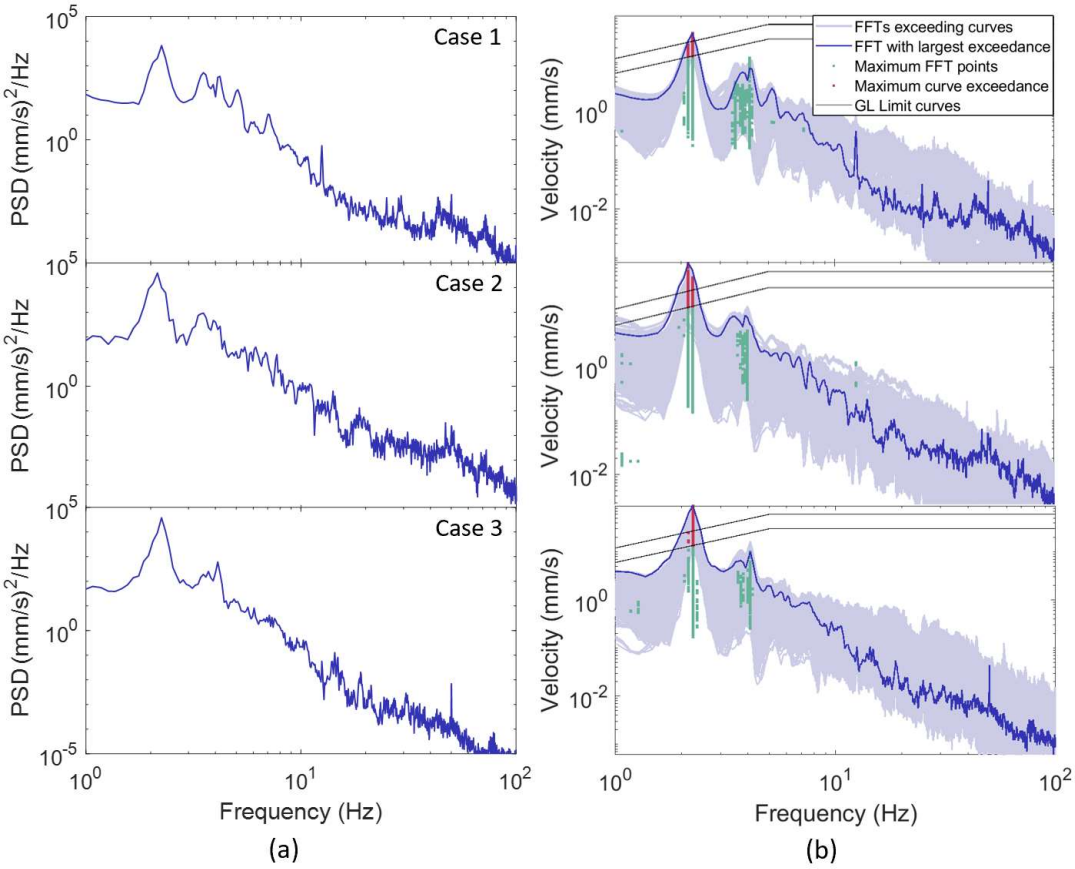

Figure 8.2: (a) PSD corresponding to the FFT with the highest limit curve exceedance (at the bow), (b) a summary of the FFTs generated for each stationary case study (Case 1 to Case 3)

For each FFT that is generated the maximum peak velocity at the corresponding frequency is extracted and plotted as a green dot (●). The maximum peak velocity at the corresponding frequency is indicated with a red dot (●), if it lies above the lower limit curve. This shows that the maximum peak velocity values are indicated around 2 Hz, 3.8 Hz, 4.1 Hz and only a few maximum peaks are indicated at lower frequencies. The FFTs therefore indicate higher peak velocity values corresponding to the first and second vertical bending modes that are excited. Case 1 shows a few maximum FFT points at 5.2 and 7.2 Hz. Case 3 shows additional maximum FFT points at 12.5 Hz, which corresponds to the frequency of the diesel engine. The limit curves are only exceeded around the 2 Hz first vertical bending mode.

8.2. Stationary case studies

Figure 8.3 illustrates the structural vibration exceedance of the GL limit curves during the second case study. All three plots (b) to (d) indicate the maximum peak velocity values extracted from the FFT analysis across the total time period. The points correspond to the centre of the 1-minute time interval analysed. The ship is held on station and the heading relative to the approaching waves is adjusted.

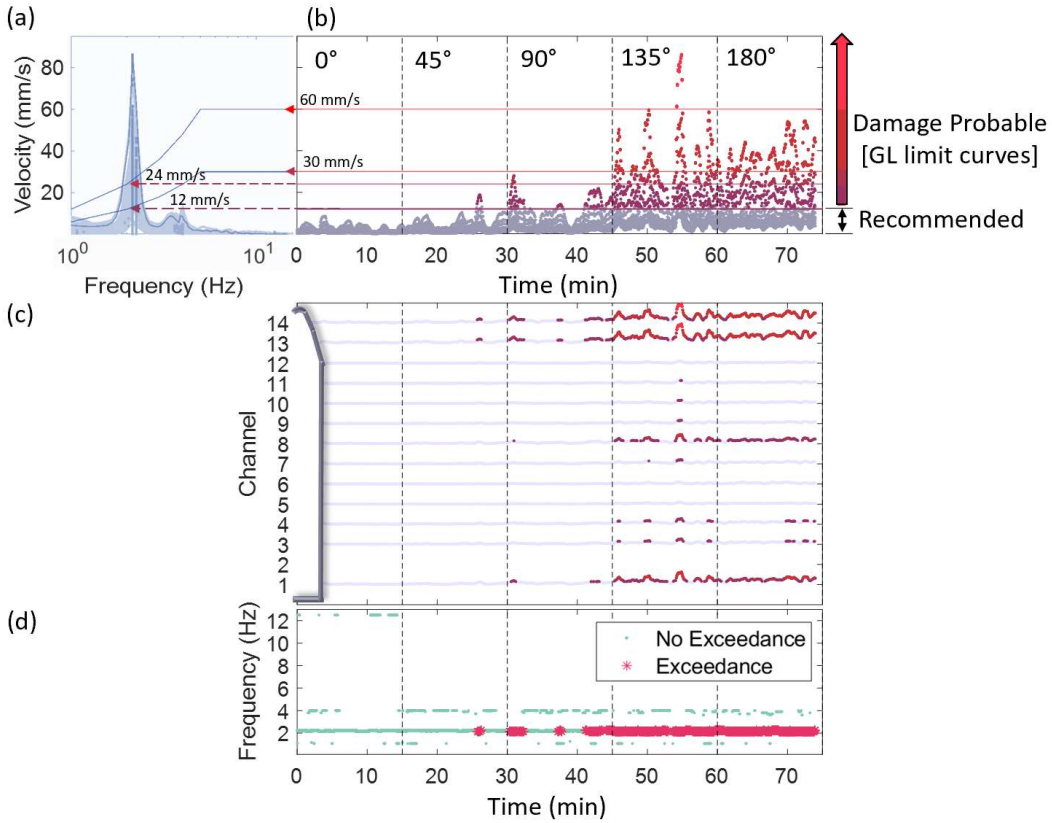

Figure 8.3: Case 2 structural vibration analysis

Figure 8.3 (a) and (b) relates the maximum peak velocity values to the limit curves. It shows that the lower limit curve is exceeded around the 2 Hz vertical bending mode for all of the relative heading angles considered, except for waves approaching head on. Therefore, the vibration is higher than recommended. Then for beam waves and waves approaching from the aft quarter the second limit curve is also exceeded around a frequency of 2 Hz. Exceedance of the second curve indicates that damage is probable. For additional perspective, the limit of 30 mm/s is exceeded for relative angles of 135° and 180°. The highest velocity levels are observed for stern-quartering seas with peak values reaching 86.24 mm/s. This even exceeds the 60 mm/s limit.

Figure 8.3 (c) shows that more structural vibration exceedance is indicated by the DC Accelerometers (Points 1,8,13 and 14). The sensor at Point 2 did not record during this case study. However, there is some exceedance by the ICP sensors in the cargo hold aft and bridge, as well as more structural limit exceedance detected by the stern thrusters at Point 3 and 4. The bow and the stern indicate high peak velocity values for a significant amount of the analysis time period with following waves and waves approaching from the aft quarter. The bow shows higher peak velocity levels than the stern.

Figure 8.3 (d) indicates the frequencies at which the maximum peak velocity values are excited for the period of time considered. The GL limit curves were only exceeded at frequencies around 2 Hz. The maximum peak velocity values indicate

that the 2 Hz bending mode was consistently excited throughout this case study. It also shows that frequencies around 1 Hz and 4 Hz were also prominent, but that the related velocity amplitudes did not exceed the limit curves. For head on waves a frequency of 12.5 Hz was also prominent, but did not elicit a structural exceedance.

Figure 8.4 illustrates similar results for the third case study. Slightly lower velocity values are recorded for waves approaching at 45° and 90°. A higher structural exceedance is experienced for waves approaching at 180° than 135°, although high velocity levels are experienced for both, with 37% and 17% of FFTs exceeding the recommended limit curve respectively during the 15-minute periods. Figure 8.5 shows a significant amount of structural exceedance experienced during the first case study, however it is only indicated for the DC sensors. Additionally, the velocity amplitudes are much lower and remain below 40 mm/s. For these case studies both stern sensors were operational. Again, more structural exceedance is indicated for the bow than the stern and the 2 Hz vertical bending mode is consistently shown to be dominant.

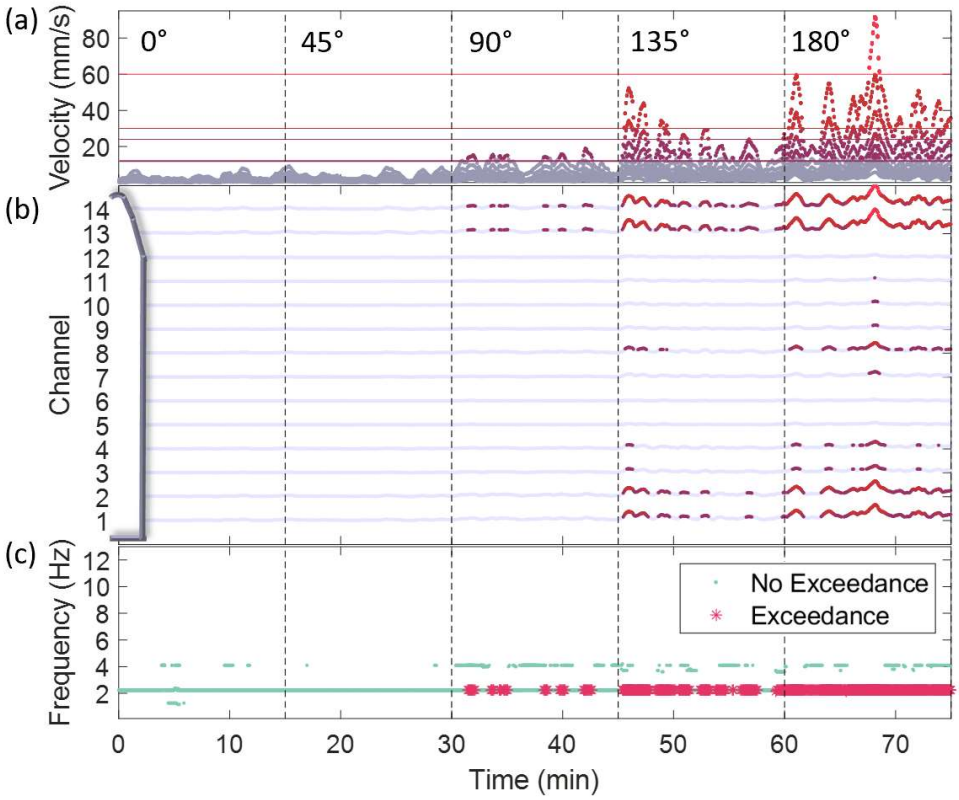

Figure 8.4: Case 3 structural vibration analysis

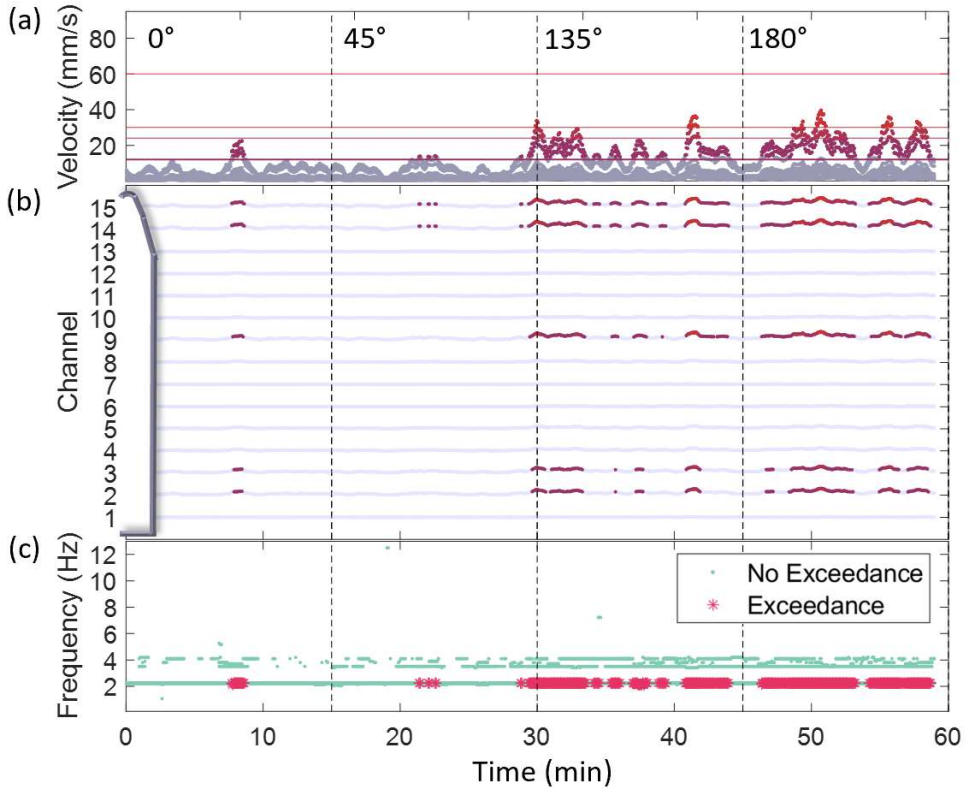

Figure 8.5: Case 1 structural vibration analysis

8.3. Change in speed case studies

Figure 8.6 and Figure 8.7 illustrate the same structural vibration analysis performed for Case 4 and 5 respectively, when both the speed of the vessel and the relative angle of the waves is controlled. These factors are maintained for 15 minutes at each operational condition considered. The figure is presented as a matrix where the rows indicate a constant forward speed of 3, 6 and 9 knots respectively. The columns indicate a constant relative heading at each respective speed.

For head on waves, as the speed increases, more structural exceedance is exhibited. The vibration structural exceedance is observed to be consistently higher at the bow for all cases, although exceedance at the stern is also observed. The vessel outlines on the right of the figure plots are given to illustrate the locations where vibration levels exceed the GL limit curves. Once again it is the 2 Hz vertical bending mode that dominates and it is consistently excited throughout the case study. All of the structural exceedances indicated above occur around 2 Hz.

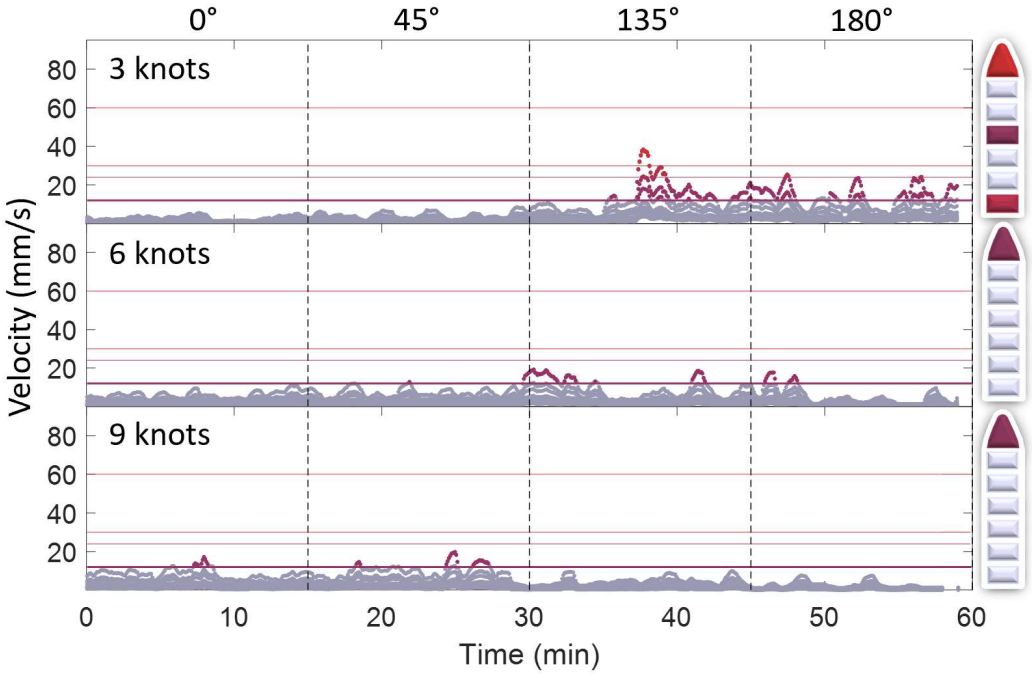

Figure 8.6: Case 4 structural vibration analysis, where 2.5% of all FFTs exceed GL limit curves

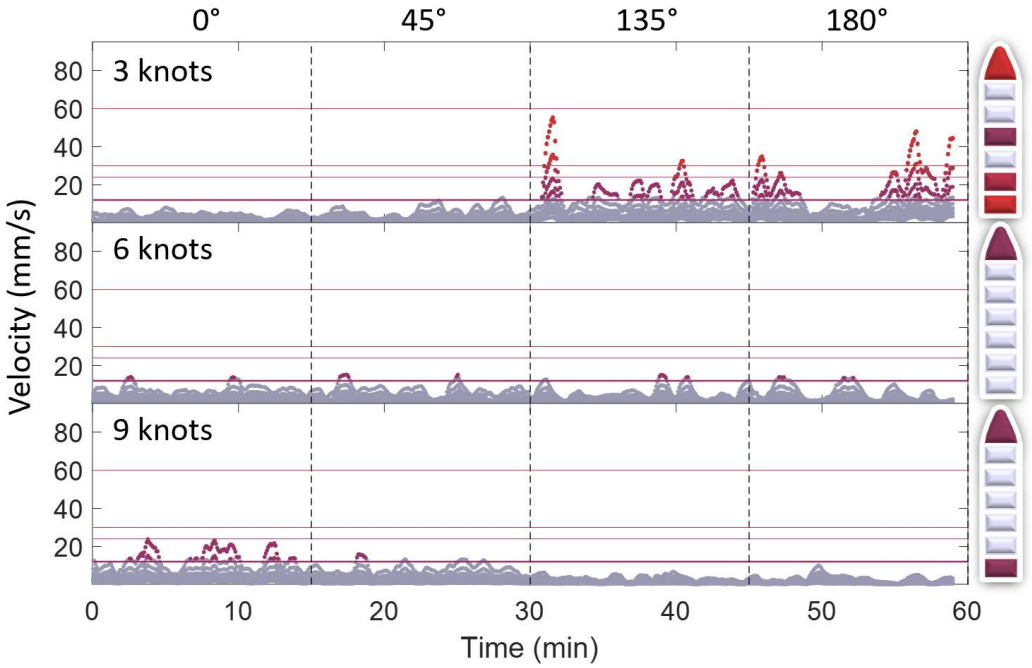

Figure 8.7: Case 5 structural vibration analysis, where 3.3% of all FFTs exceed GL limit curves

It is shown that when the vessel speed is maintained at 3 knots for following waves and waves approaching at the aft quarter, the maximum peak velocity values show significant exceedance of the limit curves. The structural exceedance observed then decreases for higher speeds. At higher vessel speeds, the relative velocity at which waves pass the ship is reduced. Lower speeds (≤ 5 knots) are known to be

more critical for stern slamming than high speeds, for all sea states (American Bureau of Shipping, 2011). It is also shown that the least structural exceedance occurs with waves approaching the shoulder of the vessel at 45° for Case 5 and with head on waves for Case 4. Nevertheless, at 9 knots, better results are shown for waves approaching at 135° and 180°. For Case 5, a similar amount of structural exceedance is indicated for all relative angles when the vessel speed is maintained at 6 knots.

8.4. Conclusion and recommendations

The structural vibration analysis, presented in the previous sections, provides an instantaneous assessment of vibration levels. The vibration levels may indicate whether certain operational conditions, specifically if slamming is encountered, are undesirable for the vessel structure and may be a concern for the fatigue life. However, at this point these methods cannot predict the amount of fatigue damage incurred or the long-term progression of fatigue damage. Therefore, vibration levels should be monitored throughout the service life of the vessel and operational conditions with high velocity levels should be avoided.

Through the structural vibration analysis that was conducted, it is evident that peak velocity levels are significantly higher than recommended for certain operational conditions when slamming is prevalent. Therefore, slamming is a concern for the vessel structure and if the speed and heading is not adjusted to mitigate slamming, and consequently reduce the velocity levels, damage of the vessel is likely. The vertical 2-node vibration mode is most easily excited and produces the largest bending moment amidships (DNV GL, 2015). Since the 2 Hz vertical bending mode is dominant throughout all operational conditions and shows exceedance of the GL limit curves it is likely that damage may be initiated amidships.

With regard to fatigue loading, the total stress history consists of quasi-static wave frequency stresses and high frequency vibration stresses. From this the total fatigue damage can be calculated (DNV GL, 2018). The wave frequency loads are of a lower frequency range than the natural frequency vibration modes, and may be in the frequency range of 0.05 to 0.02 Hz. The wave stress combined with the vibration stress results in a broadband process, for which rainflow counting is the recognised method to determine the fatigue loading history (DNV GL, 2015). Therefore, an analysis which considers frequencies above 1 Hz neglects the effect of wave frequency loading stresses and does not present insight into the total fatigue damage, which includes low frequency components.

Moreover, the high vibration levels indicate that fatigue damage is probable for certain operational conditions, according to the GL limit curves. However, in conditions where the vibration levels are low, the vessel is nevertheless exposed to low frequency wave stresses, in addition to any high frequency stresses that may be present (DNV GL, 2015). The accumulation of fatigue damage is a continuous process throughout the operational lifetime of the vessel and the rate of damage is a function of all encountered sea states and operational conditions (Mao *et al.*, 2010). Therefore, it is recommended that strain measurements should additionally be recorded to more reliably determine the total stress cycles and the total accumulated fatigue damage. Nevertheless, the vibration damage magnitude

has been similar to that of the wave damage, as assessed by DNV GL for all model tests and full-scale measurements (DNV GL, 2018). Consequently, strain measurements may be combined with global ship vibration measurements to gain structural insight for the operation of the vessel and to validate whether high vibration levels do correspond to a high rate of fatigue damage.

9. Operational modal analysis

9.1. Frequency domain decomposition

Stern slamming in particular can excite resonant frequencies in the vessel structure and the 2-node vertical bending mode is most commonly excited (Carlton & Vlašić, 2005). The structural vibration analysis in Section 8 showed that the Germanischer Loyd velocity curves were typically exceeded, with a maximum FFT peak velocity around 2 Hz. In order to examine the modal response of the vessel, Operational Modal Analysis (OMA) techniques are employed. The mode shapes and associated frequencies are obtained through Frequency Domain Decomposition (FDD) (Brincker *et al.*, 2000). The vertical bending mode response magnitudes are then assessed. This provides insight into the contribution of different modes to the whipping response and aids the identification of critical areas at risk of structural damage. It is also desired to compare the vertical bending mode response magnitudes for bow and stern slamming.

The power spectral density (PSD) was calculated for each of the accelerometer channels, for each of the relative headings considered, over the frequency range of 0 to 32 Hz. Figure 9.1 illustrates the average of the PSDs from the DC sensors at the bow and stern for a stationary manoeuvre. The first significant peak at 0.13 Hz, close to the wave encounter frequency of 0.12 Hz, indicates that a significant amount of rigid body motion (RBM) is captured in the signal recording. Two further significant peaks seen around 2.25 Hz and 4.09 Hz, are associated with the first and second vertical bending modes (VBM) (Soal, 2014; Van Zijl, 2020). Therefore, further analysis considers the frequency range below 9 Hz.

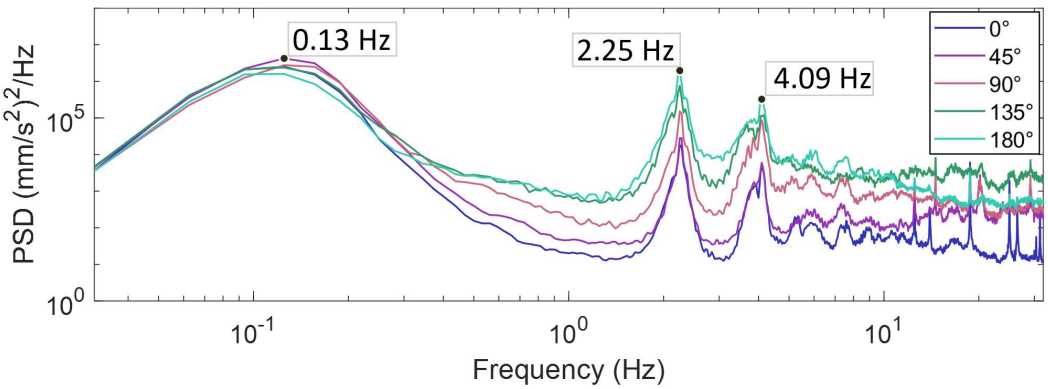

Figure 9.1: PSDs of a stationary manoeuvre, Case 3, with a 2048-point Hanning window, 50% overlap and a frequency resolution of 0.313 Hz.

Caution is necessary when harmonics are present in the signal. A harmonic appears as a narrow peak in the PSD and singular values, which can be confused with modal peaks (Brincker *et al.*, 2007). The shaft often operates at 140 rpm

(2.33 Hz) which may influence the first vertical bending mode (Saunders, 2018). The average shaft speed for the manoeuvres varies between 115 rpm (1.92 Hz) and 58 rpm (0.97 Hz). Therefore, it is unlikely that the shaft speed harmonics will significantly influence the first VBM. However, the Blade Pass Frequency (BPF) ranges from 3.88 to 7.68 Hz, which may influence the second VBM for the manoeuvres at speeds of 3 knots, as shown in Figure 9.2. Therefore, the second VBM may be larger for these cases due to the resonant effect of the BPF contributing to the magnitude of the response. Nevertheless, the modal parameters are consistently identified throughout the manoeuvre sequences, irrespective of the BPF, and the significant peaks in the PSD are not solely attributed to the harmonic peaks, even when the frequencies are similar.

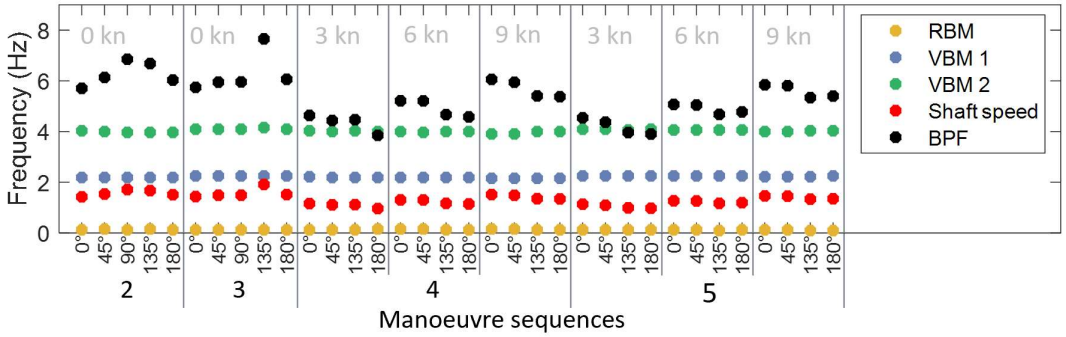

Figure 9.2: Spring Cruise rigid body motion, modal frequencies, shaft speed and BPF

The FDD modal analysis was conducted for each of the open water manoeuvre case studies. The 15 minute measurement duration produces 1800 observations of the 2 Hz vertical bending mode, which is the lowest expected natural frequency (Van Zijl, 2020). The signal was decimated to reduce the sample frequency to 64 Hz. A PSD matrix is calculated with a 2048-point Hanning window and an overlap of 50%. The frequency resolution is 0.0313 Hz. The singular value decomposition (SVD) is computed for each frequency line. The first set of singular values from the CPSD matrix are plotted in Figure 9.3 (a) and (b) for Case 3 and Case 5 respectively, for each of the relative headings. Only the first set of singular values are considered for the analysis.

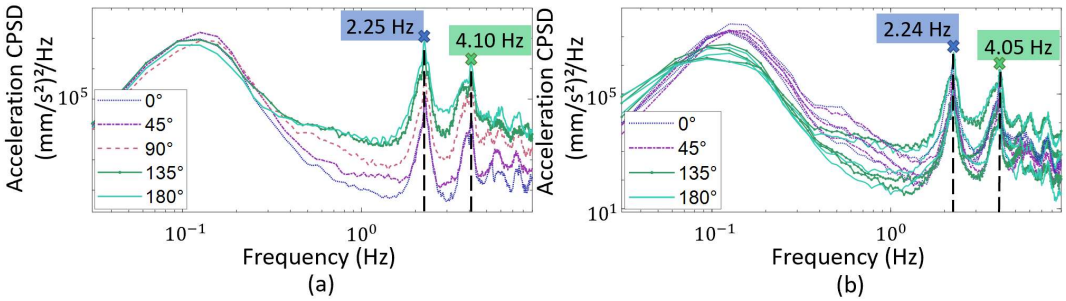

Figure 9.3: First set of singular values of CPSD matrix for (a) a stationary manoeuvre (Case 3), and (b) a manoeuvre at speed (Case 5), for each of the relative headings

Prominent peaks are indicated around 2.25 Hz and 4.10 Hz. These represent the first two VBM of the vessel, for which the mode shapes are shown in Figure 9.4. The frequency of the VBM peaks obtained from the singular values are also plotted

for the manoeuvre sequences in Figure 9.2. Figure 9.4 (a) shows the 2-node vertical bending or hogging mode, for which the OMA has a period of 0.44 s. The second VBM has a period of 0.24 s. Therefore, if each mode is excited for only a minute a total of 135 and 245 oscillatory cycles would be experienced for the first and second VBMs respectively. VBM 2 is approximately twice the frequency of VBM 1.

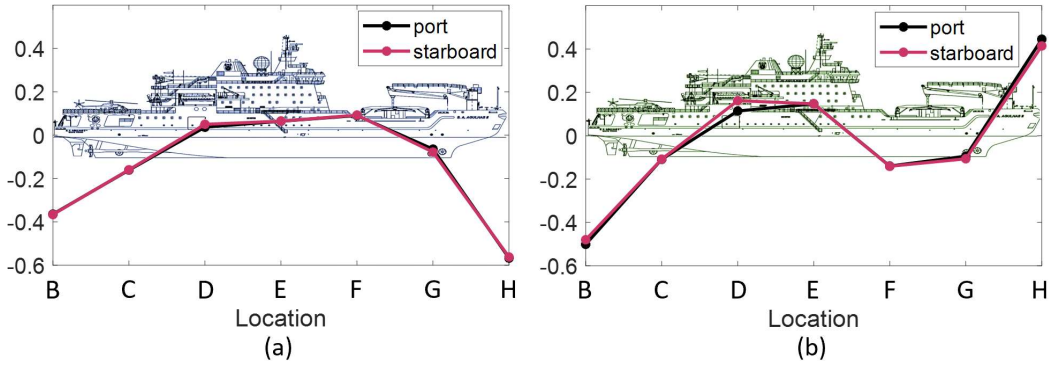

Figure 9.4: Mode shapes of the first two VBM at (a) 2.25 Hz and (b) 4.09 Hz

The modal assurance criterion (MAC) matrix is used to compare the similarity between different mode shapes. The MAC value between two modes, φ_r and φ_s, is defined by Equation (36). Figure 9.3 shows that the same two VBM dominate the structural response throughout all sequences of manoeuvres. This is confirmed by the MAC matrix shown in Figure 9.5 (a). The high MAC values ($MAC \approx 1$), show that the mode shape for each VBM remains consistent between the different operational conditions, across all of the case studies (Brandt, 2011). However, when the first and second VBM are compared, the MAC values are low ($MAC \approx 0$). This confirms that VBM 1 and VBM 2 are two distinct mode shapes. The slight difference in the MAC values obtained for Case 2 is due to the portside steering gear room accelerometer that was inadvertently disconnected from its power supply. Therefore, the portside mode shape point at location B cannot be determined. Even so, the MAC values remain similar.

$$MAC_{rs} = \frac{|{\varphi_r}^H \varphi_s|^2}{({\varphi_r}^H \varphi_r)({\varphi_s}^H \varphi_s)} \tag{36}$$

The process for determining the magnitude of the modal response is presented in Figure 9.5 (b). Figure 9.6 shows the first five singular values of the cross PSD (CPSD) for stationary vessel with head on waves. The first singular value (s1) shows two prominent peaks at 2.25 Hz and 4.09 Hz. Each VBM peak is extracted and the mode shape is determined at the corresponding frequency. The mode shapes associated with frequency points, with a frequency resolution of 0.0313 Hz, on either side of the peak are also determined. The similarity of the adjacent mode shapes and the mode shape relating to the peak is assed using a MAC matrix. Values greater than 0.9 indicate consistent resemblance of the two mode shapes

(Pastor, Binda & Harčarik, 2012). Therefore, an upper and lower frequency bound are extracted for consistent mode shapes that are related to each VBM.

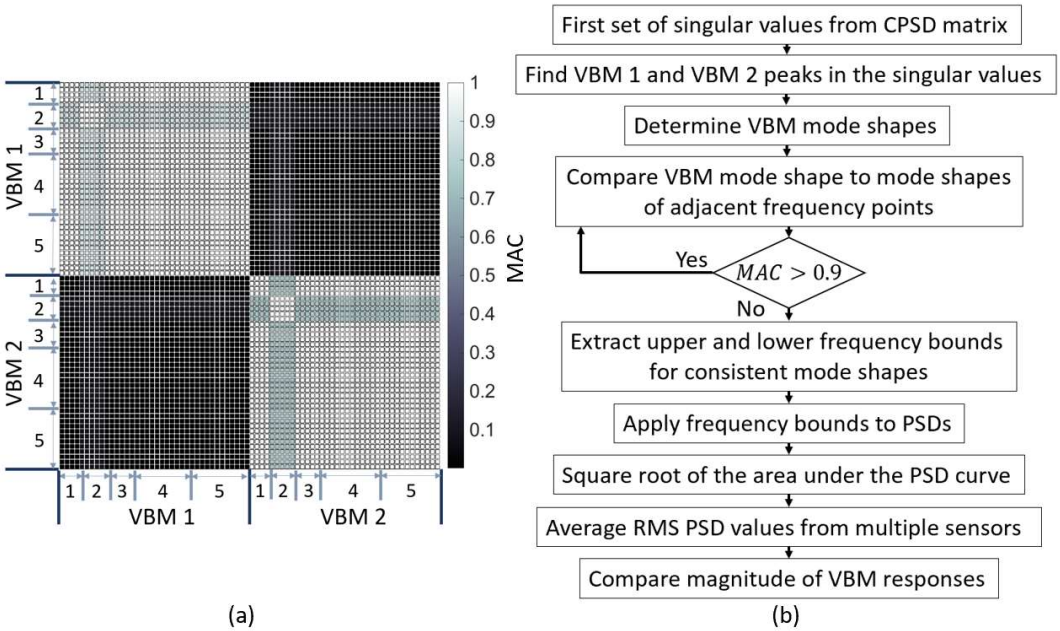

Figure 9.5: (a) MAC matrix corresponding to VBM 1 and VBM 2 for all sequences of manoeuvres, Case (1) to (5), (b) process diagram for determining the magnitude of VBM 1 and VBM 2 responses

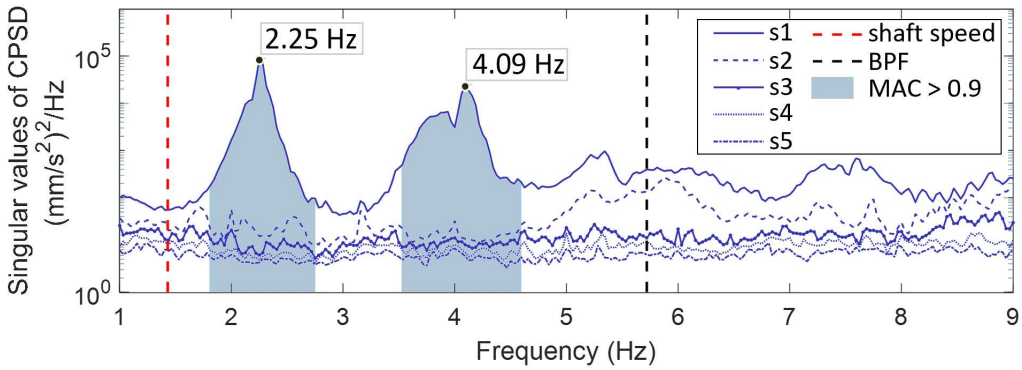

Figure 9.6: First five singular values (s1 to s5) of CPSD matrix for Case 3 with head on waves, a shaft speed of 86 rpm (1.43 Hz) and a blade pass frequency of 5.72 Hz

The lower frequency (f_1) and upper frequency (f_2) bounds are then applied to the PSDs of the bow and stern sensors with the same frequency resolution, as illustrated in Figure 9.7. The square root of the area under the PSD curves, within the frequency range surrounding a modal peak, is obtained using the MATLAB `trapz` function. Thus the RMS PSD values related to the magnitude of each VBM response within the frequency range are determined according to Equation (37), where G_{xx} refers to the single-sided PSD (Brandt, 2011). This is repeated for each manoeuvre sequence. The average of the RMS values generated for the bow and stern sensors is shown for both VBM in Figure 9.8 for all of the manoeuvres.

$$x_{RMS} = \sqrt{\int_{f_1}^{f_2} G_{xx}(f)df} \tag{37}$$

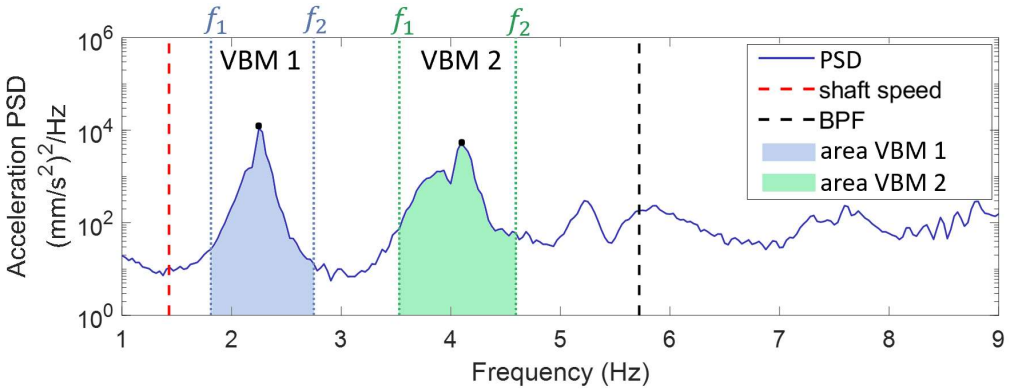

Figure 9.7: PSD of the starboard steering gear room sensor for Case 3 with head on waves, a shaft speed of 86 rpm (1.43 Hz) and a blade pass frequency of 5.72 Hz

9.2. Results and conclusions

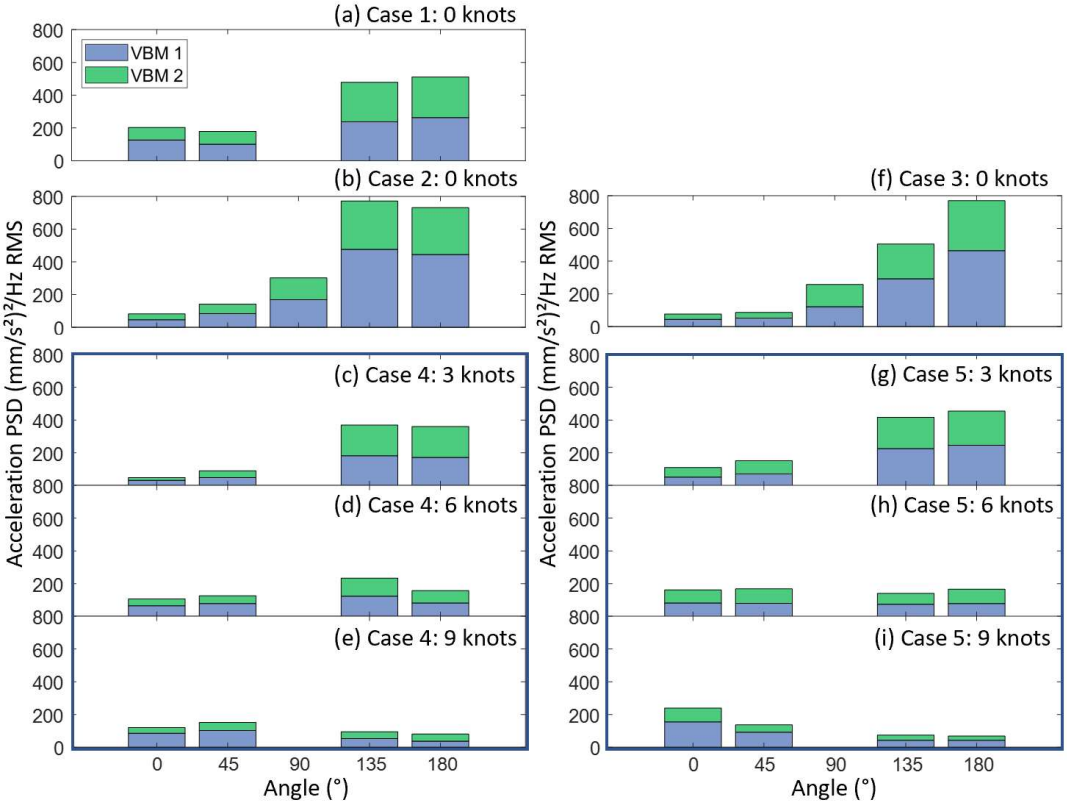

Figure 9.8: Stacked bar graphs showing the total energy associated with the first two VBMs for different ship velocities and relative headings

Figure 9.8 (a), (b) and (f) shows that the RMS magnitude of the VBM response for the stationary vessel typically increases as the relative angle of approaching waves

is adjusted from head on waves to following waves. This is clearly seen for Case 2 and Case 3 in Figure 9.8 (b) and (f) respectively. It can be seen that the first VBM associated with the hogging-sagging mode shape, around 2.25 Hz, is typically dominant. The bar graphs show a stacked representation of the total energy, which accumulates both of the VBM.

Figure 9.8 (c) to (e) and (g) to (i) shows that the VBM response magnitude is generally lower for the manoeuvre sequences performed at speed. VBM 1 is again typically dominant, however, both VBM frequently show similar energy levels. The largest VBM magnitude is associated with stern-quartering seas when the vessel is travelling at 3 knots. Additionally, the flexural response in aft-quartering and following seas significantly decreases as the vessel speed increases.

The highest VBM response is observed for Cases 2 and Case 3, with aft-quartering waves when the vessel was held on station. As whipping typically only involves the first three VBM (Bannister, 1980), and VBM 1 and VBM 2 are dominant, it is expected that the VBM response magnitudes are related to the whipping experienced due to wave slamming. For Case 3, for example, the wave state is assumed constant and the increase in the VBM response across the relative headings can therefore be attributed to the increase in slamming-induced whipping that is encountered when the relative orientation of the vessel in a given wave state is changed. The total VBM response associated with following waves is 10 times the response associated with head on waves. For Case 2 the VBM response associated with following waves is 9 times that of head on waves.

Moreover, Figure 9.1 suggests that the rigid body motion response remains largely similar throughout Case 3, but that the flexural response of the structure rises, reaching a maximum in following seas. With large VBM responses, considerable stress is likely experienced near the midship. Furthermore, the total fatigue damage consists of wave frequency stresses and high frequency stresses due to wave induced-vibration (DNV GL, 2015). Therefore, it is anticipated that when the flexural response dominates, vibration stress governs the contribution to fatigue, whereas when the rigid body response dominates, wave stress governs the fatigue contribution. This should be confirmed with strain measurements, which may provide further insight into the consequence for fatigue and structural damage.

Additionally, since the seamanship of the captain significantly influences the fatigue damage incurred for a given sea state. The vessel speed and relative heading should be adjusted to reduce the whipping induced flexural response. Storhaug and Moe (2007) revealed that the fatigue damage incurred during the worst day corresponded to approximately two months of typical fatigue loading for a large container vessel. Therefore, even short durations of slamming induced whipping may substantially contribute to fatigue damage.

The global ship vibration levels of the hull girders are dependent on modal parameters such as time varying loads, the distribution of stiffness and mass as well as structural and hydrodynamic damping. Damping significantly influences the vibration amplitudes proximate to natural frequencies (Jensen, 2001). Studies have also revealed a dependency of natural frequencies and damping ratios on ship speed (Orlowitz & Brandt, 2014). It is therefore desirable to determine

damping ratios through enhanced FDD (EFDD) techniques (Jacobsen, Andersen & Brincker, 2006; Tarinejad & Damadipour, 2014) or the Multiple-input Ibrahim Time Domain (MITD) method (Brincker & Ventura, 2015). Structural damping affects the magnitude and duration of whipping responses and influences the contribution of whipping to fatigue damage (Brandt, 2011; ISSC Committee II.2, 2018). Therefore, damping ratios should be investigated with respect to whipping and structural damage in further investigations.

10. Conclusion

The primary research objective is to quantify the frequency and severity of wave slamming encountered by the SAA II. This was achieved through full-scale measurements of ship responses to wave slamming, recorded concurrently with the associated vessel operational parameters and environmental conditions that were encountered during purposely executed open water manoeuvres. The wave slamming quantification process comprises of slamming detection, a structural vibration analysis and determining the flexural bending response magnitude.

10.1. Slamming detection

The frequency of wave slamming was first determined using the `findpeaks`, spectrogram and continuous Morlet wavelet transform methods. For each method a single slamming event that is detected across multiple channels is represented as a single peak acceleration amplitude at the earliest time extracted. This also aims to segregate stern and bow slamming. It was determined that a threshold is required to extract significant slams and reject slams of smaller magnitude. Peaks denoting slams in the acceleration-time signal are then related to corresponding peaks in the velocity, which are benchmarked against a MAD velocity statistical outlier thresholds associated with each sensor. The proposed algorithms have been tested on purposely executed manoeuvre case studies. All three slamming detection methods show similar results for the slamming incidence associated with the operational conditions encountered during the manoeuvre sequences. The results appear to correlate better after only considering structurally significant local slams.

The specific differences in slamming detection capabilities were revealed for simulated signals as well as for signal records relating to specific case studies. The advantages and disadvantages of the slamming detection techniques are summarized in Table 10.1. It was evident that the computationally efficient `findpeaks` method is the most viable method for post voyage data processing. However, it is considered more accurate to employ time-frequency representations of the signal for broadband slamming detection, therefore, the cwt is considered a good choice when the processing time of long voyage histories is not the limiting factor.

Table 10.1: The advantages (+) and disadvantages (-) of the slamming detection techniques

`Findpeaks`	
+	Shortest execution time, on average 8.83 times faster than cwt.
+	Simulation of slamming detection for decreasing time intervals fails last.
-	Time of recurrence and peak prominence govern slamming detection.
-	Data driven MAD acceleration outlier and peak prominence threshold.
-	MAD velocity outlier threshold for structurally significant slams.
-	Peak prominence limits detection of significant slams when slamming is prevalent.
Spectrogram	
+	Broadband frequency excitation governs slamming detection.
-	Mean execution time 0.64 times that of cwt, but 5.69 times that of `findpeaks`.
-	Simulation of slamming detection for decreasing magnitudes fails first.
-	`MinThreshold` argument sets a power spectral representation threshold.
-	MAD velocity outlier threshold for structurally significant slams.
-	Largest absolute maximum peak associated with a slam event may lie outside of the search interval relating pixel width to the time domain signal.
Morlet wavelet	
+	Broadband frequency excitation governs slamming detection.
+	Mathematical form resembles an impulse response.
-	Longest execution time.
-	EMD and data driven MAD outlier threshold.
-	MAD velocity outlier threshold for structurally significant slams.
-	Largest absolute maximum peak associated with a slam event may lie outside of the search interval relating pixel width to the time domain signal.

10.2. Wave slamming quantification results

The proposed wave slamming quantification process is summarised in Figure 10.1 and the outputs are further illustrated in Figure 10.2. Figure 10.2 (a) presents the average number of significant slams extracted by the `findpeaks`, spectrogram and Morlet wavelet methods respectively at the site of impact, for the starboard and port side sensors during Case 3. Figure 10.2 (b) presents the absolute acceleration magnitude obtained for each peak detected, at the site of impact. The number of stern slams and the corresponding acceleration magnitude increases when the vessel is held on station in following and stern-quartering seas. Typically, fewer bow slams of smaller magnitude are detected. The segregation of bow and stern slamming corroborates that the SAA II is predisposed to stern slamming and also substantiates that the effects of slamming are exacerbated when the vessel is held stationary during oceanographic activities (Omer & Bekker, 2016).

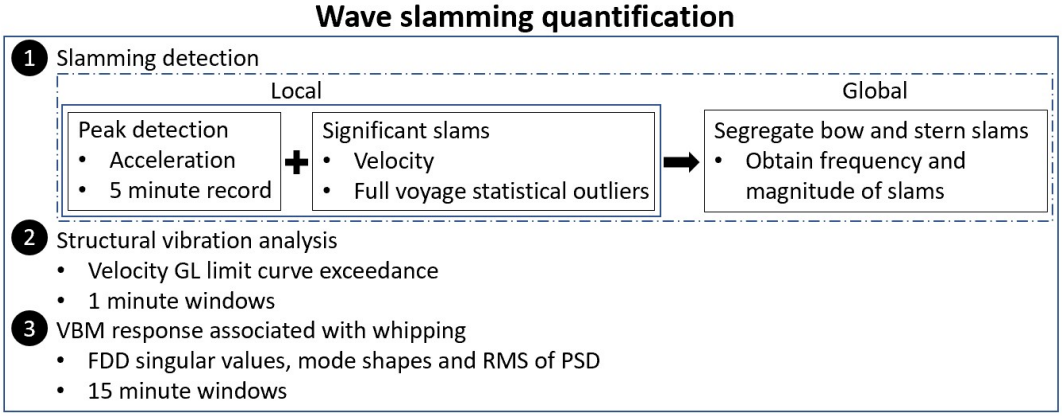

Figure 10.1: Summary of wave slamming quantification process

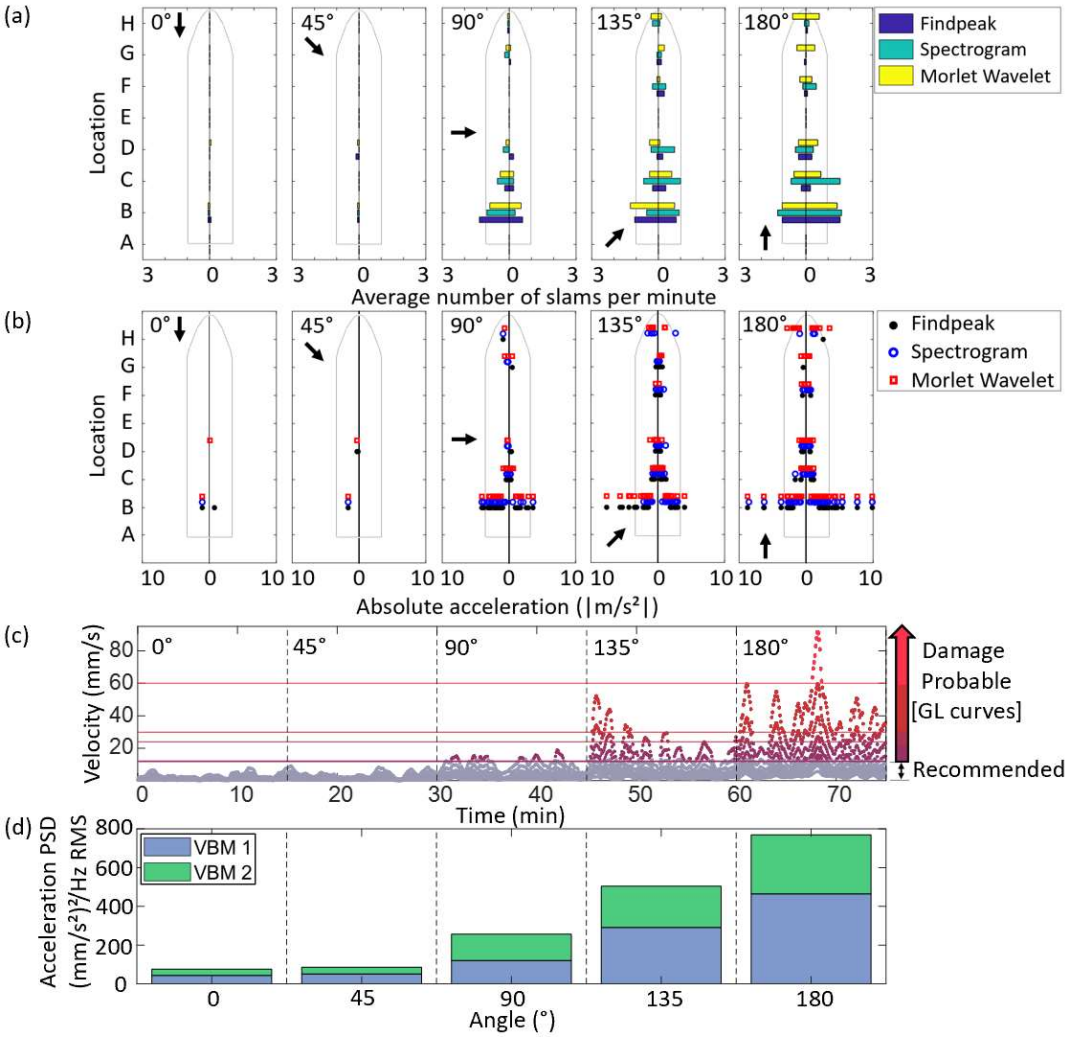

Figure 10.2: Stationary manoeuvre Case 3: (a) average number of slams per minute, (b) absolute peak magnitude of slams, (c) velocity GL limit curve exceedance, (d) RMS value associated with the VBM response

Velocity levels in Figure 10.2 (c) indicate that damage is probable for conditions associated with prevalent stern slams of larger magnitude (Asmussen *et al.*, 2001). The recommended GL limit curve is not exceeded for head and bow-quartering seas with minimal slamming incidence. The highest structural exceedance is seen for following waves with 37% of FFTs exceeding the recommended velocity limit curve, which is more than double the 17% for stern-quartering seas. Velocity levels are shown to be higher at the bow.

Figure 10.2 (d) indicates the RMS PSD values associated with the magnitude of the first two VBM responses. When the vessel is operated on station, the combined VBM RMS values of the bending response increases tenfold for following waves compared to head on waves, in the same wave state. The increase in the bending response is thus associated with slamming incidence detected at the stern, as the relative orientation of the vessel in a given wave state is changed. Therefore, OMA shows that larger magnitude slams induce a larger whipping response due to the large VBM flexural response when slamming is prevalent.

The frequency and magnitude of slamming incidence can similarly be shown to concur with structural exceedance and the associated VBM flexural response for the other stationary manoeuvres and the manoeuvres at speed. Slamming incidence, velocity GL limit curve exceedance and the excessive bending of the hull structure is greatest when the vessel is held on station with following and stern-quartering seas. The slamming and associated VBM whipping response is reduced under these conditions as the wave encounter frequency is decreased with increasing vessel speed. Conversely, as the speed increases, more slamming and a greater bending response is observed for head and bow-quartering seas.

10.3. Future work

OMA shows large VBM responses associated with wave slamming; thus, considerable stress is likely experienced near the midship (DNV GL, 2018). Strain measurements may provide additional insight into stress cycles and fatigue damage incurred by the ship structure (Mao *et al.*, 2010). Damping ratios should also be investigated with respect to whipping and structural damage (ISSC Committee II.2, 2018). Nevertheless, high vibration levels indicate that structural fatigue damage is probable for operational conditions disposed to wave slamming according to the GL limit curves (Asmussen *et al.*, 2001). The quantification of wave slamming presented in this thesis may be integrated with strain measurements to develop a vessel monitoring system that assesses the risk of fatigue damage and necessary time intervals between repairs. Vessel fatigue life is a concern for safety and has economic implications. Similar monitoring systems may benefit other vessels, such as large container ships.

Wave slamming is undesirable as it influences fatigue life and may lead to local structural damage (Constantinescu *et al.*, 2011). Previous research also revealed that the vibration resulting from wave slamming adversely affects human comfort (Omer, 2016). It is therefore desirable to reduce the severity and frequency of wave slamming. The captain may adjust the speed or alter the heading to reduce the effect of wave slamming. He may also try to avoid severe weather conditions through re-routing or delaying the arrival time, however, this conversely influences

the fuel consumption and efficiency of vessel operations, which also require consideration (Kapsenberg, 2011). To better correlate these factors with the prevalence of wave slamming, data from entire voyages should be analysed and consolidated through multi-variate statistics and probability theory. Additionally, the automated quantification of wave slamming can provide further insight into the relationship between wave slamming events and the effect on human factors.

Historical and new voyage wave slamming quantification data, along with operational and environmental conditions, can be integrated with a digital twin model of the vessel. The model can be developed to provide insight for operational decision making. Forecast weather and ocean conditions can be assessed in conjunction with historical wave slamming data for similar conditions to aid route planning. The model can also be developed to advise on the optimal speed and heading for specific conditions encountered to reduce the effect of wave slamming. Thereby the seamanship of the captain is monitored with respect to the historic fatigue loading sustained and future fatigue loading due to wave induced-vibration can be reduced as wave slamming is avoided where possible (Erikstad, 2018).

The SAA II is often held on station during oceanographic activities. Therefore, the preliminary results indicate that the vessel should be held on station with head or bow-quartering seas to reduce the effects of stern slamming. When the vessel is traversing following or stern-quartering seas it is recommended that the vessel speed is increased to minimise the incidence of stern slamming. A detailed cost and fatigue life analysis, should be conducted to determine the optimal vessel speed for head and bow-quartering seas, which is also dependent on the ocean conditions encountered. The preliminary results do show that as the speed increases more slamming and a larger bending response is observed. However, the extent to which the slightly higher bending response and structural vibration levels influence the fatigue life is not known, and it is also important that the vessel is operated economically.

Consequently, results indicate potential structural damage attributed to stern slamming and whipping, which is exacerbated in following seas when the vessel is stationary. Thus, conditions which dispose the vessel to stern slamming should be consolidated through full voyage analyses and avoided whenever possible. The contribution of whipping to fatigue damage should also be investigated further through a conventional fatigue analysis in conjunction with wave slamming quantification techniques.

11. Reference list

Agilent Technologies. 2000. *The fundamentals of signal analysis*.

Alickovic, E., Kevric, J. & Subasi, A. 2018. Performance evaluation of empirical mode decomposition , discrete wavelet transform , and wavelet packed decomposition for automated epileptic seizure detection and prediction. *Biomedical Signal Processing and Control*. 39:94–102.

American Bureau of Shipping. 2011. *ABS guide for slamming loads and strength assessment for vessels*.

Amzallag, C., Gerey, J.P., Robert, J.L. & Bahuaud, J. 1994. Standardization of the rainflow counting method for fatigue analysis. *International Journal of Fatigue*. 16(4):287–293.

Anthony, D.K. & Simón, F. 2009. Generating ‘‘idealised” impulse response functions to improve or repair single degree of freedom system measurements. *Applied Acoustics*. 70(4):531–539.

Asmussen, I., Menzel, W. & Mumm, H. 2001. Ship vibration. In Hamburg *GL Technology*. 8.

Bannister, K.A. 1980. Whipping analysis techniques for ships and submarines. *The Shock and Vibration Bulletin*. 50:83–85.

Barhoumi, M. & Storhaug, G. 2014. Assessment of whipping and springing on a large container vessel. *International Journal of Naval Architecture and Ocean Engineering*. 6(2):442–458.

Bekker, A. 2018. Exploring the blue skies potential of digital twin technology for a polar supply and research vessel. In Helsinki *Proceedings of the 13th International Marine Design Conference*.

Bekker, A. & Van Zijl, C.M. 2019. The use of line detection to identify random impulses in long time histories. In Copenhagen *8th International Operational Modal Analysis Conference*.

Bekker, A., Van Zijl, C.M. & Saunders, C.F.W. 2018. The detection of wave slamming from vibration measurements on a polar supply and research vessel. In Lisbon *The 14th International Conference on Vibration Engineering and Technology of Machinery*.

Bekker, A., van Zijl, C.M. & Saunders, C.F.W. 2018. The detection of wave slamming from vibration measurements on a polar supply and research vessel.

Bertram, V. 2012. *Practical ship hydrodynamics*. 2nd ed. Oxford: Elsevier Ltd.

Bossau, J.C. 2018. The use of anomaly detection algorithms to detect wave slamming. Stellenbosch University. Undergraduate Project Report.

Boyce, W.E. & DiPrim, R.C. 2001. *Elementary differential equations and boundary value problems*. 7th ed. New York: John Wiley & Sons, Inc.

Brandt, A. 2011. *Noise and vibration analysis: signal analysis and experimental procedures*. 1st ed. John Wiley & Sons, Ltd.

Brandt, A. 2013. The ABRAVIBE toolbox for teaching vibration analysis and structural dynamics. In Garden Grove *31st International Modal Analysis Conference*. 131–141.

Brincker, R. & Ventura, C. 2015. *Introduction to operational modal analysis*. John Wiley & Sons, Ltd.

Brincker, R., Zhang, L. & Andersen, P. 2000. Modal identification from ambient responses using frequency domain decomposition. In Texas *The 18th International Modal Analysis Conference (IMAC)*. 625–630.

Brincker, R., Andersen, P. & Jacobsen, N.-J. 2007. Automated frequency domain decomposition for operational modal analysis. In Society for Experimental Mechanics *IMAC-XXIV: A Conference & Exposition on Structural Dynamics*.

BS ISO 20283-2:2008. 2008. Measurement of structural vibration. In *Mechanical Vibration - Measurement of Vibration on Ships*.

Carlton, J.S. & Vlašić, D. 2005. Ship vibration and noise: some topical aspects. In *1st International Ship Noise and Vibration Conference*.

Çengel, Y.A. & Cimbala, J.M. 2014. *Fluid mechanics*. 3rd ed. Singapore: McGraw-Hill Education.

Committee on Large Container Ship Safety. 2013. *Interim report*. Japan.

Constantinescu, A., Alaoui, A., Nême, A. & Rigo, P. 2011. Numerical and experimental studies of simple geometries in slamming. *International Journal of Offshore and Polar Engineering*. 21(3):216–224.

Copernicus Climate Change Service (C3S). 2018. *ERA5: Fifth generation of ECMWF atmospheric reanalyses of the global climate*. [Online], Available: https://cds.climate.copernicus.eu/cdsapp#!/dataset/reanalysis-era5-single-levels?tab=form [2020, May 30].

Department of Environmental Affairs. 2019. *SA Agulhas II - Open day awareness programme*. [Online], Available: https://www.environment.gov.za/event/deptactivity/saagulhas2_opendayprogramme2019 [2020, July 01].

Dessi, D. 2006. Experimental investigation of the ship response to bow and stern slamming loads. In Wuxi: National Defense Industry Press *4th International Conference on Hydroelasticity in Marine Technology*.

Dessi, D. 2014. Whipping-based criterion for the identification of slamming events. *International Journal of Naval Architecture and Ocean Engineering*. 6:1082–1095.

Devleker, K. 2016. *Understanding wavelets*. [Online], Available: https://www.mathworks.com/videos/series/understanding-wavelets-121287.html [2019, December 07].

Dharampal & Mutneja, V. 2015. Methods of image edge detection: a review. *Electrical & Electronic Systems*. 4(2).

DNV GL. 2015. *Fatigue and ultimate strength assessment of container ships including whipping and springing*. [Online], Available: https://rules.dnvgl.com/docs/pdf/DNVGL/CG/2015-10/DNVGL-CG-0153.pdf [2020, March 27].

DNV GL. 2018. *Fatigue assessment of ship structures*. [Online], Available: https://rules.dnvgl.com/docs/pdf/DNVGL/CG/2018-01/DNVGL-CG-0129.pdf [2020, March 27].

DNV GL. 2019. Additional class notations. In *Rules for Classification of Ships*. 29–38.

Dressler, K. 2006. Sinusoidal extraction using an efficient implementation of a multi-resolution FFT. In Montreal: McGill University *9th International Conference on Digital Audio Effects*. 247.

Duda, R.O. & Hart, P.E. 1972. Use of the Hough transformation to detect lines and curves in pictures. *Communications of the Association for Computing Machinery*. 15(1):11–15.

Erikstad, S.O. 2017. Merging physics, big data analytics and simulation for the next-generation digital twins. In *11th Symposium on High-Performance Marine Vehicles*. 139–148.

Erikstad, S.O. 2018. Designing ship digital services. In Tullamore *18th Conference on Computer and IT Applications in the Maritime*. 458–469.

Fan, G.-X. & Liu, Q.H. 2001. The CGFFT method with a discontinuous FFT algorithm. *Microwave and Optical Technology Letters*. 29(1):47–49.

Fricke, W. 2017. Fatigue and fracture of ship structures. In John Wiley & Sons, Ltd. *Encyclopedia of Maritime and Offshore Engineering*. 1–12.

Gaberson, H.A. 2007. Conditions under which displacement, velocity, or

acceleration should be used for diagnostic vibration monitoring. *Vibration Institute Annual Meeting*. 259–270.

Gaberson, H.A. & Chalmers, R.H. 1969. Modal velocity as a criterion of shock severity. *Shock and Vibration Bulletin*. 40(2):31–49.

García Plaza, E. & Núñez López, P.J. 2018. Application of the wavelet packet transform to vibration signals for surface roughness monitoring in CNC turning operations. *Mechanical Systems and Signal Processing*. 98:902–919.

Ghoraani, B. 2010. Time-frequency feauture analysis. Ryerson University.

Graps, A. 1995. An introduction to wavelets. *IEEE Computational Science and Engineering*. 2:1–18.

He, Y. & Liu, Y. 2011. Experimental research into time-frequency characteristics of cavitation noise using wavelet scalogram. *Applied Acoustics*. 72:721–731.

Henry, J.R. & Bailey, F.C. 1970. *Slamming of ships: a critical review of the current state of knowledge*.

Huang, S.-Y. & Bai, Z. 2003. Wavelets, advanced. In 3rd ed. Elsevier Science Ltd. *Encyclopedia of Physical Science and Technology*. 753–771.

Huang, N., Zheng, Q. & Tung, C. 1998. The empirical mode decomposition and the Hilbert spectrum for nonlinear and non-stationary time series analysis. *Proceedings of The Royal Society A Mathematical Physical and Engineering Sciences*. 904–993.

Inman, D.J. 2014. *Engineering vibration*. 4th ed. Pearson Education Ltd.

International Association of Classification Societies. 2016. Requirements concerning polar class.

ISSC Committee II.2. 2009. Dynamic response. In Vol. 1. Seoul *17th International Ship and Offshore Structures Congress*. 289–374.

ISSC Committee II.2. 2018. Dynamic response. In Vol. 1. Amsterdam *20th International Ship and offshore Structures Congress*. 260–261.

Jacobsen, N.J., Andersen, P. & Brincker, R. 2006. Using enhanced frequency domain decomposition as a robust technique to harmonic excitation in operational modal analysis. In *ISMA2006: International Conference on Noise and Vibration Engineering*. 3129–3140.

Jensen, J.J. 2001. *Load and global response of ships*. Elsevier Ltd.

Kapsenberg, G.K. 2011. Slamming of ships: where are we now? *Philosophical Transactions of the Royal Society A: Mathematical, Physical and Engineering*

Sciences. 369:2892–2919.

Von Kármán, T. 1929. *The impact on seaplane floats during landing*. Washington DC: National Advisory Committee for Aeronautics.

Khanam, S., Tandon, N. & Dutt, J.K. 2014. Fault size estimation in the outer race of ball bearing using discrete wavelet transform of the vibration signal. *Procedia Technology*. 14:12–19.

Kıymıka, M.K., Güler, İ., Dizibüyük, A. & Akın, M. 2005. Comparison of STFT and wavelet transform methods in determining epileptic seizure activity in EEG signals for real-time application. *Computers in Biology and Medicine*. 35:603–616.

Kowalska-Koczwara, A. & Stypuła, K. 2018. Influence of crest factor on evaluation of human perception of traffic vibration. *Journal of Measurements in Engineering*. 6(4):250–255.

Kumar, A. & Kumar, R. 2017. Time-frequency analysis and support vector machine in automatic detection of defect from vibration signal of centrifugal pump. *Measurement*. 108:119–133.

Lee, J.A. 2008. Technical management of VLCC/VLBC hull structures based on safety case principles. Liverpool John Moores University.

Leys, C., Ley, C., Klein, O., Bernard, P. & Licata, L. 2013. Do not use standard deviation around the mean, use absolute deviation around the median. *Journal of Experimental Social Psychology*. 49(4):764–766.

Lloyd's Register. 2006. *Ship vibration and noise guidance notes*. London.

Lloyd's Register. 2015. *General overview of ship structural vibration problems*. London.

Loughlin, P.J., Pitton, J.W. & Atlas, L.E. 1992. Proper time-frequency energy distributions and the Heisenberg uncertainty principle. In Victoria: IEEE *Proceedings of the IEEE-SP International Symposium on Time-Frequency and Time-Scale Analysis*. 6–9.

Magalhães, F. & Cunha, Á. 2011. Explaining operational modal analysis with data from an arch bridge. *Mechanical Systems and Signal Processing*. 25(5):1431–1450.

Mao, W., Ringsberg, J.W., Rychlik, I. & Storhaug, G. 2010. Development of a fatigue model useful in ship routing design. *Journal of Ship Research*. 54(4):281–293.

Marine Accident Investigation Branch. 2008. *Report on the investigation of the structural failure of MSC Napoli*. [Online], Available:

http://news.bbc.co.uk/2/shared/bsp/hi/pdfs/21_04_08_napoli.pdf.

MathWorks. 2007. *findpeaks*. [Online], Available: https://www.mathworks.com/help/signal/ref/findpeaks.html [2019, April 24].

MathWorks. 2016. *cwt*. [Online], Available: https://www.mathworks.com/help/wavelet/ref/cwt.html [2020, February 10].

MathWorks. 2017a. *isoutlier*. [Online], Available: https://www.mathworks.com/help/matlab/ref/isoutlier.html [2019, December 04].

MathWorks. 2017b. *pspectrum*. [Online], Available: https://www.mathworks.com/help/signal/ref/pspectrum.html [2020, February 11].

MathWorks. 2018a. *emd*. [Online], Available: https://www.mathworks.com/help/signal/ref/emd.html [2020, February 10].

MathWorks. 2018b. *cwtfilterbank*. [Online], Available: https://www.mathworks.com/help/wavelet/ref/cwtfilterbank.html [2020, February 10].

MathWorks. n.d. *color specification*. [Online], Available: https://www.mathworks.com/help/matlab/ref/colorspec.html [2018a, October 10].

MathWorks. n.d. *hough*. [Online], Available: https://www.mathworks.com/help/images/ref/hough.html [2018b, July 20].

Melanie Gosling. 2013. SA Agulhas II sent to Marion Island. *Cape Times* (Cape Town). 25 March. [Online], Available: https://www.iol.co.za/news/south-africa/western-cape/sa-agulhas-ii-sent-to-marion-island-1491301.

Mussomeli, A., Meeker, B., Shepley, S. & Schatsky, D. 2018. *Signals for strategists: expecting digital twins*. [Online], Available: https://www2.deloitte.com/insights/us/en/focus/signals-for-strategists/understanding-digital-twin-technology.html [2019, April 09].

Nickerson, B. & Bekker, A. 2017. *Surveying the SA Agulhas II*. [Online], Available: http://www.ee.co.za/article/surveying-sa-agulhas-ii.html [2019, April 10].

Ochi, M.K. 1964. Prediction of occurrence and severity of ship slamming at sea. In Bergen *5th Symposium on Naval Hydrodynamics*. 545–596.

Omer, H. 2016. The impact of wave slamming induced vibration on human factors and equipment on-board the S.A. Agulhas II. Stellenbosch University.

Omer, H. & Bekker, A. 2016. Detection of wave slamming sites from ship

deflections. *R & D Journal of the South African Institution of Mechanical Engineering*. 32:50–57.

Orlowitz, E. & Brandt, A. 2014. Operational modal analysis for dynamic characterization of a Ro-Lo ship. *Journal of Ship Research*. 58(4):216–224.

Öztürk, C. 1995. Development of experimental techniques to minimise the leakage errors involved in FFT based measurements. *Applied Acoustics*. 44(4):375–382.

Pastor, M., Binda, M. & Harčarik, T. 2012. Modal assurance criterion. *Procedia Engineering*. 48:543–548.

Pijanowski, B.C., Villanueva-Rivera, L.J., Dumyahn, S.L., Farina, A., Krause, B.L., Napoletano, B.M., Gage, S.H. & Pieretti, N. 2011. Soundscape ecology: the science of sound in the landscape. *BioScience*. 61(3):203–216.

Pintelon, R. & Schoukens, J. 1990. Real-time integration and differentiation of analog-signals by means of digital filtering. *IEEE Transactions on Instrumentation and Measurement*. 39(6):923–927.

Pitas, I. 2000. *Digital image processing algorithms and applications*. John Wiley & Sons, Ltd.

Rabi, J., Balusamy, T. & Jawahar, R.R. 2019. Analysis of vibration signal responses on pre induced tunnel defects in friction stir welding using wavelet transform and empirical mode decomposition. *Defence Technology*. 15(6):885–896.

Rychlik, I. 1987. A new definition of the rainflow cycle counting method. *International Journal of Fatigue*. 9(2):119–121.

Samundiswary, P. & Subbarao, M.V. 2016. Time-frequency analysis of non-stationary signals using frequency slice wavelet transform. In Coimbatore: IEEE *10th International conference on intelligent systems and control (ISCO)*.

Saunders, C.F.W. 2018. The detection and analysis of wave slamming from full-scale ship measurements. Stellenbosch University.

Sheen, Y. 2009. On the study of applying Morlet wavelet to the Hilbert transform for the envelope detection of bearing vibrations. *Mechanical Systems and Signal Processing*. 23:1518–1527.

Smith, C.C., Dahl, J.F. & Thornhill, R.J. 1996. The duality of leakage and aliasing and improved digital spectral analysis techniques. *Journal of Dynamic Systems, Measurement, and Control*. 118(4):741–747.

Soal, K.I. 2014. Vibration response of the polar supply and research vessel the S.A. Agulhas II in Antarctica and the Southern Ocean. Stellenbosch

University.

Soal, K. & Bekker, A. 2013. Whole-body vibration comfort on the S.A. Agulhas II Polar Supply and Research Vessel during a voyage to Antarctica. In *48th United Kingdom Conference on Human Responses to Vibration*. 16–18.

Soal, K., Bienert, J. & Bekker, A. 2015. Operational modal analysis on the polar supply and research vessel the S.A. Agulhas II. In Vol. 6. Gijon *6th International Operational Modal Analysis Conference*.

Storhaug, G. & Moe, E. 2007. Measurements of wave induced vibrations onboard a large container vessel operating in harsh environment. In Houston *10th International Symposium on Practical Design of Ships and Other Floating Structures*. 419–427.

Susanto, A., Liu, C.H., Yamada, K., Hwang, Y.R., Tanaka, R. & Sekiya, K. 2018. Application of Hilbert–Huang transform for vibration signal analysis in end-milling. *Precision Engineering*. 53:263–277.

Tarinejad, R. & Damadipour, M. 2014. Modal identification of structures by a novel approach based on FDD-wavelet method. *Journal of Sound and Vibration*. 333:1024–1045.

Thomas, G., Davis, M.R., Holloway, D.S. & Roberts, T. 2015. The effect of slamming and whipping on the fatigue life of a high-speed catamaran. *Australian Journal of Mechanical Engineering*. 3(2):165–174.

Wang, S. & Guedes Soares, C. 2017. Review of ship slamming loads and responses. *Journal of Marine Science and Application*. 16(4):427–445.

White, N., Lee, Y. & Wang, Z. 2012. Guidance notes on whipping and springing assessment. In Glasgow *11th Int. Marine Design Conference*.

Xun, J. & Yan, S. 2008. A revised Hilbert – Huang transformation based on the neural networks and its application in vibration signal analysis of a deployable structure. *Mechanical Systems and Signal Processing*. 22:1705–1723.

Yang, W.X. & Ren, X.M. 2004. Detecting impulses in mechanical signals by wavelets. *EURASIP Journal on Applied Signal Processing*. 1156–1162.

Zeiler, A., Faltermeier, R., Keck, I.R., Tomé, A.M., Puntonet, C.G. & Lang, E.W. 2010. Empirical mode decomposition - an introduction. In Barcelona *International Joint Conference on Neural Networks*. 1–8.

Van Zijl, C.M. 2020. Operational Modal Analysis on the SA Agulhas II. Stellenbosch University.

Van Zijl, C.M. & Bekker, A. 2018. Variations in vibration responses of an ice-going vessel during wave slamming. In *31st Conference on Condition Monitoring*

and Diagnostic Engineering Management. 1–9.

Appendix A. Supplementary analysis

A.1. Median absolute deviation outlier threshold

Figure A1 (a) shows four slams extracted from an acceleration-time signal that exceed the MAD acceleration threshold of ±0.607 m/s^2 obtained for the port side steering gear room sensor. Figure A1 (b) shows that only one of these extracted slams corresponds to a peak velocity value, which exceeds the MAD velocity threshold of 25.7 mm/s. Peak 3 and peak 4 have magnitudes of 1.17 m/s² and - 1.04 m/s² respectively. Peak 3 therefore has a larger acceleration magnitude, however, only peak 4 is considered structurally significant as it relates to a larger velocity magnitude than the other slams, as seen by peak 5. It is noted that slam 4 exhibits a clear transient whipping response with a slower decay than is observed for the other slams. As the whipping decay coefficient increases fatigue life also increases, which further suggests that slam 4 is structurally significant (Thomas *et al.*, 2015).

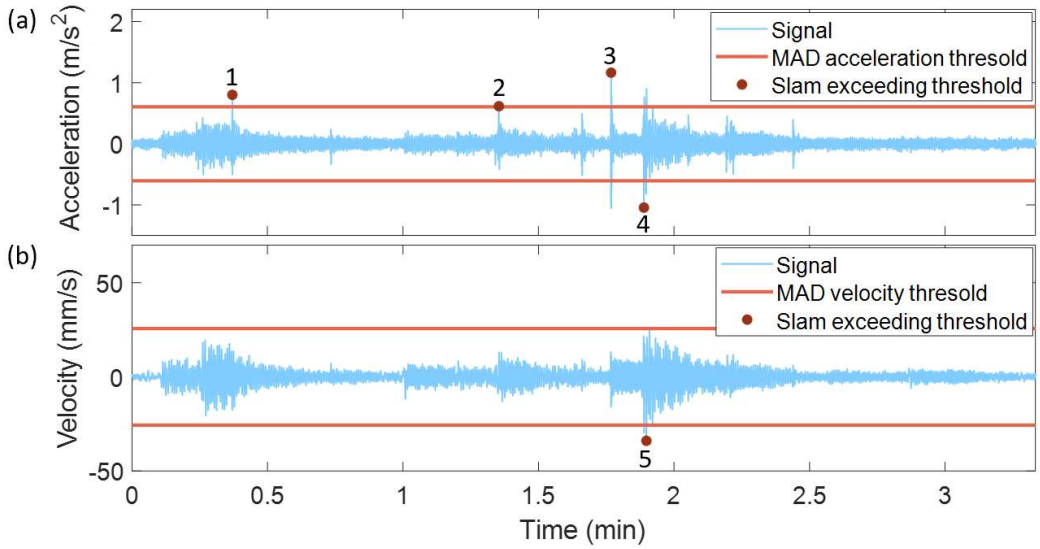

Figure A1: (a) Slams exceeding the MAD acceleration threshold and (b) slams exceeding the MAD velocity threshold, recorded in the port side steering gear room during Case 3 with head on waves

While slamming is prevalent, as it is for the vessel held on station with following waves, many significant slams are extracted from the acceleration signal, as seen in Figure A2 (a). Even slams which exhibit less transient whipping decay than other slams are considered significant. In Figure A2 both the acceleration and velocity MAD thresholds are frequently exceeded as the signal is typically larger in magnitude than for head on waves. Only smaller magnitude peaks in the acceleration and corresponding velocity signal are not considered significant. Two slams were extracted from the acceleration-time signal, which do exceed the MAD acceleration threshold. However, these slams are not considered significant due to the corresponding low velocity levels. Therefore, it is shown that both the slam magnitude and the transient whipping response influence the velocity level and thus the identification of structurally significant slams.

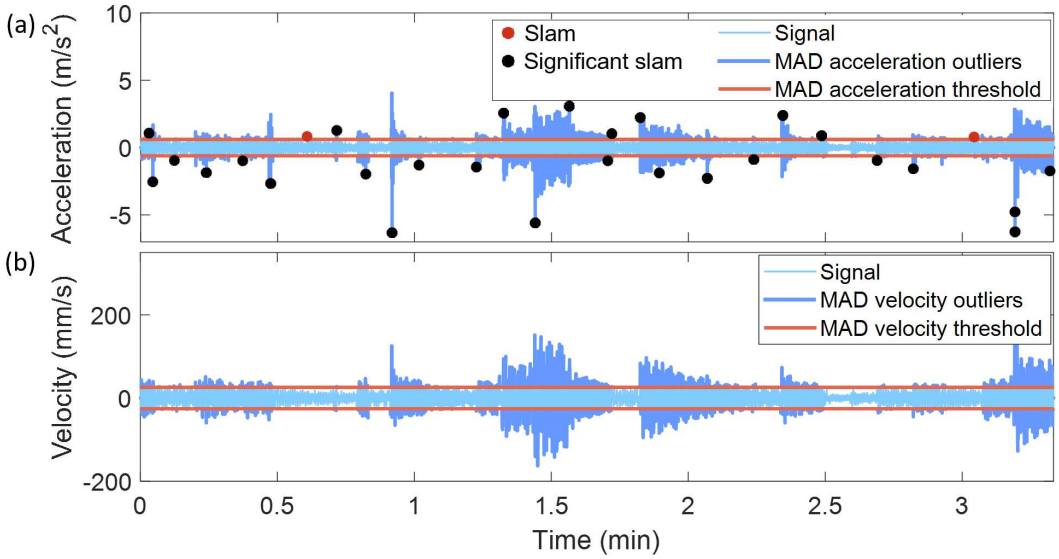

Figure A2: (a) MAD acceleration outliers and significant slams, which correspond to MAD velocity outliers in (b), recorded in the port side steering gear room during Case 3 with following waves

A.2. Time-frequency representations for two different relative heading conditions

Figure A3 and Figure A4 present the scalogram and spectrogram images analysed in Section 7.2, where the `findpeaks`, spectrogram and Morlet wavelet slamming detection techniques are compared for specific case studies.

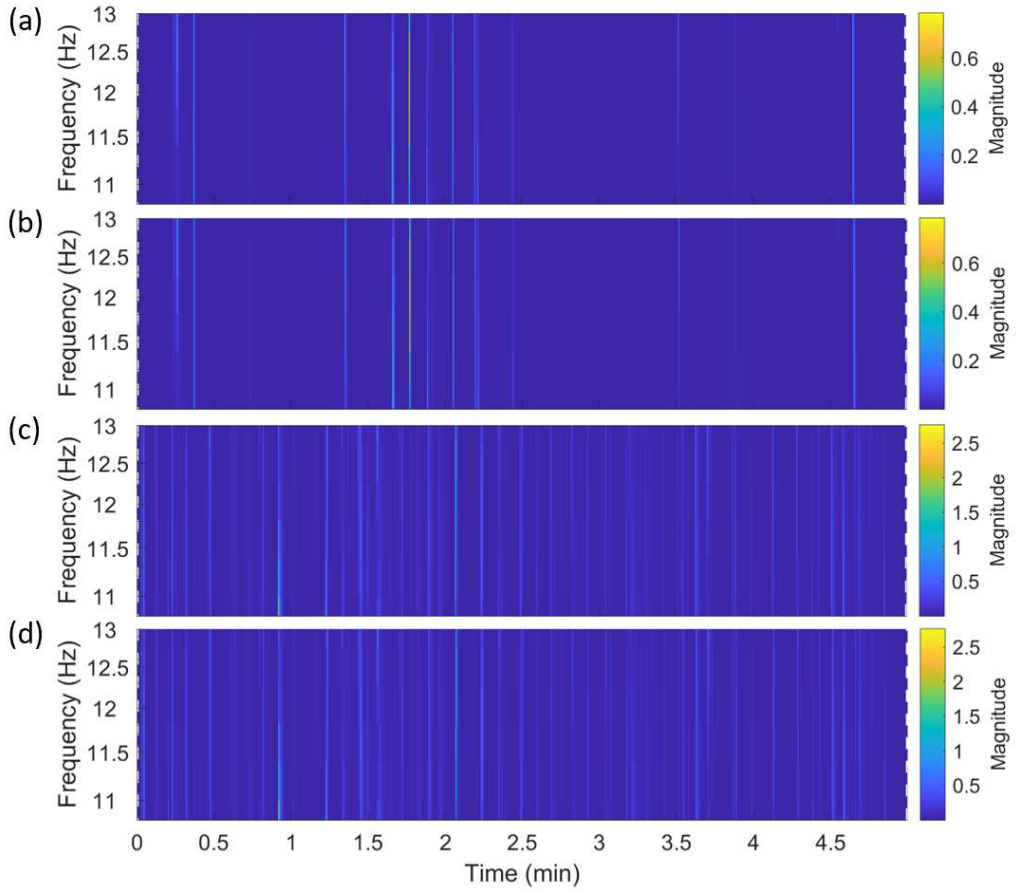

Figure A3: Comparison of scalogram images for (a) the starboard and (b) the port side steering gear room during Case 3 with head on waves as well as (c) the starboard and (d) the port side steering gear room during Case 3 with following waves (related slamming detection presented in Figure 7.2).

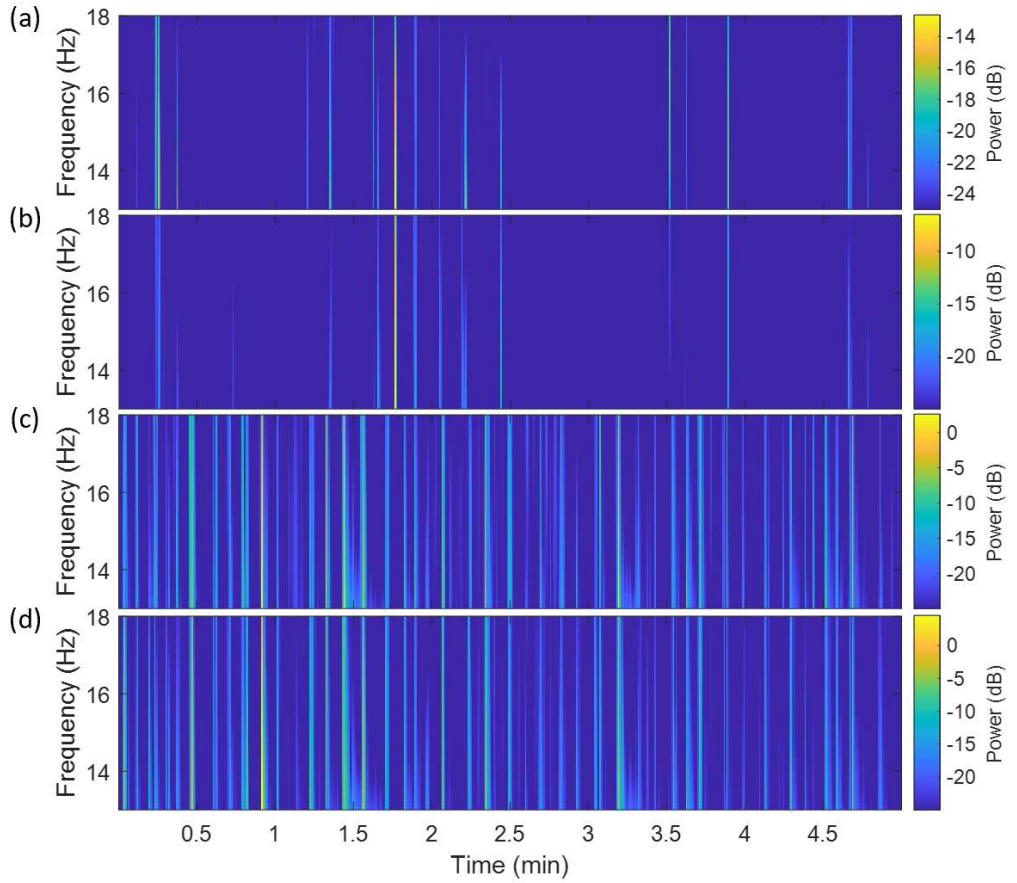

Figure A4: Comparison of spectrogram images for (a) the starboard and (b) the port side steering gear room during Case 3 with head on waves as well as (c) the starboard and (d) the port side steering gear room during Case 3 with following waves (related slamming detection presented in Figure 7.2).

A.3. DNV GL structural vibration analysis

The previous statement claiming that DNV GL's assessment of the RMS velocity level is not considered optimal for the structural assessment of slamming cases in this study is substantiated by the fact that the RMS velocity did not exceed 45 mm/s for any of the manoeuvre case studies. Figure A5 illustrates that for all of the case studies the RMS velocity remains well below the recommended level for different ship velocities as well as relative headings.

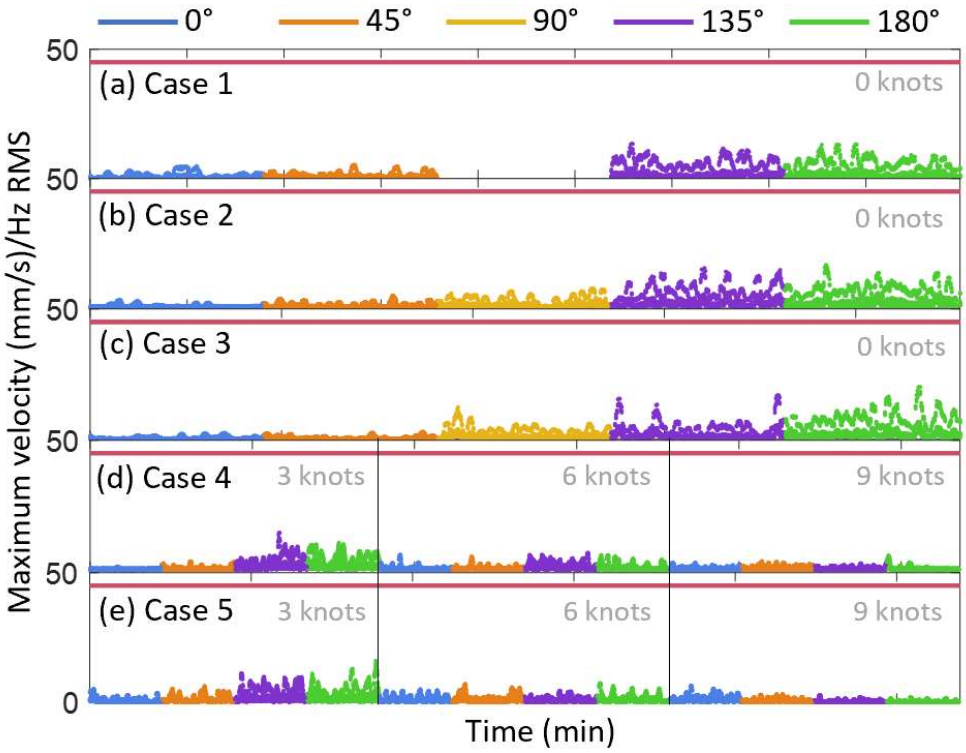

Figure A5: DNV GL assessment of RMS levels at discrete frequencies for the frequency range 4 to 200 Hz, for the manoeuvre case studies

The signal was high-pass and low-pass filtered for analysis in the frequency range of 4 to 200 Hz. The FFT is generated with a 2048-point flattop window, with 50% overlap, and is averaged over the minimum recommended time period of 30 seconds. The 30 second time interval is implemented as a sliding interval with a 5 second offset. The 2048-point window allows for 1024 spectral lines and a resolution of 0.1953 Hz, and exceeds the requirement of at least 400 spectral lines. The ABRAVIBE function `alinspec` is used to produce a linear, RMS weighted spectrum as if it were a periodic signal. A peak in the FFT is interpreted as a sine at that frequency with an RMS value corresponding to the peak value. The maximum RMS velocity at a specific frequency of the FFT was extracted for each 30 second interval and the results are plotted above for the five case studies and all of the relevant channels.

Appendix B. MATLAB code

B.1. Slamming detection

B.1.1. Measurement selection and signal conditioning

```
close all
clc
%
tic
%%%%%%%%%%%%%%%%%%%%%%%%%%%%%%%%%%%%%%%%%%%%%%%%%%%%%%%%%%%%%%%%%%%%%%%%%%%%%%%%
% USER INPUTS
Winter=0; % Winter Cruise == 1, Spring Cruise == 0
% Choose the folder of interest:
raw_folder_directory = 'C:\Users\USER\Documents\Cases\SpringData';
start_file='a0111254';
end_file='a0112254';
start_time='18/11/19 11:13:00.000';
end_time='18/11/19 11:21:00.000';
start_time=datenum(start_time,'dd/mm/yy HH:MM:SS.FFF');
end_time=datenum(end_time,'dd/mm/yy HH:MM:SS.FFF');

% Choose the channels of interest:
if Winter==1
    IDX= [26,29,30,23,24,21,22,3,4,19,17,20,18,9,11];% - WINTER CRUISE!
    DC=[2,3,8,14,15];% index of DC accelerometers winter
else
    IDX= [29,30,23,24,21,22,3,4,19,17,20,18,9,11];% - SPRING CRUISE!
    DC=[1,2,7,13,14];% index of DC accelerometers spring
end
%%%%%%%%%%%%%%%%%%%%%%%%%%%%%%%%%%%%%%%%%%%%%%%%%%%%%%%%%%%%%%%%%%%%%%%%%%%%%%%%
%Folder creation
%Change structure name to identify the case
result_folder='Output_cwt_180_V9';
Results='Results_cwt';
Output='output_cwt';

%To save plot results:
plot_folder='Lines_cwt_180';
mkdir(raw_folder_directory,plot_folder);
plot_folder_directory = fullfile(raw_folder_directory,plot_folder);

mkdir(raw_folder_directory,result_folder);
result_file_directory = fullfile(raw_folder_directory,result_folder);
Result_file =  fullfile(result_file_directory,'Results_cwt.mat');
out_file =  fullfile(result_file_directory,'output_cwt.mat');

%Folder selected
raw_file_directory=[raw_folder_directory,'\*.mat'];
filelist = ls(raw_file_directory);
list = filelist(:,1:8);
numfiles = size(filelist,1);
start_file_name = fullfile(raw_folder_directory,filelist(1,:));
start_handle = load(start_file_name);
%%%%%%%%%%%%%%%%%%%%%%%%%%%%%%%%%%%%%%%%%%%%%%%%%%%%%%%%%%%%%%%%%%%%%%%%%%%%%%%%
% finding the files for the time of interest
for fileidx = 1:numfiles
    ts = strcmp(list(fileidx,:),start_file);
    if ts == 1
        startsesh = fileidx;
        current_file_name = fullfile(raw_folder_directory,...
                            filelist(fileidx,:));
```

```
        start_handle = load(current_file_name);
        start_t = start_handle.n_SS_B01_S_X__X.function_record.↙
TL_export_properties_annotation.absolute_time(1:19);
        start_number = datenum(start_t);
    end
    tf = strcmp(list(fileidx,:),end_file);
    if tf == 1
        endsesh = fileidx;
        break
    end
end
files=endsesh-startsesh+1;
%%%%%%%%%%%%%%%%%%%%%%%%%%%%%%%%%%%%%%%%%%%%%%%%%%%%%%%%%%%%%%%%%%%%%%%%%%%%
% Signal parameters
fs=1/start_handle.n_SS_D801_P_Y__Y.x_values.increment;
period=1/fs;
tRecord=1/fs*start_handle.n_SS_D801_P_Y__Y.x_values.number_of_values;
leng=tRecord/60;% total time of recording in minutes
%%%%%%%%%%%%%%%%%%%%%%%%%%%%%%%%%%%%%%%%%%%%%%%%%%%%%%%%%%%%%%%%%%%%%%%%%%%%
% load the data for the duration selected:
% check the channel order for the LoadData function
% check number of channels
channels=length(IDX);%number of channels
Yd_raw = zeros(tRecord/period*files,channels);
end_number = start_number + size(Yd_raw,1)/fs/60/60/24;
t_abs = start_number:1/fs/60/60/24:end_number - 1/fs/60/60/24;
cnt=0;
for fileidx = startsesh:endsesh
    current_file_name = fullfile(raw_folder_directory,filelist(fileidx,:));
    h = load(current_file_name);
    if Winter==1
        Y_raw = LoadData_15Chan(h);% - WINTER CRUISE!
    else
        Y_raw = LoadData_14Chan_Spring(h);% - SPRING CRUISE!
    end
    Yd_raw((tRecord/period*cnt+1):(tRecord/period*(cnt+1)),:)= Y_raw;
    cnt=cnt+1;
end
%%%%%%%%%%%%%%%%%%%%%%%%%%%%%%%%%%%%%%%%%%%%%%%%%%%%%%%%%%%%%%%%%%%%%%%%%%%%
% integrate time sinal
mm=1000;%Convert data to mm/s^2
iir=zeros(23,length(IDX));
velocity = [timeint(mm.*Yd_raw,fs,'IIR',1);iir];%-23 samples
%%%%%%%%%%%%%%%%%%%%%%%%%%%%%%%%%%%%%%%%%%%%%%%%%%%%%%%%%%%%%%%%%%%%%%%%%%%%
% filtering
% Slamming ID:
Y_fH = HPF_2Hz(Yd_raw,fs,leng,channels);% High-pass filter > 2 Hz
Y_f = LPF_20Hz(Y_fH,fs,channels);% Low-pass filter < 20 Hz
% Velocity MAD benchmarking:
V_fH = HPF_1Hz(velocity,fs,leng,channels);% High-pass filter > 1 Hz
V_f = LPF_100Hz(V_fH,fs,channels);% Low-pass filter < 100 Hz
%%%%%%%%%%%%%%%%%%%%%%%%%%%%%%%%%%%%%%%%%%%%%%%%%%%%%%%%%%%%%%%%%%%%%%%%%%%%
% Removing unwanted time data for peak detection
Y_f = RemoveTime(Y_f,t_abs,startsesh,endsesh,start_time,end_time,files,...
      tRecord/period);
t=(0:1/fs:(length(Y_f(:,1))-1)/fs)';%time in seconds
%%%%%%%%%%%%%%%%%%%%%%%%%%%%%%%%%%%%%%%%%%%%%%%%%%%%%%%%%%%%%%%%%%%%%%%%%%%%
if Winter==1
    benchmark=[6.34,25.04,25.70,10.13,9.98,5.70,5.57,9.10,21.16,8.74,...
               8.83,8.06,8.38,31.22,31.71]; %MAD from full voyage
else
    benchmark=[25.04,25.70,10.13,9.98,5.70,5.57,9.10,21.16,8.74,8.83,...
               8.06,8.38,31.22,31.71];
end
```

```
%%%%%%%%%%%%%%%%%%%%%%%%%%%%%%%%%%%%%%%%%%%%%%%%%%%%%%%%%%%%%%%%%%%%%%%%%%%%%%%%
%% Continuous Morlet Wavelet
%%%%%%%%%%%%%%%%%%%%%%%%%%%%%%%%%%%%%%%%%%%%%%%%%%%%%%%%%%%%%%%%%%%%%%%%%%%%%%%%
output_cwt=struct('t_cat',[],'acc_cat',[],'vel_cat',[],'t',[],'acc',[]);

% create a filter bank for cwt
fb=cwtfilterbank('SignalLength',tRecord/period,...
    'Wavelet','amor','SamplingFrequency',fs,...
    'FrequencyLimits',[10 15]);

% detect peaks for all channels in 5 minute records:
for idx = 1:length(IDX) %loop through channels
    [imf]=emd(Y_f(:,idx),'Interpolation','pchip');
    numIMF=1;
    IMF=imf(:,numIMF);
    [output_cwt(idx)] = Processchan_cwt(Y_f(:,idx),t,idx,tRecord,fs,...
        files,fb,IMF,plot_folder_directory);
   %apply benchmark
   if (length(output_cwt(idx).t_cat)>0)
   MaxV=zeros(length(output_cwt(idx).t_cat),1);
   [LIA,LOCB] = ismember(output_cwt(idx).t_cat,t);
    for i=1:length(LOCB)
        % max velocity in 2s interval
        MaxV(i)=max(abs(V_f(LOCB(i)-2048+1:LOCB(i)+2048,idx)));
        Exd=(MaxV>=benchmark(idx));
    end
    output_cwt(idx).vel_cat=MaxV;
    % Only significant slams
    output_cwt(idx).t=output_cwt(idx).t_cat(Exd);
    output_cwt(idx).acc=output_cwt(idx).acc_cat(Exd);
   end
end
%%%%%%%%%%%%%%%%%%%%%%%%%%%%%%%%%%%%%%%%%%%%%%%%%%%%%%%%%%%%%%%%%%%%%%%%%%%%%%%%
%% Spectrogram
%%%%%%%%%%%%%%%%%%%%%%%%%%%%%%%%%%%%%%%%%%%%%%%%%%%%%%%%%%%%%%%%%%%%%%%%%%%%%%%%
output_spect=struct('t_cat',[],'acc_cat',[],'vel_cat',[],'t',[],'acc',[]);
% detect peaks for all channels in 5 minute records:
for idx = 1:length(IDX) %loop through channels
   [output_spect(idx)] = Processchan_spect(Y_f(:,idx),t,idx,tRecord,period,...
                         fs,files,DC,plot_folder_directory);
   %apply benchmark
   if (length(output_spect(idx).t_cat)>0)
   MaxV=zeros(length(output_spect(idx).t_cat),1);
   [LIA,LOCB] = ismember(output_spect(idx).t_cat,t);
    for i=1:length(LOCB)
        % max velocity in 2s interval
        MaxV(i)=max(abs(V_f(LOCB(i)-2048+1:LOCB(i)+2048,idx)));
        Exd=(MaxV>=benchmark(idx));
    end
    output_spect(idx).vel_cat=MaxV;
    % Only significant slams
    output_spect(idx).t=output_spect(idx).t_cat(Exd);
    output_spect(idx).acc=output_spect(idx).acc_cat(Exd);
   end
end
%%%%%%%%%%%%%%%%%%%%%%%%%%%%%%%%%%%%%%%%%%%%%%%%%%%%%%%%%%%%%%%%%%%%%%%%%%%%%%%%
%% Findpeaks
%%%%%%%%%%%%%%%%%%%%%%%%%%%%%%%%%%%%%%%%%%%%%%%%%%%%%%%%%%%%%%%%%%%%%%%%%%%%%%%%
output_fpk=struct('t_cat',[],'acc_cat',[],'vel_cat',[],'t',[],'acc',[]);
% detect peaks for all channels in 5 minute records:
for idx = 1:length(IDX) %loop through channels
   [output_fpk(idx)] = Processchan_fpk(Y_f(:,idx),t,idx,tRecord,period,fs,...
                       files,plot_folder_directory);
```

```
183     %apply benchmark
184     if (length(output_fpk(idx).t_cat)>0)
185     MaxV=zeros(length(output_fpk(idx).t_cat),1);
186     [LIA,LOCB] = ismember(output_fpk(idx).t_cat,t);
187      for i=1:length(LOCB)
188          % max velocity in 2s interval
189          MaxV(i)=max(abs(V_f(LOCB(i)-2048+1:LOCB(i)+2048,idx)));
190          Exd=(MaxV>=benchmark(idx));
191      end
192      output_fpk(idx).vel_cat=MaxV;
193      % Only significant slams
194      output_fpk(idx).t=output_fpk(idx).t_cat(Exd);
195      output_fpk(idx).acc=output_fpk(idx).acc_cat(Exd);
196     end
197 end
198 %% %%%%%%%%%%%%%%%%%%%%%%%%%%%%%%%%%%%%%%%%%%%%%%%%%%%%%%%%%%%%%%%%%%%%%%%%%%%
199 % ignore port side stearing gear sensor for Spring Cruise, Case 2
200 if strcmp(raw_folder_directory(end-18:end),'20191019_132142_Run')==1
201     output_cwt(2).t_cat=[];
202     output_cwt(2).acc_cat=[];
203 end
204 % Saving parameters
205 Results_cwt.tabs_strt = t_abs(1,1);
206 Results_cwt.t = t;
207 Results_cwt.y = Y_f;
208 Results_cwt.v =V_f;
209 Results_cwt.IDX=IDX;
210 Results_cwt.t_fin=toc;
211 save(Result_file,Results)
212 save(out_file,Output)
213 %%%%%%%%%%%%%%%%%%%%%%%%%%%%%%%%%%%%%%%%%%%%%%%%%%%%%%%%%%%%%%%%%%%%%%%%%%%

214 %% Earliest Slam Time
215 close all
216 plot_folder_directory = fullfile(raw_folder_directory,result_folder);
217 seconds = 0:1:tRecord*files;
218 tol=2;%no of accelerometers that detect a slam
219 if Winter==1
220     B_IDX = [8:9]; % Bridge idx winter
221 else
222     B_IDX = [7:8]; % Bridge idx spring
223 end
224
225 [channel_slams,tmin,I,acc_min,t_rank1,acc_rank] = ChannelsSlams(IDX,seconds,↙
output_cwt,plot_folder_directory,tol,B_IDX);
226
227 % Saving parameters
228 Results_cwt.channel_slams=channel_slams';%total slams detected for each channel
229 Results_cwt.tmin=tmin;%the earliest time of the slam recorded
230 Results_cwt.I=I;%channel position of earliest time
231 Results_cwt.acc_min=acc_min;%the peak acceleration of the earliest slam
232 Results_cwt.t_rank1=t_rank1;
233 Results_cwt.acc_rank=acc_rank;
234 save(Result_file,Results)
```

B.1.2. Findpeaks

```
function [output] = Processchan_fpk(y,t,idx,tRecord,period,fs,files,plot_folder_directory)
 disp(['Started working on channel ' num2str(idx)])
 output=struct('t_cat',[],'acc_cat',[],'vel_cat',[],'t',[],'acc',[]);
 [TFb,Lb,Ub,Cb] = isoutlier(y(y~=0));
    for sect=1:files %loop for time series
        tsect= t((tRecord/period*sect-tRecord/period+1:tRecord/period*sect),1)';
        ysect= y((tRecord/period*sect-tRecord/period)+1:(tRecord/period*sect),1)';
        %%%%%%%%%%%%%%%%%%%%%%%%%%%%%%%%%%%%%%%%%%%%%%%%%%%%%%%%%%%%%%%%%%%%%%%
        % Ignore signal less than Threshold
        % absolute because findpeaks only works for positive values
        Thresh=max(abs([Ub Lb]));
        Threshold = Thresh*ones(size(tsect));
        signal_thresh = abs(ysect) > Threshold;
        % all components larger than Threshold set to one
        % all components less than Threshold set to zero
        signal_thresh = signal_thresh.*ysect;
        %%%%%%%%%%%%%%%%%%%%%%%%%%%%%%%%%%%%%%%%%%%%%%%%%%%%%%%%%%%%%%%%%%%%%%%
        % Findpeaks positive and negative peaks
        sig_thresh = abs(signal_thresh);
        %%%%%%%%%%%%%%%%%%%%%%%%%%%%%%%%%%%%%%%%%%%%%%%%%%%%%%%%%%%%%%%%%%%%%%%
        minpeakdist = round(60/10/(1/fs));
        %max 10 slams per min = 1 slam every 6 s
        [acceleration,locs] = findpeaks(sig_thresh,'npeaks',...
            tRecord,'minpeakdistance',minpeakdist,...
            'minpeakprominence',Thresh);
        %%%%%%%%%%%%%%%%%%%%%%%%%%%%%%%%%%%%%%%%%%%%%%%%%%%%%%%%%%%%%%%%%%%%%%%
        t_impact = zeros(length(acceleration),1);
        % find time instances of impact
        for n = 1:length(locs)
            for k = 1:length(ysect)
                if (k == locs(1,n))
                    t_impact(n,1)= tsect(1,k);
                    acceleration(1,n)=ysect(1,k);
                 end
            end
        end
        f=figure(idx);
        plot(tsect, ysect, 'k');
        hold on
        plot(tsect,signal_thresh);%plot all outliers
        hold on
        plot(t_impact, acceleration, 'r*');
        hold on
        plot(tsect, Threshold,'LineWidth',2);
        hold on
        plot(tsect, -Threshold,'LineWidth',2);
        hold off
        xlabel('Time (s)');
        ylabel('Acceleration (m/s^2)');
        set(gca,'FontSize',14)
        set(gcf, 'Position', [100,100,900,350]);
        legend('original signal','outliers','slams','upper threshold',...
               'lower threshold');
        ChID = sprintf('Slams - Point %d - File %d',idx,sect);
        plotID = fullfile(plot_folder_directory,ChID);
        saveas(f,plotID,'jpg');
        %%%%%%%%%%%%%%%%%%%%%%%%%%%%%%%%%%%%%%%%%%%%%%%%%%%%%%%%%%%%%%%%%%%%%%%
        if length(acceleration)>=1
        output.t_cat=cat(1,output.t_cat,t_impact);
```

```
60          output.acc_cat=cat(1,output.acc_cat,acceleration');
61          end
62      end
63      disp(['Finished processing channel '  num2str(idx)])
64  end
```

B.1.3. Spectrogram

```
 1  function [output] = Processchan_spect(y,t,idx,tRecord,period,fs,files,DC,↙
plot_folder_directory)
 2  disp(['Started working on channel ' num2str(idx)])
 3  output=struct('t_cat',[],'acc_cat',[],'vel_cat',[],'t',[],'acc',[]);
 4      for sect=1:files %loop for time series
 5          tsect= t((tRecord/period*sect-tRecord/period+1:tRecord/period*sect),1)';
 6          ysect= y((tRecord/period*sect-tRecord/period)+1:(tRecord/period*sect),1)';
 7          f=figure(idx);
 8          ChID = sprintf('spect - Point %d - File %d',idx,sect);
 9          plotID = fullfile(plot_folder_directory,ChID);
10          if ismember(idx,DC)==1
11              pspectrum(ysect,fs,'spectrogram','FrequencyLimits',...
12                  [13 18],'Leakage',0.85,'OverlapPercent',50,...
13                  'TimeResolution',0.5,'MinThreshold',-25)
14          else
15              pspectrum(ysect,fs,'spectrogram','FrequencyLimits',...
16                  [13 18],'Leakage',0.85,'OverlapPercent',50,...
17                  'TimeResolution',0.5,'MinThreshold',-35)
18          end
19          % set: 'TimeResolution','FrequencyLimits','MinThreshold',...
20          % 'OverlapPercent','Leakage'
21          set(gca,'FontSize',14)
22          ylabel('Frequency (Hz)');
23          set(gcf, 'Position', [100,100,900,310]);
24          title(' '); xlabel('Time (min)');
25          saveas(f,plotID,'jpg');
26          F = getframe;
27          %%%%%%%%%%%%%%%%%%%%%%%%%%%%%%%%%%%%%%%%%%%%%%%%%%%%%%%%%%%%%%%%%%%%%%%
28          % Black and white image
29          [I,xData,BW] = BlackWhite(F);
30          %%%%%%%%%%%%%%%%%%%%%%%%%%%%%%%%%%%%%%%%%%%%%%%%%%%%%%%%%%%%%%%%%%%%%%%
31          % Hough transform
32          lines = HoughTransform(BW,tRecord);
33          %%%%%%%%%%%%%%%%%%%%%%%%%%%%%%%%%%%%%%%%%%%%%%%%%%%%%%%%%%%%%%%%%%%%%%%
34          % Scale position of lines, detected as pixels, to correspond to
35          % x-axis of time series plot
36          [t_impact,acceleration]=Image2Time(lines,xData,tsect,ysect,fs);
37          f=figure(idx);
38          ChID = sprintf('slams - Point %d - File %d',idx,sect);
39          plotID = fullfile(plot_folder_directory,ChID);
40          plot(tsect,ysect,'Color',[0.2 0.3 0.5],'LineWidth',1);
41          hold on
42          plot(t_impact,acceleration,'r*');
43          set(gca,'FontSize',14)
44          set(gcf, 'Position', [100,100,900,310]);
45          xlabel('Time (s)')
46          ylabel('Acceleration (m/s^2)');
47          axis tight
48          legend('signal','slam');
49          saveas(f,plotID,'jpg');
50          hold off
51          %%%%%%%%%%%%%%%%%%%%%%%%%%%%%%%%%%%%%%%%%%%%%%%%%%%%%%%%%%%%%%%%%%%%%%%
52          if length(acceleration)>=1
```

```
        output.t_cat=cat(1,output.t_cat,t_impact);
        output.acc_cat=cat(1,output.acc_cat,acceleration);
        end
    end
    disp(['Finished processing channel ' num2str(idx)])
end
```

B.1.4. Continuous Morlet wavelet transform

```
function [output] = Processchan_cwt(y,t,idx,tRecord,fs,files,fb,IMF,plot_folder_directory)
    disp(['Started working on channel ' num2str(idx)])
    output=struct('t_cat',[],'acc_cat',[],'vel_cat',[],'t',[],'acc',[]);
    [TFb1,Lb1,Ub1,Cb1] = isoutlier(IMF(IMF~=0));
    %%%%%%%%%%%%%%%%%%%%%%%%%%%%%%%%%%%%%%%%%%%%%%%%%%%%%%%%%%%%%%%%%%%%%%%
    for sect=1:files %loop for time series
        tsect= t((tRecord/(1/fs)*sect-tRecord/(1/fs)+1:tRecord/(1/fs)*sect),1)';
        ysect= y((tRecord/(1/fs)*sect-tRecord/(1/fs))+1:(tRecord/(1/fs)*sect),1)';
        ysect_imf= IMF((tRecord/(1/fs)*sect-tRecord/(1/fs))+1:(tRecord/(1/fs)*sect),1)';
        %%%%%%%%%%%%%%%%%%%%%%%%%%%%%%%%%%%%%%%%%%%%%%%%%%%%%%%%%%%%%%%%%%%%%%%
        % Ignore signal less than Threshold
        Thresh=max(abs([Ub1 Lb1]));
        Threshold = Thresh*ones(size(tsect));
        % all components larger than Threshold set to one
        % all components less than Threshold set to zero
        signal_thresh = abs(ysect_imf) > Threshold;
        signal_thresh = signal_thresh.*ysect_imf;
        %%%%%%%%%%%%%%%%%%%%%%%%%%%%%%%%%%%%%%%%%%%%%%%%%%%%%%%%%%%%%%%%%%%%%%%
        f=figure(idx);
        ChID = sprintf('cwt - Point %d - File %d',idx,sect);
        plotID = fullfile(plot_folder_directory,ChID);
        cwt(signal_thresh,'FilterBank',fb);
        set(gca,'FontSize',14);
        title('Frequency (Hz)'); xlabel('Time (min)');
        set(gcf, 'Position', [100,100,900,310]);
        saveas(f,plotID,'jpg');
        F = getframe;
        %%%%%%%%%%%%%%%%%%%%%%%%%%%%%%%%%%%%%%%%%%%%%%%%%%%%%%%%%%%%%%%%%%%%%%%
        % Black and white image
        [I,xData,BW] = BlackWhite(F);
        %%%%%%%%%%%%%%%%%%%%%%%%%%%%%%%%%%%%%%%%%%%%%%%%%%%%%%%%%%%%%%%%%%%%%%%
        % Hough transform
        lines = HoughTransform(BW,tRecord);
        %%%%%%%%%%%%%%%%%%%%%%%%%%%%%%%%%%%%%%%%%%%%%%%%%%%%%%%%%%%%%%%%%%%%%%%
        % Scale position of lines, detected as pixels, to correspond to
        % x-axis of time series plot
        [t_impact,acceleration]=Image2Time(lines,xData,tsect,ysect,fs);
        % ignore false peaks detected in zero signal
        for i=1:length(acceleration)
          if   abs(acceleration(i,1))<Threshold
              acceleration(i,1)=inf;
              t_impact(i,1)=inf;
          end
        end
        t_impact(t_impact==inf)=[];
        acceleration(acceleration==inf)=[];
        %%%%%%%%%%%%%%%%%%%%%%%%%%%%%%%%%%%%%%%%%%%%%%%%%%%%%%%%%%%%%%%%%%%%%%%
        f=figure(idx);
        ChID = sprintf('slams - Point %d - File %d',idx,sect);
        plotID = fullfile(plot_folder_directory,ChID);
        plot(tsect,ysect,'Color',[0.5 0.7 1],'LineWidth',1);
```

```
        hold on
        plot(tsect,signal_thresh,'Color',[0.1 0.2 0.4],'LineWidth',1);
        hold on
        plot(t_impact,acceleration,'r*');
        set(gca,'FontSize',14)
        set(gcf,'Position',[100,100,900,310]);
        xlabel('Time (s)')
        ylabel('Acceleration (m/s^2)');
        axis tight
        legend('signal','IMF outliers','slam');
        saveas(f,plotID,'jpg');
        hold off
        %%%%%%%%%%%%%%%%%%%%%%%%%%%%%%%%%%%%%%%%%%%%%%%%%%%%%%%%%%%%%%%%%%%%%%%
        if length(acceleration)>=1
        output.t_cat=cat(1,output.t_cat,t_impact);
        output.acc_cat=cat(1,output.acc_cat,acceleration);
        end
    end
    disp(['Finished processing channel ' num2str(idx)])
end
```

B.1.5. Black and white image

```
function [I,xData,BW] = BlackWhite(F)
% converts image to a black and white image
A = frame2im(F); % capturing the spectogram and converting it to an image
I = rgb2gray(A); % converting it to a grayscale intensity image
RI = imref2d(size(I));% Determine dimensions of image
d = imshow(I,RI);
xData = get(d,'XData'); % number of pixels along x-axis
% Black and white image:
BW = I > 80; %%% set grayscale threshold
end
```

B.1.6. Hough transform

```
function lines= HoughTransform(BW,tRecord)
% detects lines of a binary image
[H,Th,Ro] = hough(BW,'Theta', (-0.01:0.01:0.01));
%%% specify angle Theta to detect vertical line (-0.01:0.01:0.01)

% identify peaks in hough transform
numpeaks = round(tRecord); % maximum number of peaks to identify
P  = houghpeaks(H,numpeaks,'Threshold',...
    ceil(0.2*max(H(:))),'Theta',Th);
%%% Values of H below 'Threshold' will not be considered to be peaks.

lines = houghlines(BW,Th,Ro,P,'FillGap',20,...
    'MinLength',40);

%%%'FillGap': houghlines merges line segments into a single line segment
%%%'MinLength': discard merged line segments shorter than 'MinLength'

%delete repeated lines
[~, index] = unique([lines.rho].', 'rows', 'stable');
lines = lines(index);
end
```

B.1.7. Image pixel coordinate to time signal

```
function [t_impact,acceleration] = Image2Time(lines,xData,tsect,ysect,fs)
% Scale position of lines, detected as pixels, to correspond to
% x-axis of time series plot
tshort=0:1/fs:(length(ysect)-1)/fs';
time_total = tshort(end);
impulse = zeros(length(lines),1);
    for k = 1:length(lines)
    xy = [lines(k).point1; lines(k).point2];
        if (xy(1,1)>2)&&(xy(1,1)<=(xData(1,2)-1))
        % ignore first and last lines which are incorrectly identified
        % start counting pixel coordintes from zero rather than one:
        lines(k).point1=lines(k).point1-[1,1];
        lines(k).point2=lines(k).point2-[1,1];
        % scale position of lines to correspond to x-axis of plot:
        lines(k).point1=lines(k).point1.*[(time_total/(xData(1,2)-1)),0];
        lines(k).point2=lines(k).point2.*[(time_total/(xData(1,2)-1)),0];
        pixel_length=(time_total/(xData(1,2)-1));% determine pixel width
        %xy coordinates
        xy = [lines(k).point1; lines(k).point2];
        %record time of slamming insatnces
        impulse(k,1) = xy(1,1);
        end
    end
time_instance = sort(impulse); % arrange elements in ascending order
time_instance(time_instance==0)=[];%remove zero
acc=zeros(length(time_instance),1);%acceleration amplitude
t_impact=zeros(length(time_instance),1);%time of detected slams
for k=1:length(time_instance)
    % search for maximum peak in pixel range near the line detected
    t1=time_instance(k,1)-pixel_length*4; %starting time to search for peak
    t2=time_instance(k,1)+pixel_length*4; %ending time to search for peak
    for i=1:length(tshort)
        % searching time interval of possible peak:
        if (tshort(1,i)>=t1)&&(tshort(1,i)<=t2)
           if(abs(ysect(1,i))>=abs(acc(k,1)))
               %detecting time of maximum acceleration value
               t_impact(k,1)=tsect(1,i);
               acc(k,1)=ysect(1,i);
           end
        end
    end
end
[t_impact,ia1,ic1]=unique(t_impact);%delete repeated occurences
acceleration= acc(ia1);
end
```

B.1.8. Earliest slam time

```
function [channel_slams,tmin,I,acc_min,t_rank1,acc_rank] = ChannelsSlams(IDX,seconds,output,plot_folder_directory,tol,B_IDX)
peaks=zeros(length(IDX),length(seconds));
for idx=1:length(IDX)
    t1=output(idx).t_cat;
    round_t=round(t1);%round slam time to the nearest second
    peaks(idx,:)=ismember(seconds,round_t);
    %slam indicated as a one to the nearest second for each channel
end
%number of channels that detect slams for each second
accumulated = sum(peaks);
peaks1=peaks;
```

```
accumulated1=accumulated;
for k=length(accumulated)-1:-1:1
    %if multiple channels detect a single slam across several adjacent
    %seconds the slam time is set to the earliest second at which a peak is
    %detected for all of the sensors
    if (accumulated(1,k)~=0)&&((accumulated(1,k+1)~=0))
        sum_total=peaks(:,k)|peaks(:,k+1);
        peaks(:,k)=sum_total;
        peaks(:,k+1)=zeros(size(sum_total));
    end
end
%number of channels that detect slams for each second - aligned
accumulated = sum(peaks);
slams=[];
%The minimum number of sensors that need to detect a peak relating to a
%slamming event for it to be included: tol == 2
peaks2=zeros(size(peaks));
for c=1:length(accumulated)
    if accumulated(1,c)>tol
        peaks2(:,c)=peaks(:,c);
        slams=[slams,c];%index of slams, to the nearest second
    end
end
%number of slams per channel to the nearest second, above tol
channel_slams=sum(peaks2,2);
%%%%%%%%%%%%%%%%%%%%%%%%%%%%%%%%%%%%%%%%%%%%%%%%%%%%%%%%%%%%%%%%%%%%%%%%%%%%%%%
figure %#1
ChID = sprintf('channel slams');
plotID = fullfile(plot_folder_directory,ChID);
bar(channel_slams)
xlabel('Channel');
ylabel('Number of Slams');
set(gcf, 'Position', [900,310,900,310]);
savefig(plotID);
%%%%%%%%%%%%%%%%%%%%%%%%%%%%%%%%%%%%%%%%%%%%%%%%%%%%%%%%%%%%%%%%%%%%%%%%%%%%%%%
%the slam time is set to the earliest second at which a peak is
%detected for all of the sensors, but it accounts for one sensor detecting
%the same slam twice
for k=length(accumulated1)-1:-1:1
    if (accumulated1(1,k)~=0)&&((accumulated1(1,k+1)~=0))
        sum_total=peaks1(:,k)+peaks1(:,k+1);
        peaks1(:,k)=sum_total;
        peaks1(:,k+1)=zeros(size(sum_total));
    end
end
%for the slams which are detected to the nearest second, at the earliest
%time across all channels,
%The detected slams are numbered for each channel
sum_accum=zeros(size(peaks1));
for r=1:length(IDX)
    for c=1:length(peaks1(1,:))
        if peaks1(r,c)==1
            sum_accum(r,c)=sum(peaks1(r,1:c),2);%all slams
        end
        if (peaks1(r,c)~=1)&&(peaks1(r,c)~=0)
            % if a sensor detects the same slam event twice
            % the earliest slam time is used, but the index is incremented
            sum_accum(r,c)=sum(peaks1(r,1:c),2)-peaks1(r,c)+1;%all slams
        end
    end
end
sum_accum=sum_accum.*peaks2;%removes slams below tol
acc_accum=zeros(size(sum_accum));
%The numbered slams for each channel relate to the index of the original
```

```
%slam time vector extracted for each channel
for r=1:length(IDX)
    for i=1:length(slams)
        element=sum_accum(r,slams(1,i));
        if element~=0
           acc_accum(r,slams(1,i))=output(r).acc_cat(sum_accum(r,slams(1,i)));
           sum_accum(r,slams(1,i))=output(r).t_cat(sum_accum(r,slams(1,i)));
        end
    end
end
sum_accum1=sum_accum;
sum_accum1(:,all(sum_accum==0))=[];
acc_accum(:,all(acc_accum==0))=[];
%all zeros set to be larger, so that they are not detected as minimum values
sum_accum1(sum_accum1==0)=seconds(1,end)+1;
%should not detect bridge as site of slam
sum_accum1(B_IDX,:)=ones(2,length(sum_accum1(1,:))).*seconds(1,end)+1;
acc_accum(B_IDX,:)=zeros(2,length(acc_accum(1,:)));
[tmin,I]=min(sum_accum1);
%corresponding acceleration value for earliest slam time
acc_min=zeros(size(tmin));
for c=1:length(I)
    acc_min(1,c)=acc_accum(I(1,c),c);
end
%%%%%%%%%%%%%%%%%%%%%%%%%%%%%%%%%%%%%%%%%%%%%%%%%%%%%%%%%%%%%%%%%%%%%%%%%%%%%%%
figure %#2
ChID = sprintf('Earliest peak');
plotID = fullfile(plot_folder_directory,ChID);
histogram(I,length(IDX))
title("Channels with earliest time for peak detection");
xlabel('Channel');
ylabel('Number of Peaks');
set(gcf, 'Position', [900,310,900,310]);
savefig(plotID);
%%%%%%%%%%%%%%%%%%%%%%%%%%%%%%%%%%%%%%%%%%%%%%%%%%%%%%%%%%%%%%%%%%%%%%%%%%%%%%%
rank=zeros(size(sum_accum));
for r=1:length(sum_accum(1,:))
    [~,~,rnk] = unique(sum_accum(:,r));
    %times in column are ranked from smallest (earliest) to largest
    %(latest)
    rank(:,r)=rnk;
end
t_rank1=rank.*peaks2;% only keep rank of non zero values
% if zero value (slam not detected) in column, rank will start from 2
t_rank1(:,all(t_rank1==0))=[];
%should not detect bridge as site of slam
t_rank1(B_IDX,:)=zeros(2,length(t_rank1(1,:)));
t_rank1((t_rank1==0))=16;
[trank,i]=sort(t_rank1);
acc_rank=zeros(size(trank));
for c=1:length(trank(1,:))
    a=acc_accum(:,c);
    acc_rank(:,c)=a(i(:,c));
end
%%%%%%%%%%%%%%%%%%%%%%%%%%%%%%%%%%%%%%%%%%%%%%%%%%%%%%%%%%%%%%%%%%%%%%%%%%%%%%%
% make smallest values largest by making all values negative:
t_rank=-rank.*peaks2;
%should not detect bridge as site of slam:
t_rank(B_IDX,:)=zeros(2,length(t_rank(1,:)));
%so that the plot appears reasonable
t_rank(t_rank==0)=-length(IDX)-1;
end
```

B.2. Structural vibration analysis

B.2.1. Measurement selection and signal conditioning

```
function [V1,V11,dfs,dfs1] = LoadStructAnalysis(IDX,raw_folder_directory,start_file,end_file,start_time,end_time,V1,V11,Winter)
%Folder selected
raw_file_directory=[raw_folder_directory,'\*.mat'];
filelist = ls(raw_file_directory);
list = filelist(:,1:8);
numfiles = size(filelist,1);
start_file_name = fullfile(raw_folder_directory,filelist(1,:));
start_handle = load(start_file_name);

Strt=0;
Yd_raw=[];
for fileidx = 1:numfiles
    ts = strcmp(list(fileidx,:),start_file);
    if ts == 1
        startsesh = fileidx;
        current_file_name = fullfile(raw_folder_directory,filelist(fileidx,:));
        start_handle = load(current_file_name);
        start_t = start_handle.n_SS_B01_S_X__X.function_record.TL_export_properties_annotation.absolute_time(1:19);
        start_number = datenum(start_t);
        Strt=1;
    end
    %%%%%%%%%%%%%%%%%%%%%%%%%%%%%%%%%%%%%%%%%%%%%%%%%%%%%%%%%%%%%%%%%%%%%%%%%%%%%%%
    if Strt==1
    current_file_name = fullfile(raw_folder_directory,filelist(fileidx,:));
    h = load(current_file_name);
    if Winter==1
        Y_raw=LoadData_15Chan(h);
    else
        Y_raw=LoadData_14Chan_Spring(h);
    end
    %%%%%%%%%%%%%%%%%%%%%%%%%%%%%%%%%%%%%%%%%%%%%%%%%%%%%%%%%%%%%%%%%%%%%%%%%%%%%%%
    Yd_raw=[Yd_raw;Y_raw];
    end
    tf = strcmp(list(fileidx,:),end_file);
    if tf == 1
        endsesh = fileidx;
        break
    end
end
files=endsesh-startsesh+1;
% Signal parameters
fs=1/start_handle.n_SS_D801_P_Y__Y.x_values.increment;
T=1/fs*start_handle.n_SS_D801_P_Y__Y.x_values.number_of_values;%total time
period=1/fs;
end_number = start_number + (T/period*files)/fs/60/60/24;
%%%%%%%%%%%%%%%%%%%%%%%%%%%%%%%%%%%%%%%%%%%%%%%%%%%%%%%%%%%%%%%%%%%%%%%%%%%%%%%
% integrate time sinal
mm=1000;%Convert data to mm/s^2
iir=zeros(23,length(IDX));
velocity = [timeint(mm*Yd_raw(:,IDX),fs,'IIR',1);iir];%-23 samples
%%%%%%%%%%%%%%%%%%%%%%%%%%%%%%%%%%%%%%%%%%%%%%%%%%%%%%%%%%%%%%%%%%%%%%%%%%%%%%%
% HPF
d = designfilt('highpassiir', ...       % Response type
       'StopbandFrequency',0.5, ...     % Frequency constraints
       'PassbandFrequency',1, ...
       'StopbandAttenuation',20, ...    % Magnitude constraints
       'PassbandRipple', 0.1,...
```

```
        'DesignMethod','butter', ...      % Design method
        'MatchExactly','stopband', ...    % Design method options
        'SampleRate',fs);                 % Sample rate
V_fH = filtfilt(d,velocity);
%%%%%%%%%%%%%%%%%%%%%%%%%%%%%%%%%%%%%%%%%%%%%%%%%%%%%%%%%%%%%%%%%%%%%%%%%%%%%%%
% LPF
dfs1=200; % decimated fs i.e. to measure 100 Hz
factor=5; %oversampling factor
v11 = resample(V_fH,25,256);    % Change sampling rate, oversampling = 2
v1=resample(v11,factor,1);      % Resample x up to 10 times oversampling
%%%%%%%%%%%%%%%%%%%%%%%%%%%%%%%%%%%%%%%%%%%%%%%%%%%%%%%%%%%%%%%%%%%%%%%%%%%%%%%
% remove unwanted time
t_abs = start_number:1/dfs1/60/60/24:end_number - 1/dfs1/60/60/24;
v11 = RemoveTime(v11,t_abs,startsesh,endsesh,start_time,end_time,files,T/↙
(1/dfs1))';
t_abs = start_number:1/(dfs1*factor)/60/60/24:end_number - 1/(dfs1*factor)↙
/60/60/24;
v1 = RemoveTime(v1,t_abs,startsesh,endsesh,start_time,end_time,files,T/(1/↙
(dfs1*factor)))';
%remove zeros
v1(:,all(v1==0))=[]; v1=v1';
v11(:,all(v11==0))=[]; v11=v11';
%%%%%%%%%%%%%%%%%%%%%%%%%%%%%%%%%%%%%%%%%%%%%%%%%%%%%%%%%%%%%%%%%%%%%%%%%%%%%%%
V1=[V1;v1];
V11=[V11;v11];
dfs=factor*dfs1;
end
```

B.2.2. Germanischer Loyd velocity limit curves

```
Winter=0; %Winter/Spring cruise
IDX= linspace(1,14,14);%Spring!
%IDX= linspace(1,15,15);%Winter!
%select folder and file:
raw_folder_directory = 'C:↙
\Users\USER\Documents\Cases\SpringStationary\20191118_105248_Run';
start_file='a0111254';
end_file='a0112754';
start_time='18/11/19 11:13:00.000';
end_time='18/11/19 11:28:00.000';
start_time=datenum(start_time,'dd/mm/yy HH:MM:SS.FFF');
end_time=datenum(end_time,'dd/mm/yy HH:MM:SS.FFF');
V11=[]; %Integrated, HPF and LPF velocity signal
V1=[]; %10 times oversampled signal
[V1,V11,dfs,dfs1] = LoadStructAnalysis(IDX,raw_folder_directory,start_file,...
                    end_file,start_time,end_time,V1,V11,Winter);
tv11=makexaxis(V11,1/(dfs1));% time vector for velocity signal
%% fft exceedance of 30 mm/s curve
tspan=60;%seconds
offset=5;%seconds
num_int=round(((tv11(end,1))-tspan)/offset+1);
%limit curves
k2=12; k1=6; m=1;
f1=1:5; f2=5:100;
yl2=@(x2)k2*x2.^m; yl1=@(x1)k1*x1.^m;
%initialise vectors
excd5_100Hz=zeros(num_int,length(IDX));
excd1_5Hz=zeros(num_int,length(IDX));
MAX=zeros(num_int,length(IDX));
F_max=zeros(num_int,length(IDX));
T_max=zeros(num_int,length(IDX));
```

```
excd_true=0;
for idx=1:length(IDX)
    for sect=1:num_int
        sig=V11((sect-1)*offset*dfs1+1:((sect-1)*offset+tspan)*dfs1,idx);
        win=2048; % hanning window length
        % alinspec ABRAVIBE function changed to obtain peak velocity values
        % rather than RMS velocity values for FFTp function:
        [Lyy,f] = FFTp(sig,dfs1,ahann(win),ceil(tspan*dfs1/win)*2-2,50);
        fres=f(2)-f(1);%frequency resolution
        Thresh=6:k1*fres:30;%threshold: delta y related to delta x
        idxl = f>=1;
        idxl(1) = 0;
        i1 = find(idxl);% frequency index 1
        idxl = f<=5;
        idxl(1) = 0;
        i2 = find(idxl);% frequency index 2
        %lower limit curve exceedance, between 1 to 5 Hz
        excd1_5Hz(sect,idx)=any(Lyy(i1(1):i2(end))>Thresh(:));
        %lower limit curve exceedance, between 5 to 100 Hz
        excd5_100Hz(sect,idx)=any(Lyy>30);
        [MAX(sect,idx),I]=max(Lyy);% Maximum FFT point
        F_max(sect,idx)=f(I);% Frequency of max FFT point
        T_max(sect,idx)=k1*f(I).^m;% Threshold corresponding to frequency
        if (excd1_5Hz(sect,idx)==1)||(excd5_100Hz(sect,idx)==1)
           loglog(f,Lyy,'Color',[0.8 0.8 0.9],'LineWidth',1); hold on
           excd_true=excd_true+1;% count and plot curve exceedance
        end
    end
end
%maximum curve exceedance:
[U1,I1]=max(MAX,[],2); [U2,I2]=max(U1); %index of maximum exceedance
idx=I1(I2);sect=I2;
sig=V11((sect-1)*offset*dfs1+1:((sect-1)*offset+tspan)*dfs1,idx);
[Lyy,f] = FFTp(sig,dfs1,ahann(win),ceil(tspan*dfs1/win)*2-2,50);
loglog(f,Lyy,'Color',[0.2 0.2 0.7],'LineWidth',1); hold on
V1=60.*ones(size(f2)); V2=30.*ones(size(f2));
plot(f2,V1,'k'); hold on; plot(f2,V2,'k'); hold on
loglog(f1,yl1(f1),'k'); hold on; loglog(f1,yl2(f1),'k'); hold on
xlabel('Frequency (Hz)'); ylabel('Velocity (mm/s)');
xlim([1 100]); ylim([min(Lyy) 90]);
set(gca,'FontSize',14)
set(gcf, 'Position', [100,100,500,300]);
legend('FFTs exceeding curves','FFT with largest exceedance',...
        'GL Limit curves');
```

B.3. Operational modal analysis

B.3.1. Frequency domain decomposition

```
Winter=0; %Winter/Spring cruise
IDX= linspace(1,13,13);%Spring!
%IDX= linspace(1,15,15);%Winter!
%select folder and file:
raw_folder_directory = 'C:\Users\USER\Documents\Cases\SpringStationary\20191118_105248_Run';
start_file='a0111254';
end_file='a0112754';
start_time='18/11/19 11:13:00.000';
end_time='18/11/19 11:28:00.000';
start_time=datenum(start_time,'dd/mm/yy HH:MM:SS.FFF');
end_time=datenum(end_time,'dd/mm/yy HH:MM:SS.FFF');
[y0,dfs] = LoadDataOMA(IDX,raw_folder_directory,start_file,end_file,...
            start_time,end_time,Winter); % repeat for each relative heading
ty1=makexaxis(y0,1/(dfs));
%%
%frequency domain decomposition (FDD)
N=2048;
C=[0.2 0.2 0.7;0.6 0.2 0.7;0.8 0.4 0.5;0.2 0.6 0.4;0.2 0.8 0.7];
P=zeros(length(IDX),length(IDX));
for i=1:5 %each relative heading: y0 to y180
    switch i
        case 1
        [Pyx,f,Nblocks] = acsdw(y0,y0,dfs,ahann(N),50);
        case 2
        [Pyx,f,Nblocks] = acsdw(y45,y45,dfs,ahann(N),50);
        case 3
        [Pyx,f,Nblocks] = acsdw(y90,y90,dfs,ahann(N),50);
        case 4
        [Pyx,f,Nblocks] = acsdw(y135,y135,dfs,ahann(N),50);
        otherwise
        [Pyx,f,Nblocks] = acsdw(y180,y180,dfs,ahann(N),50);
    end
    for I=1:length(Pyx(:,1,1))
        P(:,:)=Pyx(I,:,:);
        [u,s,~] = svd(P);
        s1(I) = s(1);% First eigen values
        ms(:,I)=u(:,1);% Mode shape
    end
    switch i % Plot first singular values of the PSD matrix
        case 1
        loglog(f,(s1),':','Color',C(i,1:3),'LineWidth',1);hold on
        case 2
        plot(f,(s1),'-.','Color',C(i,1:3),'LineWidth',1);hold on
        case 3
        plot(f,(s1),'--','Color',C(i,1:3),'LineWidth',1);hold on
        case 4
        plot(f,(s1),'.-','Color',C(i,1:3),'LineWidth',1);hold on
        otherwise
        plot(f,(s1),'Color',C(i,1:3),'LineWidth',1);hold on
    end
end
legend('0°','45°','90°','135°','180°');
xlabel('Frequency (Hz)')
ylabel('Singular values of CPSD','mm/s^2)^2/Hz');
xlim([0 9]); ylim([0 10^8])
yticks([10 10^5])
set(gca,'FontSize',14) ;  set(gcf, 'Position', [100,100,600,300]);
%%
```

```
close all
% Identified modal frequencies
Irgb=zeros(1,5); I1=zeros(1,5); I2=zeros(1,5); %frequency index
MRgb=zeros(length(IDX),5);
ms1=zeros(length(IDX),5); ms2=zeros(length(IDX),5);
N=2048;%window length
fUB=zeros(5,3);fLB=zeros(5,3);
for angle=1:5 % for each realative heading
    switch angle
        case 1
        [Pyx,f,Nblocks] = acsdw(y0,y0,dfs,ahann(N),50);
        case 2
        [Pyx,f,Nblocks] = acsdw(y45,y45,dfs,ahann(N),50);
        case 3
        [Pyx,f,Nblocks] = acsdw(y90,y90,dfs,ahann(N),50);
        case 4
        [Pyx,f,Nblocks] = acsdw(y135,y135,dfs,ahann(N),50);
        otherwise
        [Pyx,f,Nblocks] = acsdw(y180,y180,dfs,ahann(N),50);
    end
    [Irgb(angle),I1(angle),I2(angle),M1,M2,fub,flb] = ModeParam(IDX,Pyx,f);
    ms1(:,angle)=M1; ms2(:,angle)=M2; % mode shapes
    fUB(angle,:)=fub; fLB(angle,:)=flb; % upper and lower frequency bounds
end
%% MAC
C3ms1=ms1;C3ms2=ms2;% case 3 mode shapes for MAC matrix
%% PSD
idx=[1 2 12 13];% bow and stern accelerometer channels
E=zeros(5,3);
for angle=1:5
    switch angle
        case 1
        [Pxx,fxx] = apsdw(y0,dfs,N);% default ahann() & 50% overlap
        case 2
        [Pxx,fxx] = apsdw(y45,dfs,N);
        case 3
        [Pxx,fxx] = apsdw(y90,dfs,N);
        case 4
        [Pxx,fxx] = apsdw(y135,dfs,N);
        otherwise
        [Pxx,fxx] = apsdw(y180,dfs,N);
    end
    ER=zeros(length(idx),3);
    for i=1:length(idx)% for each channel
        % upper and lower frequency bounds: PSD curve section for each mode
        PR=Pxx(fLB(angle,1):fUB(angle,1),idx(i));% RBM
        P1=Pxx(fLB(angle,2):fUB(angle,2),idx(i));% VBM 1
        P2=Pxx(fLB(angle,3):fUB(angle,3),idx(i));% VBM 2
        x=fxx(2)-fxx(1);%frequency resolution
        ER(i,1)=sqrt(trapz(x,PR));%RMS RBM
        ER(i,2)=sqrt(trapz(x,P1));%RMS VBM 1
        ER(i,3)=sqrt(trapz(x,P2));%RMS VBM 2
    end
%average RMS for bow and stern sensors
E(angle,:)= [sum(ER(:,1))/length(idx) sum(ER(:,2))/length(idx) sum(ER(:,3))↙
/length(idx)];
end
%% bar graphs
angle=[0 45 90 135 180];
ba=bar(angle,([E(:,2)'; E(:,3)']),'stacked','FaceColor','flat'); hold on
ba(1).CData = [0.5 0.6 0.8];
ba(2).CData = [0.3 0.8 0.5];
xlabel('Angle (°)');
```

```
ylabel({'Acceleration PSD';'(mm/s^2)^2/Hz RMS'});
legend('VBM 1','VBM 2')
set(gca,'FontSize',14) ;  set(gcf, 'Position', [100,100,800,200]);
ylim([0 800])
xlim([-45/2 180+45/2])
```

B.3.2. Modal parameters

```
function [Irgb,I1,I2,M1,M2,fub,flb] = ModeParam(IDX,Pyx,f)
    P=zeros(length(IDX),length(IDX));
    ms=zeros(length(IDX),length(Pyx(:,1,1)));
    % Compute SVD of the PSD at each frequency
    for I=1:length(Pyx(:,1,1))
        P(:,:)=Pyx(I,:,:);
        [u,s,~] = svd(P);
        s1(I) = s(1);% First eigen values
        ms(:,I)=u(:,1);% Mode shape
    end
    I=find(f==1); %1 Hz, frequency range
    [MAX,Irgb]=max(s1(1:I));% Rigid Body Motion < 1Hz
    UB=find(f==3); %3 Hz, frequency range < VBM 2
    l=s1(I:UB); % frequency range 1 to 3 Hz
    [MAX,I1]=max(l);% VBM 1
    I1=I1+I-1;% frequency index
    M1=(ms(:,I1));% mode shape 1
    I=find(f==3); %3 Hz
    I2=find(f==10); %10 Hz
    clear l; l=s1(I:I2); % frequency range 3 to 10 Hz
    [MAX,I2]=max(l); % VBM 2
    I2=I2+I-1;% frequency index
    M2=(ms(:,I2));% mode shape 2
    MRgb=(ms(:,Irgb));% Rigid Body Motion
    for mode=1:3
        MAC1=[1 1; 1 1]; c1=0;
        MAC2=[1 1; 1 1]; c2=0;
        lim=90;
        for i=1:length(s1)
            if (MAC1(1,2) > lim/100)
                c1=c1+1;
                switch mode
                    case 1
                        MAC1 = amac([MRgb (ms(:,Irgb+c1))]);
                    case 2
                        MAC1 = amac([M1 (ms(:,I1+c1))]);
                    otherwise
                        MAC1 = amac([M2 (ms(:,I2+c1))]);
                end
            end
            if (MAC2(1,2) > lim/100)&&((Irgb+c2-1)>0)
                c2=c2-1;
                switch mode
                    case 1
                        MAC2 = amac([MRgb (ms(:,Irgb+c2))]);
                    case 2
                        MAC2 = amac([M1 (ms(:,I1+c2))]);
                    otherwise
                        MAC2 = amac([M2 (ms(:,I2+c2))]);
                end
            end
        end
        fub(mode)=Irgb+c1-1;
```

```
54          flb(mode)=Irgb+c2+1;
55      end
56  end
```